

Systematic study of photoneutron reactions just above the neutron emission threshold

Vom Fachbereich Physik
der Technischen Universität Darmstadt
zur Erlangung des Grades
eines Doktors der Naturwissenschaften (Dr. rer. nat.)
genehmigte

Dissertation

von
Dipl. Phys. Jens Hasper
aus Bad Hersfeld

Januar 2008

Darmstadt
D 17

Dissertation eingereicht am 30. Januar 2008
Mündliche Prüfung am 14. April 2008

Prüfer

Professor Dr. rer. nat. Norbert Pietralla

(Referent)

Professor Dr. rer. nat. Andreas Zilges

(Korreferent)

Professor Dr. rer. nat. Karlheinz Langanke

Professor Dr. rer. nat. Thomas Walther

It is a capital mistake to theorize before one has data.
Insensibly one begins to twist facts to suit theories,
instead of theories to suit facts.

Arthur Conan Doyle (1859 - 1930)
A Scandal in Bohemia

Abstract

This thesis deals with the systematic study of photoneutron reactions in the astrophysically relevant energy region just above the neutron threshold.

Photodisintegration reactions play a decisive role in the nucleosynthesis of elements heavier than iron. A large number of proton-rich isotopes are believed to be exclusively produced by a combination of (γ, n) , (γ, p) and (γ, α) reactions during supernova explosions in the so-called p process. Astrophysical network calculations of this process have to account for thousands of photodisintegration reaction rates which mainly need to be adopted from theoretical predictions. To test and improve the predictive power of these calculations, it is mandatory to provide reliable experimental data for those reactions which can be studied in the laboratory.

Therefore, in the scope of this thesis, the photoneutron reactions of various isotopes have been measured in photoactivation experiments at the superconducting Darmstadt electron linear accelerator S-DALINAC. In particular, for the first time, experimental data have been provided for the photoneutron cross sections of rare-earth isotopes in the astrophysically relevant energy region. The experimental results will be compared with theoretical predictions of two statistical model codes and discussed with regard to their astrophysical implications.

Zusammenfassung

Diese Arbeit beschäftigt sich mit der systematischen Untersuchung von (γ, n) -Reaktionen im astrophysikalisch relevanten Energiebereich knapp oberhalb der Neutronenseparationsenergie.

Photodisintegrationsreaktionen spielen eine maßgebliche Rolle in der Nukleosynthese der Elemente schwerer als Eisen. Man geht davon aus, dass eine große Anzahl von protonenreichen Kernen ausschließlich durch eine Kombination von (γ, n) -, (γ, p) - und (γ, α) -Reaktionen während einer Supernova-Explosion im sogenannten p -Prozess gebildet werden kann. Astrophysikalische Netzwerkrechnungen für diesen Prozess müssen tausende von Photodisintegrationsraten berücksichtigen, die weitestgehend auf theoretischen Vorhersagen beruhen. Um die Vorhersagekraft dieser Rechnungen zu überprüfen und zu verbessern, ist es erforderlich zuverlässige experimentelle Daten für all diejenigen Reaktionen zu liefern, die im Labor zugänglich sind.

Zu diesem Zweck wurden im Rahmen dieser Arbeit verschiedene (γ, n) -Reaktionen in Photoaktivierungsexperimenten am supraleitenden Elektronenbeschleuniger S-DALINAC vermessen. Insbesondere wurden erstmalig experimentelle Daten für (γ, n) -Wirkungsquerschnitte im astrophysikalisch relevanten Energiebereich in der Massenregion der Seltenen Erden bereitgestellt. Die experimentellen Ergebnisse werden mit zwei auf dem Statistischen Modell basierenden Rechnungen verglichen und im Hinblick auf ihre astrophysikalische Relevanz diskutiert.

Contents

1	Introduction	1
2	Physics basics	5
2.1	Nucleosynthesis of elements	5
2.1.1	The solar abundance distribution	5
2.1.2	Stellar nucleosynthesis	6
2.1.3	The s , r , and p process	7
2.1.4	Photodisintegration in the nucleosynthesis of heavy elements	11
2.2	Astrophysical implication of ground-state reaction rates	13
2.3	Theoretical basics of reaction-rate calculations	19
2.3.1	The statistical model	19
2.3.2	Nuclear physics input	22
3	Photoactivation experiments at the S-DALINAC	25
3.1	Experimental technique	25
3.1.1	Normalization of absolute cross-section predictions	29
3.1.2	Determination of ground-state reaction rates	29
3.2	Determination of reaction yields	32
3.2.1	Detector setups	34
3.2.2	Detection efficiency	35
3.2.3	Correction for self-absorption and target dimensions	38
3.2.4	Treatment of summing effects	39
3.3	Determination of the photon flux	43
3.3.1	Spectral shape of bremsstrahlung	43
3.3.2	Absolute normalization of the photon flux	44
3.4	Determination of the beam energy	50

3.4.1	Offline method using a deflecting magnet	51
3.4.2	Direct measurement of bremsstrahlung spectra	52
3.4.3	Photoactivation very close to the neutron threshold	54
3.4.4	Charge distribution in a segmented radiator	56
3.4.5	Comparison and summary of various techniques	57
3.5	Systematic and statistical uncertainties	58
4	Experimental results	61
4.1	Photoneutron reactions of rare-earth isotopes	61
4.1.1	Experiment and data analysis	61
4.1.2	Results	64
4.2	Photoneutron reactions near the neutron-shell closure	69
4.2.1	Experiment and data analysis	69
4.2.2	Results	70
4.3	The photoneutron reaction of ^{192}Os	72
4.3.1	Experiment and data analysis	75
4.3.2	Results	77
4.4	The photoneutron reactions of $^{191,193}\text{Ir}$	79
4.4.1	Experiment and data analysis	79
4.4.2	Results	82
4.5	Overview	85
5	Discussion	89
5.1	Sensitivity of statistical model calculations to nuclear physics input	89
5.2	Global predictive power of statistical model codes	95
6	Summary and outlook	99
A	Parametrization of bremsstrahlung spectra	109
B	Input for detection-efficiency calibrations	111
B.1	Calibration sources	111
B.2	Detector dimensions	112

C	Correction factors for the determination of target activity	113
C.1	Corrections for self-absorption and target dimensions	113
C.2	Correction factors for summing effects	113

Chapter 1

Introduction

Since the early civilizations of our ancient world, mankind was trying to understand the composition of matter. Driven by the idea that the complexity of matter can be reduced to a combination of only a small number of basic components, Empedokles (about 490 – 420 B.C.) postulated that the enormous variety of properties observed for all different kinds of materials can be explained by the interaction of only four basic elements: fire, water, earth, and air. This theory dominated the world view of the western culture for almost two thousand years.

It was not until the second half of the 18th century that atomism, i. e., the theory that all objects are composed of a certain number of indivisible and indestructible blocks, so-called *atoms*, started to gain in importance, encouraged by the observations of chemical experiments. During that time, the ambitious studies of many scientists revealed the existence of a large number of chemical elements, which were classified on a systematic basis. The most promising approach was given by the periodic system of elements by Mendelejeff in the year 1869 listing 63 different elements [1]. This periodic system still serves as the basis for today's classification. From then on, many physical experiments aimed to study the properties of atoms themselves indicating that atoms consist of even smaller components.

In the year 1897, Thomson discovered the existence of small negatively-charged particles in atoms: *electrons*. Afterwards, the famous scattering experiment of α particles on thin gold foils by Rutherford in the year 1910 gave strong evidence that atoms consist of a small positively-charged nucleus covered by a cloud of electrons. Some years later, it was found that the nucleus is made of a certain number of positively-charged and neutral particles: *protons* and *neutrons*. Finally, today, one knows that protons and neutrons are also composed in a complex way of even smaller particles, so-called *quarks*. The investigation of the properties and interactions of these elementary particles is still an ambitious aim of modern research.

Parallel to these studies, scientists started to go further into the question of the origin of chemical elements. In particular, since first data for the relative abundances of elements were provided by the geochemist Goldschmidt in 1937 [2], theoretical models for the synthesis of elements in our universe could be reviewed on the basis of observed data. Within the following years, the accuracy of the observed abundance pattern was increased significantly by several works due to spectroscopic data of the sun and mass-spectroscopic data of meteoroids. This revealed more and more features of the abundance curve.

In the late 1930s and early 1940s, many theories were developed to quantitatively describe the details of the abundance distribution, most of them assuming that the large bulk of elements was produced in a primordial state of our universe (e. g., see Ref. [3]). However, many observations made in these years indicated that these theories were not able to provide a comprehensive explanation for all the features of the abundance pattern. Moreover, the detection of lines of technetium in the spectra of evolved red giant stars in 1952 by the astronomer Merrill brought forward a powerful argument against theories postulating an exclusive primordial nucleosynthesis. Because the longest-living isotope of technetium has a half-life of only about four million years, this observation was a strong evidence for ongoing nucleosynthesis in our universe.

Based on large amounts of empirical data, Burbidge, Burbidge, Fowler, and Hoyle (B²FH) published their pioneering work on the synthesis of elements in stars in the year 1957 [4]. In this work, the idea was presented that all elements heavier than hydrogen can be built during the various evolutionary stages of stars. In this context, they postulated eight different nucleosynthetic processes giving a complete explanation for all details of the abundance curve. Aware that the amount of empirical data available at that time was not sufficient to prove their theory beyond all reasonable doubt, the main intention of the authors was to “*lay the groundwork for future experimental, observational, and theoretical work which may ultimately provide conclusive evidence for the origin of the elements in stars*”.

Indeed, this work has often been regarded as the starting point for a new field of research called *Nuclear Astrophysics*, which has rapidly aroused great interest among many scientists. In the following decades, extensive experimental and theoretical studies have been carried out to confirm and to extend the suggestions by B²FH pushed on by further improving empirical data from observations of stars. In the year 1997, the results of forty years of research on the synthesis of elements in stars have been brought together in the comprehensive review by Wallerstein *et al.* [5]. Although some of the processes proposed by B²FH had to be either revised or extended, it is remarkable that many of their ideas could be verified.

However, even nowadays, more than fifty years later, the search for the origin of chemical elements has not lost its fascination, and Nuclear Astrophysics has become one of the most attractive fields of Nuclear Physics containing many open questions. The interdisciplinary work of astronomers, chemists, geologists, astrophysicists, and nuclear physicists reveals more and more features of the evolution of our universe, which need to be explained.

One of the still heavily discussed questions deals with the nucleosynthesis of elements heavier than iron. This subfield of Nuclear Astrophysics provided the motivation for this thesis. In the first part of Chapter 2, an overview of the stellar synthesis of heavy elements will be given. In particular, the astrophysical implication of photodisintegration reactions will be outlined. Astrophysical studies nowadays take into account huge reaction networks involving an enormous number of nuclear reaction rates. These rates mainly need to be adopted from theoretical calculations. Therefore, the second part of Chapter 2 describes the basic ideas of theoretical models based on the theory of Hauser and Feshbach [6]. The aim of this thesis is to provide reliable

experimental data for photoneutron reactions with astrophysical implication. Thus, in Chapter 3 the experimental setup and the data analysis will be described in detail. Experimental results of the photoneutron reactions of ten different isotopes will be presented and compared to the theoretical calculations in Chapter 4. The results will then be discussed in Chapter 5. Finally, a summary and outlook will be given in Chapter 6.

Chapter 2

Physics basics

This chapter is intended to introduce the main theories regarding the nucleosynthetic processes in stars and, thereby, outlines the nucleosynthesis of heavy elements beyond iron and the role of photodisintegration reactions. In this context, the astrophysical implication of experimentally determined reaction rates will be discussed. The second part of this chapter will discuss the main ideas of statistical model calculations. This will serve as the basis for a deeper discussion on the reliability of theoretical calculations in a later chapter of this work, where predictions of two advanced statistical model codes will be compared to experimental data of several photoneutron reactions.

2.1 Nucleosynthesis of elements

2.1.1 The solar abundance distribution

From the large amount of observational data stemming from mass spectroscopy of meteoroids and the spectral lines of stars, the solar abundance distribution nowadays has been accurately determined. A compilation of these data was published in a work by Anders and Grevesse in the year 1989 [7] and still serves as the standard test for many quantitative nucleosynthesis network calculations. Some of these data have recently been revised in Ref. [8]. The abundance curve derived from this compilation is shown in Fig. 2.1, and today's uncertainties for the elemental abundances are summarized in Fig. 2.2 showing a mean uncertainty of only about 7%. Data for isotopic solar abundance ratios are even more accurate because these ratios are not affected by the galactical chemical evolution of matter. Thus, the observed abundance pattern sets strong constraints on nucleosynthesis models. As shown in Fig. 2.1, the solar abundance distribution cannot be simply described by a smooth curve but exhibits many features which need to be accounted for in any complete theory on nucleosynthesis. These features will be discussed in the following sections.

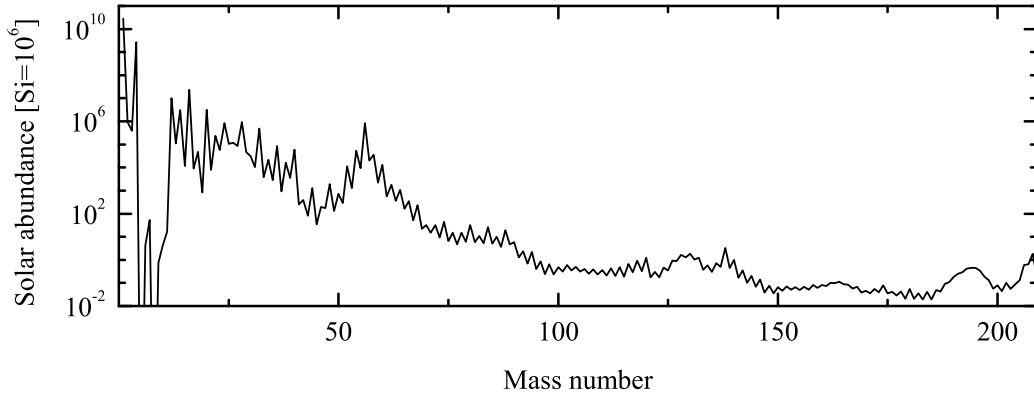


Fig. 2.1: Solar abundance distribution derived from the compilation of Ref. [7]. See text for details.

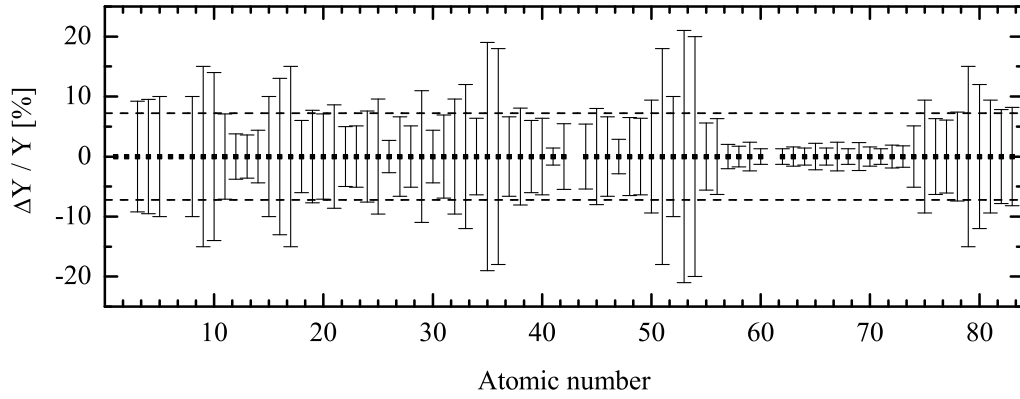


Fig. 2.2: Uncertainties of elemental abundances Y quoted in Ref. [7]. The mean uncertainty is indicated by dashed lines.

2.1.2 Stellar nucleosynthesis

As clearly seen from the solar abundance distribution in Fig. 2.1, the matter of our universe is strongly dominated by hydrogen and helium. Most of their abundances are known to be built in the explosive primordial synthesis of the big bang. However, many observations in the last decades have proven that the production of all elements heavier than hydrogen is still an ongoing process taking place in the various burning phases of stars.

The evolution of a star starts with quiet *hydrogen burning*. In this evolutionary stage, energy is produced by the fusion of hydrogen to helium under conditions of a hydrostatic equilibrium. This burning phase usually lasts for millions or even billions of years depending on the mass of the star. However, at some point in time, hydrogen is exhausted and energy production is not

sufficient anymore to balance the gravitational pressure of the massive envelope of the star. The gravitational work then heats up the core and ignites *helium burning* leading to the production of ^{12}C by the fusion of three α particles. This burning continues until helium is exhausted and the way is cleared for burning phases of higher temperatures such as *carbon burning* and *oxygen burning*, where even heavier nuclei are synthesized. With each evolutionary stage of stars temperature increases until, finally, a nuclear statistical equilibrium is reached in the so-called *silicon burning*, in which only the most tightly bound isotopes survive. Under these conditions, the abundance peak in the iron region at mass number $A = 56$ is produced.

Further fusion of charged nuclei beyond this iron peak is strongly suppressed due to the decreasing binding energy per nucleon and the increasing coulomb barrier. Thus, a different nucleosynthetic mechanism is required to account for those heavy elements. Double peaks in the abundance pattern at certain mass numbers ($A = 80$ and 90 , $A = 130$ and 138 , and $A = 195$ and 208) gave rise to the idea of the synthesis of heavy nuclei by two neutron capture processes, the so-called *slow neutron-capture process* (s process) and the *rapid neutron-capture process* (r process). In the last decades, much more evidence has been found for the existence of these processes. More details will be given in the following section. However, even this variety of processes can still not account for a large number of stable proton-rich nuclei, i. e., isotopes having more protons relative to other stable nuclei in an isotopic chain. For this reason, B²FH had demanded the existence of another process, the so-called p process. Recent results have shown that this process is mainly dominated by photodisintegration reactions under the explosive conditions of supernovae. This will also be discussed in detail in the next section.

Although the key features of the solar abundance distribution can be understood within the denoted processes, many questions in the quantitative description of the abundance curve still remain unanswered providing much opportunity for extensive studies in the field of Nuclear Astrophysics in the future. To mention a few examples, the origin of the very rare elements D, Li, Be and B still is not fully understood. Moreover, even results of latest nucleosynthesis network calculations show large discrepancies with empirical data for certain heavy isotopes, e. g., several isotopes just below the $A \approx 100$ mass region are systematically underproduced by theoretical calculations. In this context, recent theoretical models have revealed the importance of neutrinos for the synthesis of many elements calling for additional processes such as the ν process and νp process. It would go far beyond the scope of this thesis to cover this new field of nuclear astrophysics with neutrinos sufficiently, and the reader, therefore, is referred to Refs. [9, 10].

2.1.3 The s , r , and p process

Almost all nuclei heavier than iron are synthesized by the slow neutron-capture process (s process) and the rapid neutron-capture process (r process). A small fraction of isotopes, however, cannot be produced in either of these two processes and is believed to be synthesized to a large

degree by photodisintegration reactions in a hot stellar environment. In the following, these processes will be described in more detail in the context of nucleosynthesis of rare-earth isotopes in the mass region $A \approx 150$. The experiments presented in Chapter 4 focus on this mass region. The rare-earth isotopes are exceptionally well suited to test stellar nucleosynthesis models with high accuracy because their relative abundances are known to an uncertainty of better than two percent (see Fig. 2.2). The main contributions to nucleosynthesis in this mass region are illustrated in the partial chart of nuclei shown in Fig. 2.3.

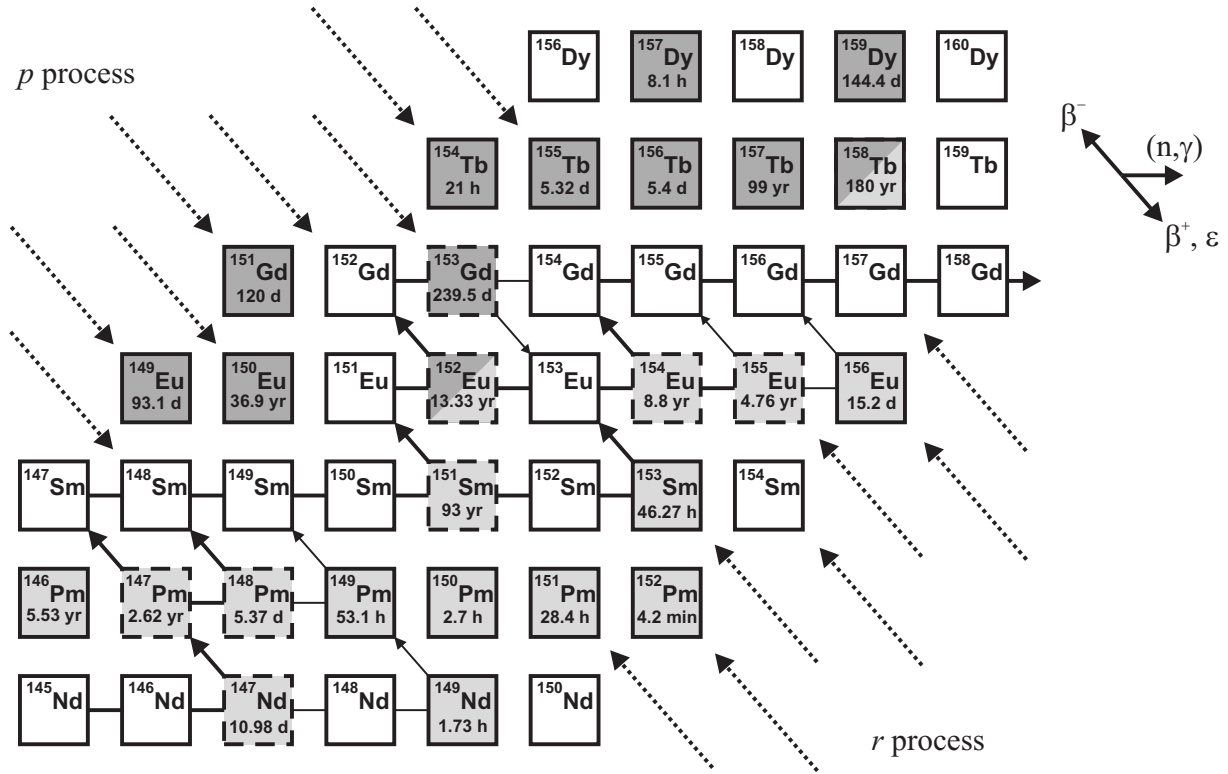


Fig. 2.3: Nucleosynthesis in the rare-earth region. The s -process flow is illustrated by solid lines. The thickness of the lines indicates the strength of the reaction flow. The reaction path is influenced by several branching points (dashed boxes). Unstable isotopes are shaded light gray (β^-) and dark gray (β^+ , ϵ). Most isotopes also have nucleosynthesis contributions from the r and p processes (dotted lines), respectively.

The s process

In the s process, neutrons are sequentially captured by stable isotopes at moderate neutron densities and temperatures (mean values: $n_n \approx 10^8 \text{ cm}^{-3}$, $T \approx 1 - 3 \times 10^8 \text{ K}$). When an unstable isotope is reached along the process path, the β -decay rate will usually exceed the neutron-capture rate, and the unstable isotope decays before another neutron can be captured. Thus, the reaction path follows the valley of stability involving mainly stable isotopes as illustrated in

Fig. 2.3. Those isotopes having a closed neutron shell and, thus, a significantly reduced neutron-capture cross section, act as a bottleneck in the process path leading to an increased abundance of isotopes with neutron-magic numbers. Hence, peaks in the solar abundance distribution at the mass numbers $A = 90$, 138, and 208 corresponding to neutron numbers $N = 50$, 82, and 126 can be observed as shown in Fig. 2.1.

In the last decades, extensive experimental studies have been carried out in neutron-capture experiments. Neutron-capture cross sections for a wide range of isotopes have become available with uncertainties of only a few percent [11, 12]. With this enormous amount of nuclear physics input, the understanding of s -process nucleosynthesis has been largely improved.

Two different sites are involved in the s -process nucleosynthesis. Isotopes of mass between $A = 56$ and $A = 90$ are synthesized in the *weak* s process during He- and C-shell burning in massive stars. On the other hand, the heavy isotopes up to mass number $A = 208$ are produced in the *main* s process during He-shell burning of thermal-pulsing AGB stars. Great improvements in the stellar models describing these sites have been achieved in the last years (e. g., see Ref. [13]) showing that the observed abundances of many isotopes can only be reproduced accurately by network calculations if the full dynamics of the physical conditions in the stellar environment are taken into account.

A very sensitive test for stellar models is provided by the so-called *branching points* along the s -process path. These unstable isotopes exhibit a half-life long enough for the neutron capture to become competitive with β decay. This situation leads to branchings of the reaction flow where the branching ratios sensitively depend on the physical conditions of the stellar site. Important branchings in the rare-earth region occur at the isotopes ^{147}Nd , $^{147,148}\text{Pm}$, ^{151}Sm , $^{154,155}\text{Eu}$, and ^{153}Gd as illustrated in Fig. 2.3. Unfortunately, experimental investigations of the neutron-capture cross sections of branching points are difficult to perform due to the instability of these nuclei. Although some ambitious experiments have provided direct experimental data for the rather long-lived isotopes [14–17], the neutron-capture cross sections of branching points usually have to be adopted from theoretical predictions. The rather large uncertainties of these calculations hamper further improvements of nucleosynthesis models for the s process [18].

Nevertheless, experimental data for the neutron-capture cross sections of branching points can be derived from studying the inverse reaction, i. e., the (γ, n) reaction of a stable neighbouring nucleus. The aim of these measurements is to constrain and improve the nuclear physics input adopted for the theoretical predictions of the stellar neutron-capture rates. This approach has been presented, e. g., in Ref. [19] and will be further discussed in Chapter 5. A detailed description of the s process is given in the comprehensive article of Ref. [20].

The r process

As discussed in the preceding paragraph, a large number of isotopes can be synthesized by slow neutron captures in the s process up to the isotope ^{209}Bi . Beyond this isotope, the instability of

nuclei against α decay terminates the s -process reaction flow. Obviously, the s process is not able to produce all heavy isotopes observed in the solar abundance distribution. For example, there is no way of reaching the heaviest stable elements, uranium and thorium, by slow neutron capture. Furthermore, many stable neutron-rich isotopes are shielded against the s process by short-lived β -unstable nuclei, e. g., the isotopes ^{150}Nd and ^{154}Sm as shown in Fig. 2.3.

Therefore, another neutron-capture process, the r process, has been postulated. Those nuclei which can only be produced within this process are called r -only isotopes accordingly. This process dictates that neutrons are captured on a very short time scale compared to the half-lives of β -unstable nuclei allowing the process to synthesize very neutron-rich isotopes. Thus, the process needs to take place under conditions of very high neutron densities ($n_n \gg 10^{20} \text{ cm}^{-3}$). Such conditions can only be found in explosive stellar scenarios. Although the astrophysical scenario of the r process is still under discussion, one of the most promising sites are Type II supernovae.

Under these explosive conditions, neutron capture and neutron emission by photodisintegration become comparable, and the so-called (n, γ) - (γ, n) equilibrium is established within each isotopic chain. β decays connect the different elements but are slow compared to the other reactions. Only one or two nuclei are significantly produced per isotopic chain, and their decay determines the flow to the next chain. These nuclei are called *waiting points*, and their abundances are directly related to their β -decay half-lives. If the r -process flow reaches isotopes with neutron-magic numbers, these isotopes will usually represent waiting points due to their relatively small Q -values for the neutron-capture reactions. After the β decay, the reaction flow in the next isotopic chain will again be halted at the same neutron-magic number. Thus, the r -process will move vertically upward in proton number until the Q -value for neutron capture is sufficiently large to overcome the neutron-magic nuclei. As the process path approaches the valley of stability, the half-lives of the corresponding waiting points will increase. The reaction flow, therefore, will be significantly delayed at these relatively long-lived isotopes leading to an accumulation of abundances.

As the process finally *freezes out*, neutron density rapidly decreases, and the produced isotopes decay back to the valley of stability and populate the r -only isotopes amongst others (see Fig. 2.3). This explains the abundance peaks shown in Fig. 2.1 at mass numbers of $A = 80, 130$ and 195 shifted relative to the s -abundance peaks. In analogy to the s process, it is important to mention that the r process is not able to synthesize all of the observed stable isotopes beyond iron. Some of them are shielded by their neutron-rich isobars against the β decay during freeze-out and, hence, can only be produced in the s process. Accordingly, these isotopes are referred to as s -only isotopes. More details about the r process are given, e. g., in Ref. [21].

The p process

Calculations of advanced theoretical nucleosynthesis models based on many observational data have shown that each the s and r process produce about 50% of the observed abundances. How-

ever, about 35 stable proton-rich isotopes, the so-called *p* nuclei, cannot be produced in either of these two processes (e. g., see $^{156,158}\text{Dy}$ of Fig. 2.3). Although these isotopes generally only represent a small fraction of the total abundance, another process is required to account for these relatively rare nuclei. This process has been postulated to be the so-called *p* process. Contributions from many different reaction mechanisms, such as radiative proton captures of lighter elements, have been under discussion. However, the following discussion will be restricted to photodisintegration, which is believed to be the most promising mechanism for the production of *p* nuclei with mass numbers $A > 100$.

Under explosive conditions, e. g., in Type II supernovae, temperatures of up to $T = 2 - 3 \times 10^9$ K give rise to a dense high-energetic photon bath. These photons are able to photodisintegrate a certain seed distribution of heavy nuclei via (γ, n) , (γ, p) , and (γ, α) reactions. Close to the valley of stability, (γ, n) reactions dominate the reaction flow moving the process path away to more and more neutron-deficient nuclei. As neutron number decreases in an isotope sequence, (γ, p) and (γ, α) reactions become competitive giving rise to branchings in the reaction flow. Thus, a rather complex reaction network emerges involving thousands of reactions. Finally, in analogy to the *r* process, the synthesized nuclei will decay back to the valley of stability and populate the *p* nuclei amongst others.

As already mentioned, the contributions of the *p* process to the abundances of most of the isotopes being produced in the *s* and *r* processes are usually rather small. This is indicated by the small relative abundances of the *p* nuclei, typically less than one percent. However, in some cases large contributions are expected, e. g., a 33% contribution is predicted for the *s*-only nucleus ^{152}Gd [7]. A detailed description of the *p* process is given by the articles of Refs. [22, 23].

In conclusion, the preceding discussions indicate that many different processes have an impact on the nucleosynthesis of heavy elements. Therefore, to quantitatively test the outcome of a certain theoretical model, it is most suitable to investigate those nuclei produced mainly in a single process, such as the *s*-only, *r*-only and *p* isotopes. However, to address all features of the abundance pattern, it is mandatory to explicitly take into account all processes.

2.1.4 Photodisintegration in the nucleosynthesis of heavy elements

Whenever a nucleosynthetic process is governed by very high temperatures, photodisintegration reactions will be induced by the high-energetic photon bath, whose spectral distribution is described by a Planck distribution:

$$n_{\gamma}^{\text{Planck}}(E_{\gamma}, T) dE_{\gamma} = \left(\frac{1}{\pi}\right)^2 \left(\frac{1}{\hbar c}\right)^3 \frac{E_{\gamma}^2}{\exp(E_{\gamma}/kT) - 1} dE_{\gamma} \quad , \quad (2.1)$$

where $n_{\gamma}^{\text{Planck}}$ denotes the density of photons of energy E_{γ} per energy interval in a photon bath of temperature T . For photon energies much larger than the thermal energy, i. e., $E_{\gamma} \gg kT$, the

photon density exponentially decreases with energy E_γ and increases with temperature T . Thus, the impact of photodisintegration reactions on any nucleosynthetic process sensitively depends on the binding energies of isotopes along the reaction flow and on the physical conditions of the stellar environment.

In the preceding sections, it was outlined that the r and p processes presumably proceed under the explosive conditions of supernovae giving rise to a significant contribution of photodisintegration reactions. As discussed, photodisintegration has shown to be the dominating mechanism in the p process for isotopes of mass $A > 100$. Furthermore, the r process reaction path is shaped by photodisintegration when photoneutron reactions become competitive with neutron capture due to the small neutron binding energies of very neutron-rich isotopes. Only in the s process, photodisintegration has no direct impact on the reaction flow because the temperature is relatively moderate.

Nevertheless, when reaction rates need to be calculated for nucleosynthesis networks, theoreticians often make use of the *principle of detailed balance* [24] to directly relate a reaction rate to its inverse reaction rate under stellar conditions. Consider a photodisintegration reaction of type $m(\gamma, j)i$. According to Ref. [25], one obtains:

$$\lambda_\gamma^* = \left(\frac{A_i A_j}{A_m} \right)^{3/2} \frac{(2J_i^0 + 1)(2J_j^0 + 1)}{(2J_m^0 + 1)} \frac{G_i(T) G_j(T)}{G_m(T)} \left(\frac{kT}{2\pi N_A \hbar^2} \right)^{3/2} \times \exp(-Q/kT) \langle \sigma_i^* v \rangle, \quad (2.2)$$

where N_A is the Avogadro constant, A and J^0 denote mass and ground-state spin, respectively, Q quotes the Q -value of the inverse reaction, and λ_γ^* and $\langle \sigma_i^* v \rangle$ are the reaction rates of the photodisintegration reaction and its inverse reaction at a given stellar temperature T , respectively. Furthermore, $G(T)$ denotes the temperature-dependent normalized partition function given by $G(T) = \frac{1}{2J^0 + 1} \sum_\mu (2J^\mu + 1) \exp(-E^\mu/kT)$, where one has to sum over all levels μ of energy E^μ and spin J^μ .

For numerical reasons, the reaction rate is often calculated in the direction of positive Q -value, and the inverse rate is determined from Eq. (2.2) afterwards. From an experimental point of view, for many reactions, the rate in only one direction can be studied in the laboratory for various experimental reasons, and Eq. (2.2) can then be applied to derive the inverse rate from experimental data. Therefore, one could also consider to determine neutron-capture rates for the s process via the measurement of photoneutron reactions. In particular, this would be an interesting approach for the investigation of short-lived branching points because these isotopes cannot be studied in neutron-capture experiments as outlined in Ref. [19].

However, it is important to clarify that Eq. (2.2) only holds for stellar reaction rates accounting for the thermal population of excited states in both target and residual nucleus. This has been illustrated, e. g., in Ref. [26]. For this reason, the applicability of Eq. (2.2) for measurements under laboratory conditions will be critically discussed in the next section.

2.2 Astrophysical implication of ground-state reaction rates

Due to the high temperatures during nucleosynthetic processes, low-lying levels of every nucleus located in the stellar environment will be thermally populated according to the Maxwell-Boltzmann distribution. Therefore, the stellar cross section of any reaction of type $i(j,o)m$ is generally given by:

$$\sigma^*(E_{ij}) = \frac{\sum_{\mu} (2J_i^{\mu} + 1) \exp(-E_i^{\mu}/kT) \sum_{\nu} \sigma^{\mu\nu}(E_{ij})}{\sum_{\mu} (2J_i^{\mu} + 1) \exp(-E_i^{\mu}/kT)} , \quad (2.3)$$

where E_{ij} denotes the center-of-mass energy. The indices μ and ν refer to the states of spin J and energy E in the target nucleus i and reaction product m , respectively. For simplification, projectile and ejectile are assumed to have no excited states. This is obviously fulfilled when only protons, neutrons, α particles, and photons are taken into consideration at astrophysically relevant energies. Note that a temperature of 3×10^9 K corresponds to a thermal energy of $kT \approx 259$ keV.

Under laboratory conditions, thermal excitations of the nucleus are negligible. Using $T \approx 0$ K, Eq. (2.3) reduces to:

$$\sigma(E_{ij}) \approx \sum_{\nu} \sigma^{0\nu}(E_{ij}) . \quad (2.4)$$

Thus, the cross section measured under laboratory conditions only addresses transitions starting from the ground state of the target nucleus.

The enhancement of the stellar reaction rate in comparison to the reaction rates determined in the laboratory is accounted for by the so-called *stellar enhancement factor*:

$$\text{SEF} = \frac{\langle \sigma^* \nu \rangle}{\langle \sigma \nu \rangle} , \quad (2.5)$$

where $\langle \sigma \nu \rangle$ and $\langle \sigma^* \nu \rangle$ denote ground-state and stellar reaction rate, respectively. For capture reactions, the stellar rate $\langle \sigma^* \nu \rangle$ is directly related to the so-called *Maxwellian Averaged capture Cross Section* (MACS) via $\text{MACS} = \frac{\langle \sigma^* \nu \rangle}{v_T}$, where v_T denotes the mean relative velocity between target and projectile at temperature T . In analogy, the stellar enhancement factor for photodisintegration reactions is defined by:

$$\text{SEF} = \frac{\lambda_{\gamma}^*}{\lambda_{\gamma}} . \quad (2.6)$$

Using Eq. (2.5) and Eq. (2.6), stellar reaction rates can be derived from the experimentally determined ones. These rates can then also be used to calculate the inverse reaction rates via the

principle of detailed balance according to Eq. (2.2). Unfortunately, the stellar enhancement factor can usually only be adopted from theory and uncertainties of the calculations also give rise to additional uncertainties in the derived stellar reaction rates. Therefore, the determination of stellar reaction rates from experimental data only seems reasonable if the stellar enhancement is rather small so that the overall uncertainties for the reaction rates are not dominated by the uncertainties of the theoretical models. In the following, the stellar enhancement of photodisintegration rates will be discussed.

The photodisintegration reaction rate per nucleus in a stellar environment of temperature T is given by:

$$\lambda^*(T) = c \int n_{\gamma}^{\text{Planck}}(E_{\gamma}, T) \sigma^*(E_{\gamma}) dE_{\gamma}, \quad (2.7)$$

where $n_{\gamma}^{\text{Planck}}$ denotes the Planck distribution of Eq. (2.1), σ^* is the stellar cross section of Eq. (2.3), and c is the velocity of light. Technically, the integral has to be evaluated for the whole energy range up to infinite photon energies. However, due to the exponentially decreasing photon density for energies $E_{\gamma} \gg kT$, large contributions to the reaction rate are only expected in a small energy window close to the reaction threshold. This is illustrated in Fig. 2.4 for the case of the ground-state photoneutron reaction rate of ^{154}Sm . In analogy to the reaction window found for charged-particle reactions, this energy window is often referred to as the *Gamow-like window*.

For further discussion, the stellar reaction rate λ^* can be written as a sum of the contributions stemming from each level of energy E_i^{μ} and spin J_i^{μ} in the target nucleus. Using Eq. (2.3) and Eq. (2.7), one obtains:

$$\begin{aligned} \lambda^*(T) &= c \int n_{\gamma}^{\text{Planck}}(E_{\gamma}, T) \frac{\sum_{\mu} (2J_i^{\mu} + 1) \exp(-E_i^{\mu}/kT) \sum_{\nu} \sigma^{\mu\nu}(E_{\gamma})}{\sum_{\mu} (2J_i^{\mu} + 1) \exp(-E_i^{\mu}/kT)} dE_{\gamma} \\ &= \frac{\sum_{\mu} (2J_i^{\mu} + 1) \exp(-E_i^{\mu}/kT) \sum_{\nu} \lambda^{\mu\nu}(T)}{\sum_{\mu} (2J_i^{\mu} + 1) \exp(-E_i^{\mu}/kT)} \\ &= \frac{\sum_{\mu} (2J_i^{\mu} + 1) \exp(-E_i^{\mu}/kT) \lambda^{\mu}(T)}{\sum_{\mu} (2J_i^{\mu} + 1) \exp(-E_i^{\mu}/kT)}, \end{aligned} \quad (2.8)$$

where $\lambda^{\mu\nu}(T) = \int n_{\gamma}^{\text{Planck}}(E_{\gamma}, T) \sigma^{\mu\nu} dE_{\gamma}$ and $\lambda^{\mu}(T) = \sum_{\nu} \lambda^{\mu\nu}(T)$. In the laboratory, it is only possible to measure the ground-state reaction rate $\lambda^{\text{g.s.}} = \lambda^0$. Thus, with regard to Eq. (2.8), the stellar enhancement factor is given by:

$$\text{SEF}(T) = \frac{\lambda^*(T)}{\lambda^{\text{g.s.}}} = \frac{1}{G_i(T)} \sum_{\mu} \underbrace{\frac{2J_i^{\mu} + 1}{2J_i^0 + 1} \exp(-E_i^{\mu}/kT) \frac{\lambda^{\mu}(T)}{\lambda^0}}_{f^{\mu}(T)}, \quad (2.9)$$

where $G_i(T)$ is the normalized partition function defined in the preceding section, and f^{μ} is the contribution of each state to the SEF.

To derive some qualitative features of f^{μ} , some simplifications will be applied. First, it is assumed that the reaction threshold S_x is rather large with regard to the thermal energy, i. e., $S_x \gg kT$. Furthermore, only low-energetic initial states in the target nucleus are taken into consideration so that $S_x \gg E_i^{\mu}$. Therefore, $E_{\gamma} \gg kT$ for terms contributing to the integral of Eq. (2.9) because $\sigma^{\mu\nu}$ only has non-zero values for photons of energy $E_{\gamma} \geq S_x - E_i^{\mu}$. Thus, the Planck distribution becomes proportional to $E_{\gamma}^2 \times \exp(-E_{\gamma}/kT)$ and f^{μ} can be approximated by:

$$\begin{aligned} f^{\mu}(T) &\approx \frac{2J_i^{\mu} + 1}{2J_i^0 + 1} \exp(-E_i^{\mu}/kT) \frac{\int_{S_x - E_i^{\mu}}^{\infty} E_{\gamma}^2 \exp(-E_{\gamma}/kT) \sum_{\nu} \sigma^{\mu\nu}(E_{\gamma}) dE_{\gamma}}{\int_{S_x}^{\infty} E_{\gamma}^2 \exp(-E_{\gamma}/kT) \sum_{\nu} \sigma^{0\nu}(E_{\gamma}) dE_{\gamma}} \\ &= \frac{2J_i^{\mu} + 1}{2J_i^0 + 1} \exp(-E_i^{\mu}/kT) \frac{\int_{S_x}^{\infty} (E_{\gamma} - E_i^{\mu})^2 \exp(-(E_{\gamma} - E_i^{\mu})/kT) \sum_{\nu} \sigma^{\mu\nu}(E_{\gamma} - E_i^{\mu}) dE_{\gamma}}{\int_{S_x}^{\infty} E_{\gamma}^2 \exp(-E_{\gamma}/kT) \sum_{\nu} \sigma^{0\nu}(E_{\gamma}) dE_{\gamma}} \\ &= \frac{2J_i^{\mu} + 1}{2J_i^0 + 1} \frac{\int_{S_x}^{\infty} (E_{\gamma} - E_i^{\mu})^2 \exp(-E_{\gamma}/kT) \sum_{\nu} \sigma^{\mu\nu}(E_{\gamma} - E_i^{\mu}) dE_{\gamma}}{\int_{S_x}^{\infty} E_{\gamma}^2 \exp(-E_{\gamma}/kT) \sum_{\nu} \sigma^{0\nu}(E_{\gamma}) dE_{\gamma}}. \end{aligned} \quad (2.10)$$

Note that a transformation of the integration limits has been performed in the second step of Eq. (2.10). If one further estimates that $(E_{\gamma} - E_i^{\mu})^2 \approx E_{\gamma}^2$ and assumes that the cross section is rather independent of the initial state μ , i. e., $\sigma^{\mu\nu}(E_{\gamma} - E_i^{\mu}) \approx \sigma^{0\nu}(E_{\gamma})$, one finally obtains:

$$f^{\mu}(T) \approx \frac{2J_i^{\mu} + 1}{2J_i^0 + 1}. \quad (2.11)$$

This is an amazing result. It shows that each state in the target nucleus gives approximately the same contribution to the SEF and, thus, to the stellar reaction rate independent of stellar temperature T and level energy E_i^{μ} . Qualitatively, this can be understood with regard to the fact that the exponential increase of photon density $n_{\gamma}^{\text{Planck}}$ with decreasing reaction threshold

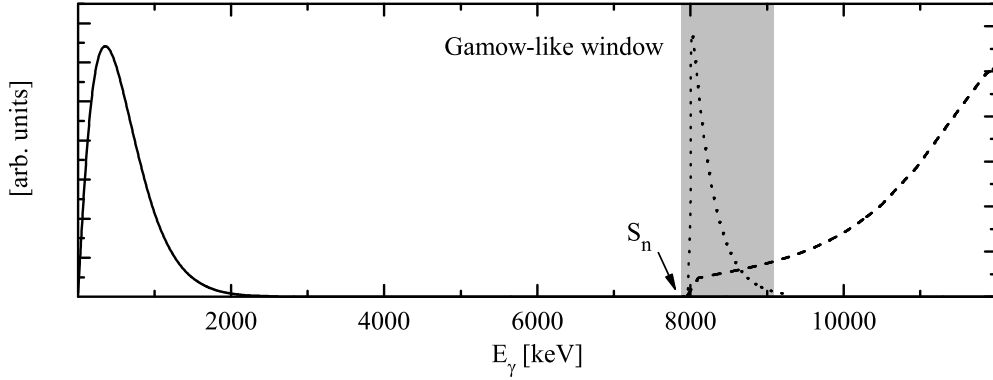


Fig. 2.4: Astrophysically relevant energy window for photoneutron reactions. The solid line shows a Planck distribution $n_{\gamma}^{\text{Planck}}$ at a temperature of $T = 2.5 \times 10^9$ K, which is typical for the stellar environment during the p process. The dashed line shows the ground-state photoneutron cross section σ for ^{154}Sm calculated with the NON-SMOKER^{WEB} code [27]. The reaction rate is determined by the product $n_{\gamma}^{\text{Planck}} \times \sigma$ (dotted line) showing only significant contributions in a small energy window just above the neutron threshold, the so-called *Gamow-like window*.

$S_x - E_i^{\mu}$ is balanced by the exponential decrease of the Maxwell-Boltzmann distribution with increasing energy E_i^{μ} .

According to Eq. (2.9), the SEF is approximately given by:

$$\text{SEF} \approx \frac{1}{G_i(T)} \sum_{\mu} \frac{2J_i^{\mu} + 1}{2J_i^0 + 1} \quad (2.12)$$

Because a very large number of states is usually involved in the reaction and $G_i(T)$ is rather small under stellar temperatures (see Fig. 2.5), Eq. (2.12) implies that the stellar enhancement factor can be expected to be huge. This indicates the difficulty to derive stellar photodisintegration rates from experimentally determined ground-state reaction rates because the latter only make up a small fraction of the total reaction rates under stellar conditions. Although the result from Eq. (2.11) has been derived under rather strong assumptions, the qualitative features can be confirmed by detailed theoretical calculations as illustrated in Tab. 2.1.

The preceding discussion has been based on the assumption that the Q -value of the reaction is negative and large compared to the thermal energy. This applies to most photodisintegration reactions involved in the nucleosynthesis reaction networks. However, with regard to the inverse reaction such as neutron capture, it is interesting to discuss the stellar enhancement for reactions of positive Q -value. In analogy to Eq. (2.10), one obtains:

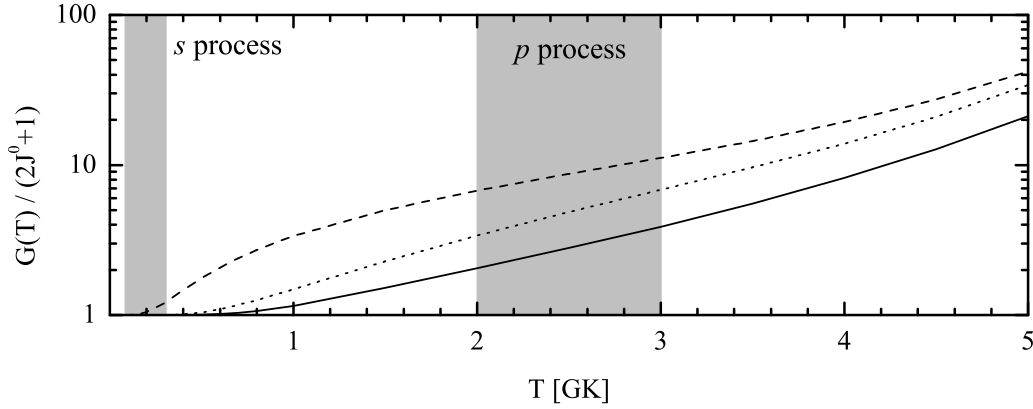


Fig. 2.5: Normalized partition function $G(T)$ as a function of temperature for ^{148}Nd (solid line), ^{154}Sm (dashed line) and ^{192}Os (dotted line). $G(T)$ has been adopted from Ref. [25]. The gray-shaded areas indicate temperatures typical for the s and p process, respectively. The partition functions are close to unity at s -process temperatures and increase rather slowly with temperature.

$$f^\mu(T) = \frac{2J_i^\mu + 1}{2J_i^0 + 1} \exp(-E_i^\mu/kT) \frac{\int_0^\infty v \Phi(v, T) \sum_v \sigma^{\mu v}(v) dv}{\int_0^\infty v \Phi(v, T) \sum_v \sigma^{0v}(v) dv} , \quad (2.13)$$

where v is the relative velocity between target nucleus and projectile, and Φ denotes the Maxwellian velocity distribution. Again, if one assumes the cross section to be rather independent of the initial state in the target nucleus, i. e., $\sigma^{\mu v} \approx \sigma^{0v}$, the equation further reduces to:

$$f^\mu(T) \approx \frac{2J_i^\mu + 1}{2J_i^0 + 1} \exp(-E_i^\mu/kT) . \quad (2.14)$$

In contrast to the result of Eq. (2.11), one finds that excited states in the target nucleus only make up a small fraction of the stellar reaction rate depending sensitively on the temperature of the stellar environment and on the level energy E_i^μ . At moderate temperatures, e. g., during the s process, the stellar rate, thus, will be strongly dominated by the ground-state reaction rate. According to Eq. (2.9), the SEF is approximately given by:

$$\text{SEF} \approx \frac{1}{G_i(T)} \sum_\mu \frac{2J_i^\mu + 1}{2J_i^0 + 1} \exp(-E_i^\mu/kT) = 1 , \quad (2.15)$$

which shows that the SEF is expected to be close to unity. Eq. (2.15) has been derived under the rather strong assumption that all cross sections $\sigma^{\mu v}$ are equal. However, detailed calculations treating each cross section $\sigma^{\mu v}$ individually confirm that the stellar enhancement is usually small [25].

^{148}Nd			
$T [10^9 \text{ K}]$	$\lambda^{\text{g.s.}}$	λ^*	SEF
2.0	1.20×10^{-2}	6.53×10^0	5.44×10^2
2.5	8.62×10^1	3.78×10^4	4.38×10^2
3.0	3.39×10^4	1.16×10^7	3.41×10^2

^{154}Sm			
$T [10^9 \text{ K}]$	$\lambda^{\text{g.s.}}$	λ^*	SEF
2.0	6.53×10^{-4}	4.95×10^{-1}	7.54×10^2
2.5	9.21×10^0	6.44×10^3	6.99×10^2
3.0	5.65×10^3	3.51×10^6	6.21×10^2

^{192}Os			
$T [10^9 \text{ K}]$	$\lambda^{\text{g.s.}}$	λ^*	SEF
2.0	4.88×10^{-3}	3.53×10^0	7.24×10^2
2.5	4.55×10^1	2.55×10^4	5.60×10^2
3.0	2.12×10^4	9.25×10^6	4.36×10^2

Tab. 2.1: The stellar photoneutron rate λ^* for three different nuclei is compared to the photoneutron ground-state reaction rate $\lambda^{\text{g.s.}}$. The rates are quoted in units of s^{-1} . $\lambda^{\text{g.s.}}$ has been calculated using the NON-SMOKER^{WEB} code [27], and λ^* has been derived from the parametrization of Ref. [25] also based on the NON-SMOKER code. The stellar enhancement factor SEF is found to be large and only weakly dependent on temperature. See text for more details.

In conclusion, one needs to be very careful when experimental data is adopted for astrophysical studies due to the stellar enhancement of reaction rates. The stellar enhancement factor has turned out to be very large for reactions of large negative Q -values such as photodisintegration reactions. This gives rise to large uncertainties when experimentally determined reaction rates are extrapolated to stellar rates. On the other hand, reactions of positive Q -value have shown a very small stellar enhancement. Thus, the large amount of neutron-capture data provided by experiments in the last decades [11] can be almost directly adopted for the reaction network of the s process exhibiting only rather small uncertainties. Furthermore, it seems to be more reliable to derive stellar photodisintegration reaction rates for the p process from experimental rates of the inverse reactions by applying the principle of detailed balance according to Eq. (2.2) rather than to derive those rates from experimental photodisintegration data.

Apparently, direct measurements of stellar photodisintegration reaction rates cannot be per-

formed. Nevertheless, photodisintegration experiments are an excellent tool to test the predictive power of theoretical calculations for a wide range of nuclei, at least for ground-state reaction rates. Experimental data for photodisintegration reactions in the astrophysically relevant energy region are still rare but are mandatory to constrain and improve the nuclear models adopted for theoretical calculations. By improving the nuclear physics input, one will increase the reliability and accuracy of theoretical predictions for ground-state reaction rates as well as for stellar reaction rates. This will be further discussed in the next section.

2.3 Theoretical basics of reaction-rate calculations

Theoretical predictions of reaction rates are indispensable for astrophysical studies and calculations of nucleosynthesis networks. Though desirable, it is impossible to provide reliable highly accurate experimental data for each reaction involved in the networks. Obviously, experiments can not address each of the thousands of reactions needed for astrophysical studies. Moreover, experimental studies are further hampered by the fact that many of the nuclei with astrophysical implication are unstable and difficult to access in the laboratory. Finally, even if every single reaction was measured in the experiment, one would still have to account for the stellar enhancement of the determined rates.

As mentioned, the stellar enhancement factor can only be derived from theoretical calculations. Most of the astrophysical investigations, therefore, have to rely on theoretical models. It is the task of experimentalists to exemplarily check the reliability of theoretical predictions on the basis of those reactions accessible in the laboratory and to provide improved input from nuclear physics to enhance the theoretical models.

Predictions of reaction rates for middleweight and heavy nuclei usually make use of the statistical model based on the theory of Hauser and Feshbach [6]. The basic ideas of the statistical model will be presented in the following section. The reliability of calculations within this model is mainly determined by the nuclear physics input adopted for the theoretical codes. Therefore, in Sec. 2.3.2, the nuclear models applied for two advanced statistical model codes will be summarized. The predictions stemming from these theoretical codes serve as the basis for comparison with experimental data provided in Chapter 4.

2.3.1 The statistical model

Nuclear reactions of rather low energy are usually dominated by *compound-nucleus* reactions. In these reactions, the target nucleus and projectile form an excited compound system which has a lifetime much longer than the typical transit time of the projectile before decaying into one of the energetically allowed reaction channels. The kinetic energy of the incident projectile is assumed to be statistically divided among the nucleons in the compound nucleus rather than being transferred to one or a few nucleons. Thus, metaphorically speaking, the compound nucleus

loses any memory of its formation making the decay of the compound system independent of the process of formation except for spin conservation. Therefore, the cross section of a reaction of type $i^\mu(j,o)m^\nu$ can be written – neglecting spin conservation – as the product of formation and decay:

$$\sigma^{\mu\nu} = \sigma_{(\text{CN})}^\mu P^\nu = \frac{\lambda^2}{4\pi^2} T_j^\mu P^\nu \quad , \quad (2.16)$$

where $\sigma_{(\text{CN})}^\mu$ denotes the cross section for the formation of the compound nucleus from the initial nucleus i^μ , and T_j^μ is the transmission coefficient. The probability of the decay of the compound system P^ν to the residual nucleus m^ν can be determined from the reciprocity theorem [28]. Finally, for comparison with experimental data, one has to take into account that the reaction involves many compound states of various spin J and parity π that can be excited. The statistical model presumes that the corresponding wave functions of the various transitions have random phases. Thus, averaging over many states will highly suppress any interference terms, and $\sigma^{\mu\nu}$ is simply determined by the sum over all participating compound states [25]:

$$\begin{aligned} \sigma^{\mu\nu}(E_{ij}) = & \frac{\pi\hbar^2/(2\mu_{ij}E_{ij})}{(2J_i^\mu+1)(2J_j+1)} \sum_{J,\pi} (2J+1) \\ & \times \frac{T_j^\mu(E, J, \pi, E_i^\mu, J_i^\mu, \pi_i^\mu) T_o^\nu(E, J, \pi, E_m^\nu, J_m^\nu, \pi_m^\nu)}{T_{\text{tot}}(E, J, \pi)} \quad . \end{aligned} \quad (2.17)$$

This formula now takes into account spin and parity conservation rules. The center-of-mass energy and the reduced mass are denoted by E_{ij} and μ_{ij} . For the notation used in Eq. (2.17), see Fig. 2.6. T_j^μ and T_o^ν are the transmission coefficients for the formation and decay of the compound state, respectively.

The total transmission coefficient T_{tot} is a sum over all energetically allowed exit channels α into bound and unbound states β of the residual nucleus and, hence, given by $T_{\text{tot}} = \sum_{\alpha,\beta} T_\alpha^\beta$. However, in many cases the number of allowed final states is huge making it impossible to treat each state individually. Therefore, the sum over all final states β of a certain reaction channel α is usually divided into:

$$\begin{aligned} \sum_\beta T_\alpha^\beta(E, J, \pi) = & \sum_{\beta=0}^{\beta_m} T_\alpha^\beta(E, J, \pi, E^\beta, J^\beta, \pi^\beta) + \\ & \int_{E^{\beta_m}}^{E-S_\alpha} \sum_{J', \pi'} \rho_\alpha(E', J', \pi') T_\alpha(E, J, \pi, E', J', \pi') dE' \quad . \end{aligned} \quad (2.18)$$

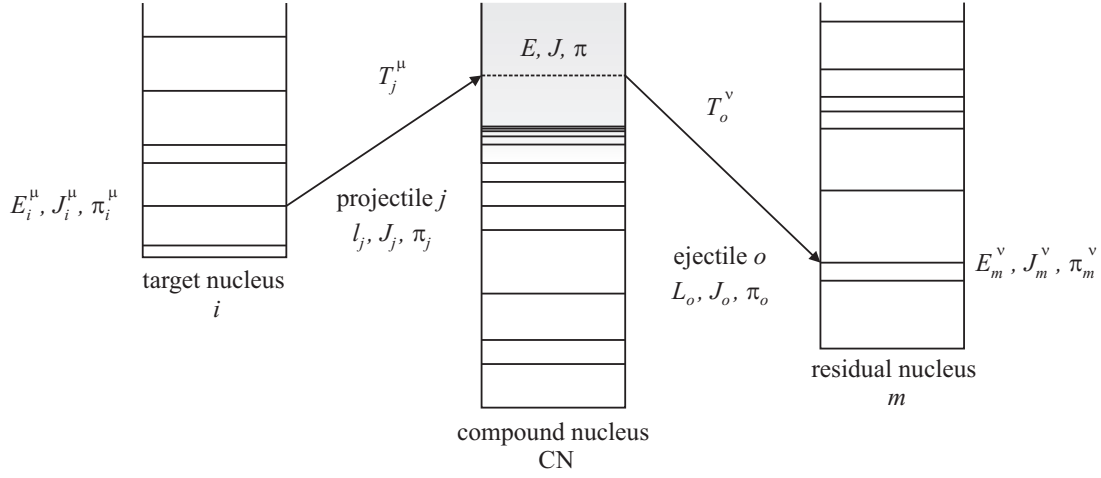


Fig. 2.6: Schematic figure of a compound-state reaction of type $i^\mu(j,o)m^\nu$. Projectile j of angular momentum l_j , spin J_j , and parity π_j and target nucleus in initial state μ of energy E_i^μ , spin J_i^μ , and parity π_i^μ form a compound state of energy E , spin J , and parity π . The compound state then decays by the emission of ejectile o of angular momentum l_o , spin J_o , and parity π_o into the residual nucleus in final state ν of energy E_m^ν , spin J_m^ν , and parity π_m^ν . The corresponding transmission coefficients are denoted by T_j^μ and T_o^ν , respectively. The gray-shaded area indicates a high level density in the compound nucleus.

The sum of the first term is evaluated for all states of known spin and parity up to the level β_m , where these quantum numbers are either uncertain or the density of levels becomes too high to treat each state separately. Final states of energies larger than E^{β_m} are accounted for by the integral of the second term. S_α is the channel separation energy, ρ_α denotes the level density of the residual nucleus, and T_α describes an averaged transmission coefficient. The level density is adopted from theoretical models or from an empirical fit to experimental data.

The sum of Eq. (2.17) has to be evaluated for all quantum numbers allowed from parity and spin conservation. Furthermore, the transmission coefficients T_j^μ can be divided into a summation over all quantum-mechanically allowed partial waves:

$$T_j^\mu(E, J, \pi, E_i^\mu, J_i^\mu, \pi_i^\mu) = \sum_{l=|J-s|}^{J+s} \sum_{s=|J_i^\mu-J_j|}^{J_i^\mu+J_j} T_{jls}(E_{ij}^\mu) \quad (2.19)$$

Eq. (2.19) already accounts for the fact that the angular momentum \vec{l} and the channel spin $\vec{s} = \vec{J}_j + \vec{J}_i^\mu$ couple to the compound-state spin $\vec{J} = \vec{l} + \vec{s}$. For example, assume a compound state of $J = 3/2$ is formed by neutron capture on an initial target state of $J_i^\mu = 0$. Since $J_j = 1/2$ for neutrons, the channel spin is also $s = 1/2$. Hence, the angular momentum must be either $l = 1$ or $l = 2$, i. e., the neutron capture is described by a p wave or d wave, respectively. Further constraints could be derived from parity conservation.

In case of particle capture or emission, the transmission coefficients T_{jls} are calculated from solving the Schrödinger equation by the use of an appropriate optical-model potential, which describes the particle-nucleus interaction. For the excitation or de-excitation by photons, the transmission coefficients have to be derived from the total photon width or γ -ray strength function, respectively. For many calculations, it is sufficient to include only the dominant E1 and M1 transitions. E1 transitions are usually calculated on the basis of a Lorentzian representation of the giant dipole resonance. M1 transitions are much smaller and are usually calculated within a simple single particle approach. In addition, for both the particle and radiative transmission coefficients, a so-called *width fluctuation correction* is applied. This correction accounts for the fact that the processes of formation and decay are not completely independent of each other as assumed in Eq. (2.17). It becomes important for an accurate description near reaction thresholds.

Finally, some considerations need to be given to the applicability of the statistical model. As mentioned, the model assumes that the density of levels is high enough for a statistical treatment, approximately $5 - 10 \text{ MeV}^{-1}$. This is fulfilled for almost all heavy nuclei. However, one has to be careful when calculating reaction rates of light nuclei or nuclei near shell closures. Furthermore, the statistical model presumes that the energy of the incident particle is not too large ($E_{\text{kin}} < 20 \text{ MeV}$). In general, energies of astrophysical implication are far below this critical energy. More details about statistical model calculations can be found, e. g., in Refs. [25, 28, 29].

2.3.2 Nuclear physics input

Today, a large number of theoretical model codes based on the Hauser-Feshbach formalism is available. Whereas the Hauser-Feshbach theory itself is well established, different predictions between the various codes can mainly be ascribed to the adopted nuclear physics input, e. g., optical-model potentials, nuclear level densities and γ -ray strength functions. The sensitivity of the results to the various input parameters will be discussed in more detail in Chapter 5.

The aim of some theoretical codes is to predict reaction rates reliably for a wide range of isotopes without adjusting the nuclear input parameters to local experimental data. The use of global nuclear parameters is essential especially for astrophysical investigations because in many cases nuclei far from the valley of stability are involved in the reaction network where no empirical data is available.

In this thesis, the predictions of two advanced statistical model codes, the TALYS code by Koning *et al.* [30] and the NON-SMOKER^{WEB} code by Rauscher [27], will be compared with experimental data. Therefore, the default nuclear models recommended by the authors of the codes have been used for the calculations. Details of these models will not be discussed here but will be summarized in the following for the sake of completeness. For more details, the reader is referred to the given references.

The NON-SMOKER^{WEB} code involves the neutron optical-model potential published by Jeukenne *et al.* [31] with a low-energy modification by Lejeune [32]. The γ -ray strength function is based on a description by Thielemann and Arnould [33] using experimental GDR energies and widths if available and the low-energy modification of the GDR Lorentzian by McCullagh *et al.* [34]. For the nuclear level density, a global parametrization within the back-shifted Fermi-gas formalism by Rauscher *et al.* [35] is applied.

The TALYS code uses the neutron optical-model potential parameterizations of Koning and Delaroche [36]. The γ -ray strength function is obtained from the compilation by Kopecky and Uhl [37], and the nuclear level density is also based on an approach using the Fermi-gas model [38]. Both the TALYS code and the NON-SMOKER^{WEB} code employ the Constant Temperature Model from Gilbert and Cameron [39] for the nuclear level density to avoid the divergence of the Fermi-gas model at low excitation energies.

Chapter 3

Photoactivation experiments at the S-DALINAC

In the last decade, several photoactivation experiments have been performed at the superconducting Darmstadt electron linear accelerator S-DALINAC [40] to study photodisintegration reactions close to the particle threshold. In this chapter, the experimental technique of photoactivation will be explained followed by a comprehensive description of the data analysis. This well-established technique has already been presented in previous works, e. g., see Refs. [26, 41].

However, compared to previous works, this chapter rather intends to deliver a deep and transparent insight into the main uncertainties of the data analysis. Since the analysis requires the use of various Monte Carlo simulations, it is essential to be aware of systematic uncertainties stemming from these simulations. In the past, exclusively the Monte Carlo code GEANT3 [42] was applied, which, unfortunately, showed discrepancies in several descriptions, in particular for the description of the spectral shape of bremsstrahlung. Therefore, all simulations of this work have been performed with the improved Monte Carlo code GEANT4 [43]. The reliability of these simulations will be discussed in detail.

At the end of this chapter, an overview of the experimental uncertainties will be given. Due to the fact that a significant contribution stems from uncertainties of the beam energy determination, several experimental techniques are presented and compared to each other with the aim to constrain this uncertainty.

3.1 Experimental technique

The experiments presented in this thesis have been performed at the *Nuclear Resonance Fluorescence* (NRF) setup at the superconducting electron linear accelerator S-DALINAC. This setup is located straight behind the injector of the accelerator and will be referred to as the *photoactivation setup* in the context of this thesis [44]. A schematic layout of the S-DALINAC is shown in Fig. 3.1. At the photoactivation setup the accelerator provides a monoenergetic electron beam of energies up to $E_0 = 10.5$ MeV with an energy spread of about 25 keV at a maximum beam current of $60 \mu\text{A}$. According to Fig. 3.2, the monoenergetic electron beam is stopped completely in a thick copper radiator and produces a continuous spectrum of bremsstrahlung photons with a maximum energy of $E_{\text{max}} = E_0$. In the following, the notation E_{max}

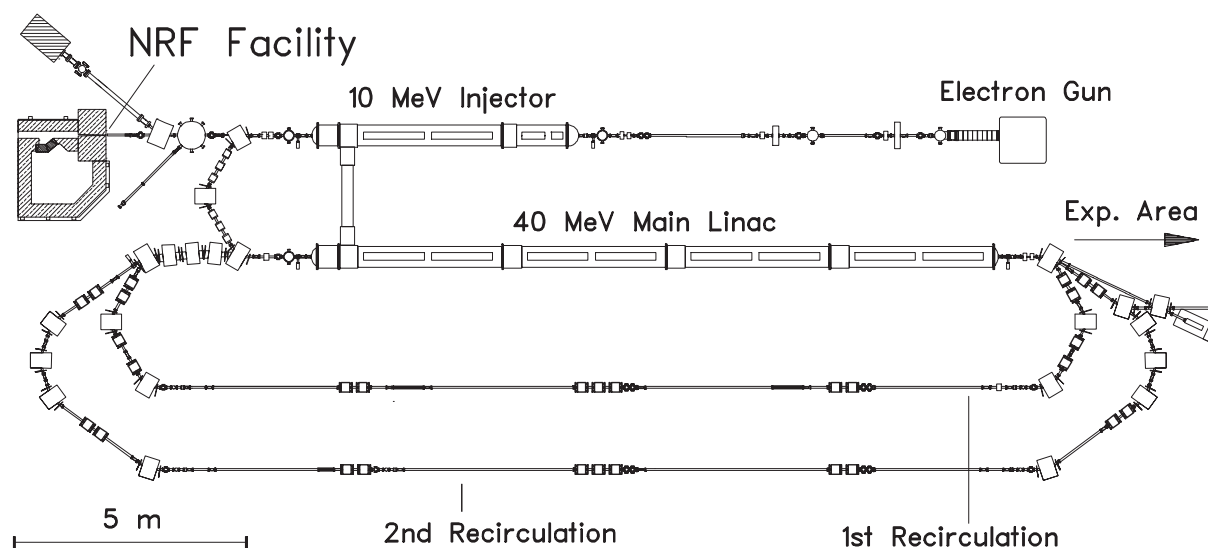


Fig. 3.1: Schematic layout of the superconducting Darmstadt electron linear accelerator S-DALINAC.

Electrons are emitted by an electron gun with an energy of about 250 keV and then formed to bunches of 3 GHz time structure in a chopper and prebuncher system using the so-called cw-mode. The electron bunches are accelerated by superconducting high-frequency cavities made out of high-purity niobium and cooled by liquid helium at 2 K. Behind the injector, a beam of energy up to 10.5 MeV and with currents up to $60 \mu\text{A}$ can be provided at the *Nuclear Resonance Fluorescence* (NRF) setup for experiments with real photons, e. g., photon-scattering and photoactivation experiments. For higher energies, the electrons need to be deflected into the main accelerator. This yields a beam of energy up to 130 MeV due to the possibility of two recirculations. The beam can be extracted to a separate experimental area after each passing of the main linac.

will be used in the context of the photon spectrum only, whereas E_0 is used to refer to the kinetic beam energy.

Conventionally, the beam energy is adjusted with a well-calibrated 40° deflecting magnet in front of the radiator. This does not allow for an online control of the beam energy during the irradiation so that the experiment is usually interrupted periodically to correct energy drifts if necessary. More details about the determination of beam energy will be given in Sec. 3.4.

The beam position is adjusted by means of several fluorescence screens, which, however, can only be used at very low beam currents. Therefore, during the experiment, the beam current is monitored online by continuously integrating the current on the radiator while a detector array of 5 Si-PIN diodes mounted behind the collimator allows for a coarse control of photon-flux intensity and beam position.

To study photodisintegration reactions, targets can be irradiated at two different positions. The first position is located directly behind the radiator, where one obtains a high-intense photon flux. The distance between radiator and target at this position was about 6.5 cm in older experi-

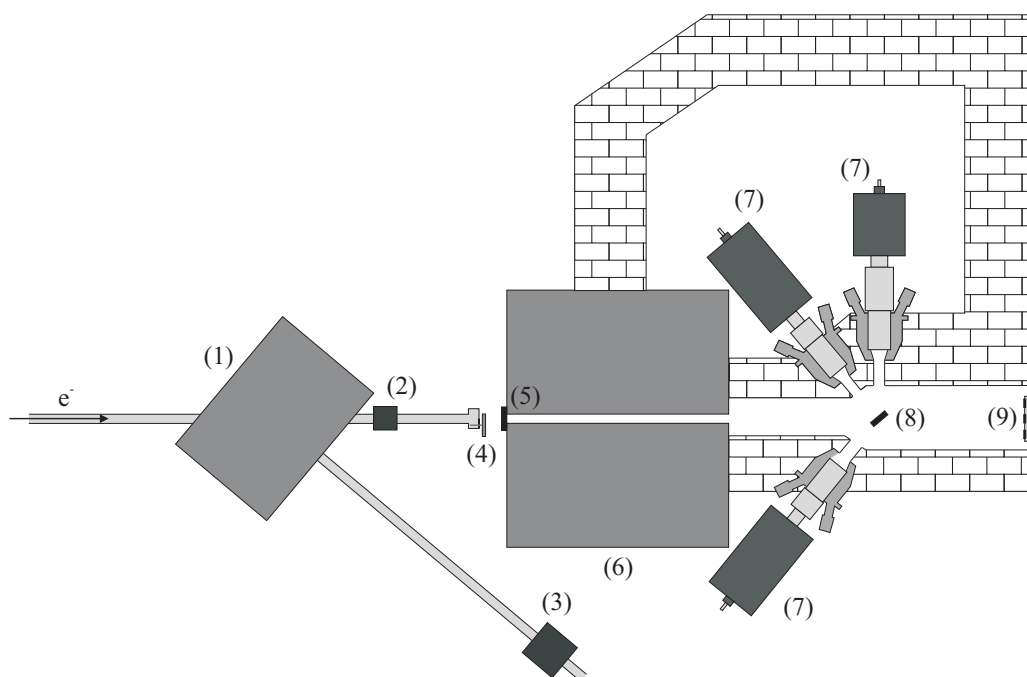


Fig. 3.2: Schematic layout of the photoactivation setup. The energy of the monoenergetic electron beam is adjusted with a well-calibrated 40° deflecting magnet (1), and the beam position is monitored on fluorescence screens (2,3). The beam is then stopped in a massive copper radiator (4) producing intense bremsstrahlung. The photons are used for the irradiation of targets, which can be mounted in front of (5) and behind (8) a thick copper collimator system (6). In addition, at position (8) photon-scattering reactions can be studied with actively-shielded HPGe detectors (7). A detector array of Si-PIN diodes (9) monitors the beam intensity and position during the irradiation.

ments and since 2007 has been increased to a larger distance of 19 cm due to small modifications on the beam line and radiator. The second target position is located behind a thick copper collimator system at a distance of 165 cm to the radiator (respectively, 177.5 cm since 2007). The well-collimated photon beam at this position provides a sufficiently low background condition to study photon-scattering reactions with actively-shielded high-purity germanium (HPGe) detectors [45]. However, the photon-flux intensity behind the collimator is approximately 270 times lower than in front of the collimator as shown in Fig. 3.3. A much longer irradiation at the second target position is needed for a sufficient reaction yield and, therefore, the first target position is definitely preferable. Nevertheless, some previous photoactivation experiments had to be performed behind the collimator [46–48] because no reliable description of the spectral shape of the photon flux in front of the collimator was available at that time. This will be discussed in more detail in Sec. 3.3.

For the determination of the time-integrated photon flux during the irradiation, the reaction yields of various standard reactions of well-known cross sections are measured simultaneously

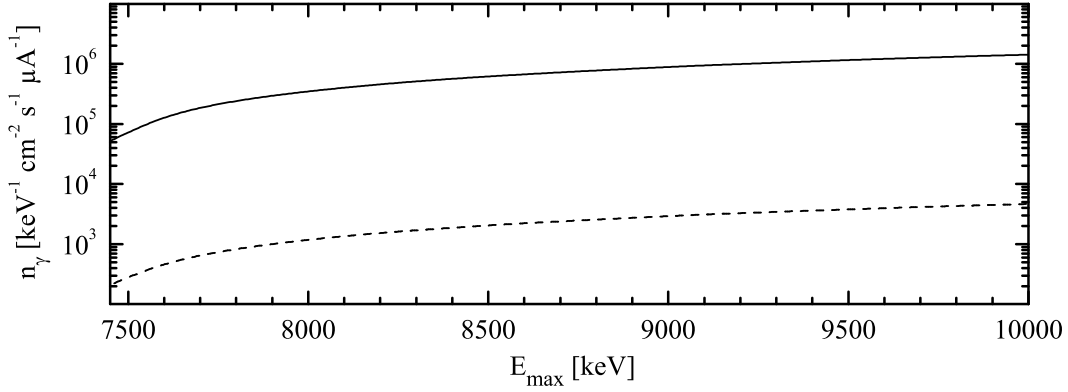


Fig. 3.3: Absolute photon flux n_γ for a fixed photon energy of $E_\gamma = 7332$ keV as a function of maximum photon energy E_{\max} at the photoactivation setup prior to the year 2007. The photon-flux intensity sharply increases with E_{\max} (note the logarithmic scale) and is approximately 270 times lower behind the collimator (dashed line) than in front of the collimator (solid line). The absolute values have changed since 2007 due to small modifications on the beam line and radiator. See text for more details.

in each experiment. Conventionally, this is done by observing the photon-scattering reaction $^{11}\text{B}(\gamma, \gamma')$ at the second target position or by measuring the photodisintegration reactions $^{187}\text{Re}(\gamma, n)$ and $^{197}\text{Au}(\gamma, n)$ at both target positions, respectively. A detailed discussion of the photon-flux determination is given in Sec. 3.3.

The photodisintegration reaction yield Y , i. e., the number of reaction products induced by a certain photodisintegration reaction during an irradiation using bremsstrahlung of energy E_{\max} , is given by:

$$Y^{E_{\max}} = N_T \int N_\gamma(E, E_{\max}) \sigma(E) dE = N_T I_\sigma, \quad (3.1)$$

where N_T denotes the number of target nuclei, $N_\gamma(E, E_{\max})$ is the time-integrated photon flux $\int_0^{t_{\text{act}}} n_\gamma(E, E_{\max}, t) dt$ for the duration of activation t_{act} , and $\sigma(E)$ is the energy-dependent photodisintegration cross section. In the following, the integral of Eq. (3.1) will be referred to as the *energy-integrated cross section* I_σ .

The reaction yield Y is determined after the irradiation by measuring the γ transitions following the α or β decays of the produced unstable isotopes with HPGe detectors under low-background conditions. Hence, photoactivation experiments are usually restricted to the investigation of those reactions where the reaction product is unstable and has an appropriate half-life and γ intensity of the decay to be observable. The excellent energy resolution of HPGe detectors of the order of 1 keV for photon energies of about 100 keV assures a distinct identification of the observed γ transitions and, therefore, a clear assignment to the corresponding decay, even if many γ transitions appear in the decay spectrum. This allows to study simultaneously a variety

of target isotopes and to use naturally composed targets in the experiment. Therefore, photoactivation experiments are a time-efficient as well as a cost-efficient technique. The determination of the reaction yield is discussed in detail in Sec. 3.2.

Finally, the energy-integrated cross section I_σ from Eq. (3.1) can be derived from the reaction yield and compared with theoretical model calculations. In the following, two different methods of data analysis are discussed.

3.1.1 Normalization of absolute cross-section predictions

Although the experiment directly yields the energy-integrated cross section I_σ according to Eq. (3.1), a further deduction of the absolute cross section σ can hardly be performed. This is due to the fact that bremsstrahlung is characterized by a continuous spectral distribution making a deconvolution of I_σ generally impossible. However, if a theoretical prediction for the cross section denoted by σ^{Theory} is adopted, I_σ can be theoretically calculated and then directly compared with the experiment. This yields a normalization factor f for the prediction:

$$f^{E_{\max}} = \frac{I_\sigma^{\text{Exp}}}{I_\sigma^{\text{Theory}}} = \frac{I_\sigma^{\text{Exp}}}{\int N_\gamma(E, E_{\max}) \sigma^{\text{Theory}}(E) dE} . \quad (3.2)$$

By using bremsstrahlung of different energies E_{\max} and deriving f for each energy, one can test the validity of a theoretical prediction within different regions of energy. If the cross section is accurately described by theory, f should be independent of E_{\max} and close to unity. However, one should point out that photoactivation experiments using bremsstrahlung only have limited sensitivity to the shape of the cross section because the normalization factor f indicates an average over a wide energy range as illustrated in Fig. 3.4. If the aim is to derive information about the energy dependence from the subtraction of reaction yields obtained at different E_{\max} , then this analysis is strongly hampered by the large uncertainties associated with the subtraction of nearly equally large numbers.

Anyway, measuring at different energies E_{\max} will reduce several experimental uncertainties and increase the reliability of the derived normalization factor. Therefore, in this thesis a mean normalization factor $\langle f \rangle$ is usually derived from averaging over measurements at different energies E_{\max} .

3.1.2 Determination of ground-state reaction rates

The physical values directly involved in astrophysical network calculations are reaction rates rather than cross sections. In particular, for calculations of the p -process network, mainly photodisintegration reaction rates for isotopes in a hot thermal photon bath need to be adopted. According to Sec. 2.2, these rates are determined by:

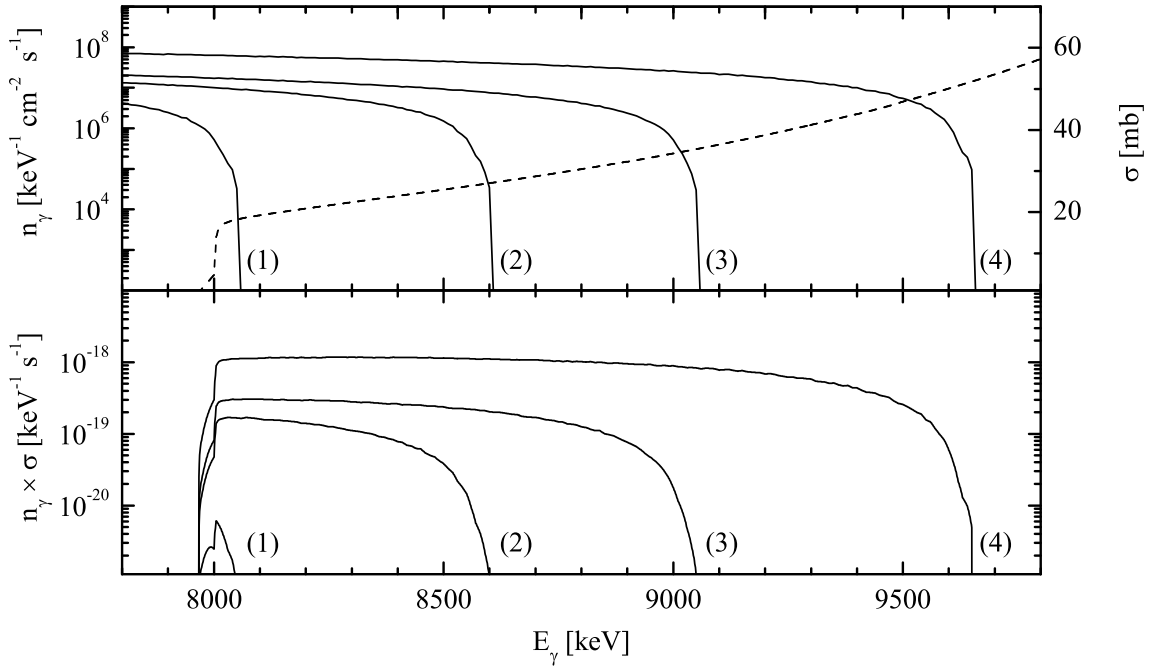


Fig. 3.4: *Top panel:* Simulated spectral distribution of bremsstrahlung at different energies E_{\max} of (1) 8050 keV, (2) 8600 keV, (3) 9050 keV, and (4) 9650 keV (solid lines) in comparison to the photoneutron cross section σ of ^{154}Sm (dashed line) predicted by the NON-SMOKER^{WEB} code [27]. *Bottom panel:* The product $n_\gamma \times \sigma$ yields the integrand of the energy-integrated cross section I_σ (see Eq. (3.1)), which covers a broad energy range close to the neutron separation energy.

$$\lambda^*(T) = c \int n_\gamma^{\text{Planck}}(E, T) \sigma^*(E) dE \quad , \quad (3.3)$$

where n_γ^{Planck} is the Planck distribution of Eq. (2.1), σ^* denotes the stellar photodisintegration cross section of Eq. (2.3), and c is the velocity of light. As discussed in detail in Sec. 2.2, stellar reaction rates cannot be measured directly in the laboratory because it is not possible to produce a thermal photon bath at p -process conditions, i. e., with the intensities resulting from temperatures between 2 and 3×10^9 K, and, thus, to account for the thermal population of excited states. Therefore, only ground-state reaction rates denoted by $\lambda^{\text{g.s.}}$ can be determined in the experiment.

An obvious way of deriving $\lambda^{\text{g.s.}}$ is to use the normalized cross section $\sigma = \langle f \rangle \times \sigma^{\text{Theory}}$ of the analysis described in the preceding section and then to calculate the ground-state reaction rate from Eq. (3.3). Using this method one has to rely on an appropriate description of the energy dependence of the cross section. This might lead to large systematic uncertainties if the

predicted shape of the cross section deviates significantly from its real shape, e. g., if some resonances above the neutron emission threshold are omitted in the theoretical description. Hence, an approach is preferred where the reaction rates can be directly determined from experimental data without the need of any theoretical input. This can be achieved by approximating the Planck spectrum at temperature T with a superposition of several bremsstrahlung spectra $n_{\gamma}^{\text{Brems}}(E, E_{\text{max}}^i)$ at different energies E_{max}^i [49]:

$$cn_{\gamma}^{\text{Planck}}(E, T) \approx \sum_i a_i(T) N_{\gamma}^{\text{Brems}}(E, E_{\text{max}}^i) \quad , \quad (3.4)$$

where $a_i(T)$ are temperature-dependent weighting coefficients. As illustrated in Fig. 3.5, a highly accurate approximation of the Planck spectrum can be achieved in the relevant energy region for astrophysical studies just above the neutron threshold energy, i. e., in the Gamow-like window, depending on how many bremsstrahlung spectra are used for the approximation. In general, using only about five bremsstrahlung spectra, the deviation between approximated and real Planck spectrum in the astrophysically relevant energy region is already less than 10%. With this approximation, Eq. (3.3) can be written as:

$$\lambda^{\text{g.s.}}(T) \approx \sum_i a_i(T) \int N_{\gamma}^{\text{Brems}}(E, E_{\text{max}}^i) \sigma(E) dE \quad (3.5)$$

$$= \sum_i a_i(T) I_{\sigma, i}^{\text{Exp}} \quad . \quad (3.6)$$

Since the energy-integrated cross section $I_{\sigma, i}^{\text{Exp}}$ is directly determined by the experiment, the reaction rates can be obtained without further assumptions on the energy dependence of the cross

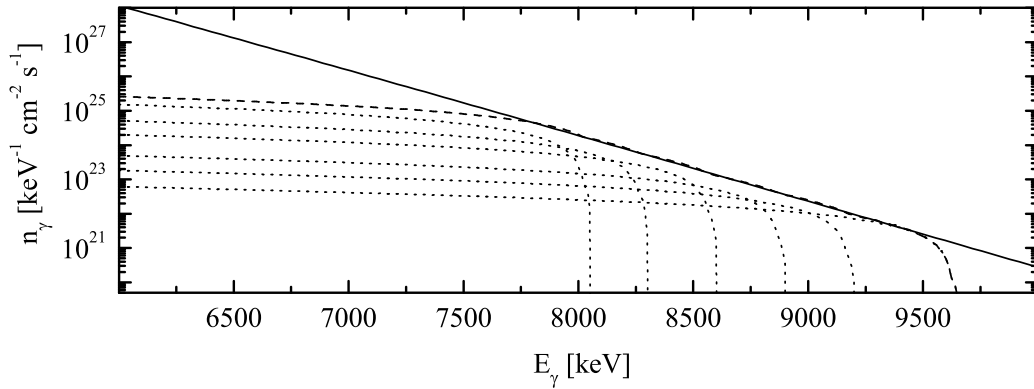


Fig. 3.5: Thermal Planck spectrum at a temperature of $T = 2.5 \times 10^9$ K (solid line). The weighted sum of different bremsstrahlung spectra (dotted lines) yields a good approximation (dashed line) of the Planck spectrum within a small energy window. See text for details.

section. Therefore, this analysis is free of systematic uncertainties stemming from any cross section prediction. Nevertheless, a reliable description of the spectral shape of bremsstrahlung close to E_{max} is essential. This will be discussed in detail in Sec. 3.3.

The experimentally determined ground-state reaction rates can then be compared to theoretical predictions. The ratio of experimental and theoretical rates can slightly differ from the normalization factor $\langle f \rangle$ of the preceding section because $\langle f \rangle$ is determined by a weighted average with regard to the uncertainties of each data point, whereas $\lambda^{\text{g.s.}}$ is derived from a weighted sum using additionally appropriate weighting coefficients $a_i(T)$. Contrary, these coefficients usually enhance the contribution of data points with larger uncertainties measured at energies very close to the threshold.

3.2 Determination of reaction yields

To determine the reaction yield of a certain reaction in photoactivation experiments, the γ transitions subsequent to the α or β decays of the produced unstable isotopes are measured with HPGe detectors after the irradiation. A typical decay spectrum is shown in Fig. 3.6.

The reaction yield Y can be derived from the activity of the irradiated target:

$$Y = \frac{A_0}{\lambda} \times \tau_{\text{act}} \times \tau_{\text{lost}} \quad , \quad (3.7)$$

where A_0 denotes the activity at the beginning of the measurement, λ is the decay constant, and τ_{act} and τ_{lost} are time-dependent correction terms.

To determine the activity A_0 , the decay spectrum is accumulated over a time period t_{meas} , which yields a peak at energy E and of area N_{meas} in the spectrum corresponding to a certain γ transition. The activity can then be calculated using:

$$A_0 = \frac{N_{\text{meas}} \times \lambda}{I_\gamma \times \varepsilon \times (1 - e^{-\lambda t_{\text{meas}}}) \times \tau_{\text{dead}}} \quad , \quad (3.8)$$

where I_γ is the intensity of the observed γ transition per decay of the parent nucleus, ε denotes the energy-dependent detection efficiency, and τ_{dead} is the correction for the dead time of the data acquisition system.

The correction factors τ_{act} and τ_{lost} account for the decay of produced nuclei during and after the irradiation, respectively. The latter is simply described by the decay law:

$$\tau_{\text{lost}} = e^{\lambda t_{\text{lost}}} \quad , \quad (3.9)$$

where t_{lost} denotes the time period between the end of irradiation and the beginning of measuring the decay. For the correction factor τ_{act} , one needs to take into account that the reaction products

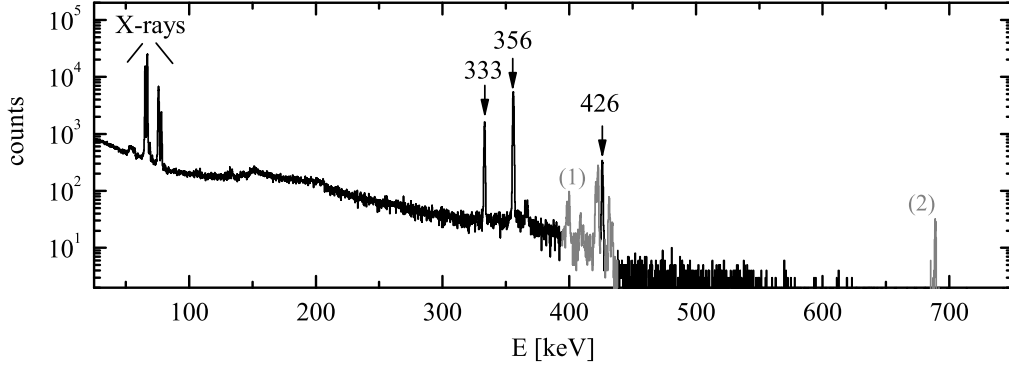


Fig. 3.6: Typical spectrum of an irradiated gold target measured at the LEPS setup (see Sec. 3.2.1). The spectrum was accumulated over a period of about 13 min. The strong γ transitions of energy $E_\gamma = 333.03$ keV, 355.73 keV, and 426.10 keV can clearly be identified in the spectrum. The gray-colored peaks stem from coincidences between X-rays and either of the transitions of energy $E_\gamma = 333.03$ keV and 355.73 keV (1) and coincidences between these two transitions (2), respectively.

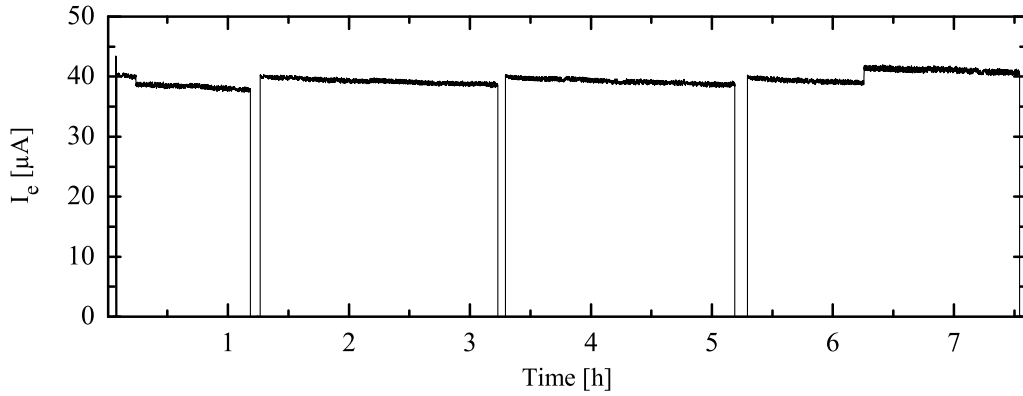


Fig. 3.7: Beam-current record of an experimental run at $E_0 = 9050$ keV. The beam current has been averaged over a time interval of $\Delta t \approx 2 - 3$ s. The irradiation was periodically interrupted to check the beam energy.

are continuously, but – due to fluctuations in the photon flux – usually not homogeneously accumulated in time during the period of irradiation t_{act} . Since the number of nuclei $N_{\text{prod},i}$ produced in a time interval Δt_i is directly proportional to the photon flux and, thus, to the beam current I_e on the radiator, τ_{act} can be derived from the time profile of the beam-current record (see Fig. 3.7):

$$\tau_{\text{act}} = \frac{\sum_i N_{\text{prod},i} \cdot e^{-\lambda(t_{\text{act}} - t_i)} \Delta t_i}{\sum_i N_{\text{prod},i}} = \frac{\sum_i I_{e,i} \cdot e^{-\lambda(t_{\text{act}} - t_i)} \Delta t_i}{\sum_i I_{e,i}} . \quad (3.10)$$

Usually, the fluctuations only have a minor impact on the correction factor τ_{act} , and the beam current can be assumed to be constant. The corrections due to fluctuations become only significant if the half-life of the reaction product is much shorter than the duration of irradiation.

3.2.1 Detector setups

For the experiments of this thesis two different setups have been used to measure the reaction yields of a photoactivation experiment.

The first setup consisted of a coaxial HPGe detector with 30% efficiency relative to a $3'' \times 3''$ NaI detector and will be referred to as *HPGe setup* in the following. The distance between target and detector was varied in different experiments. Small distances were used to cover a large solid angle to assure a high detection efficiency. On the other hand, larger distances

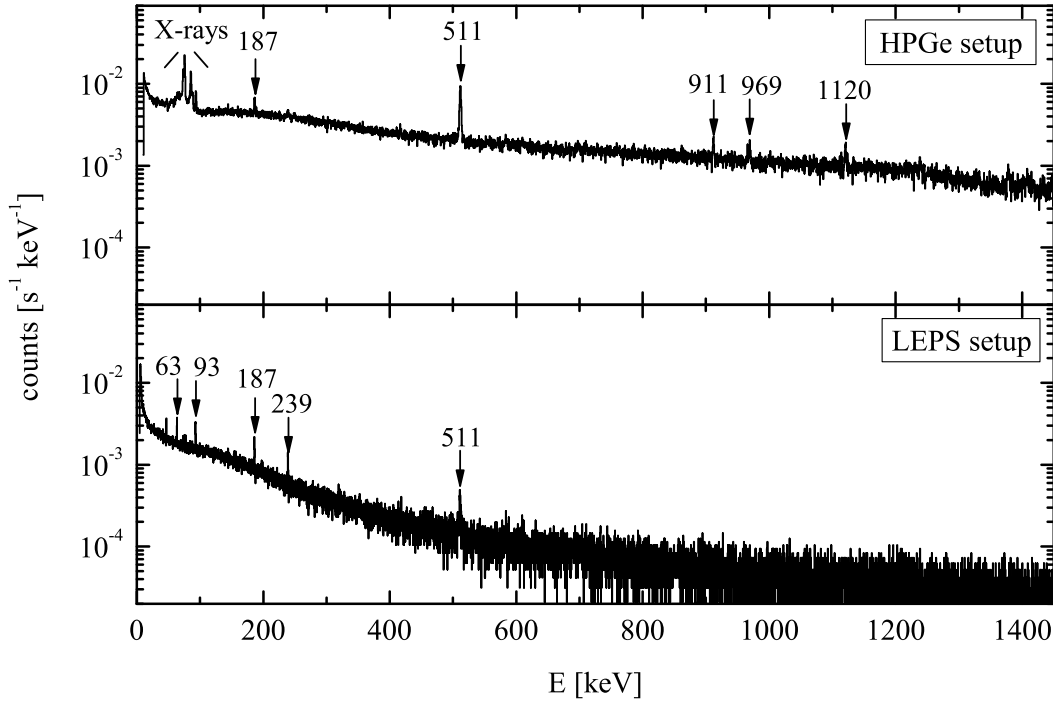


Fig. 3.8: Natural background spectrum measured at the HPGe and LEPS setup. The spectra have been accumulated for a period of a few days and were normalized to the measuring time afterwards. In comparison with the HPGe setup, the background rate sharply decreases towards higher energies at the LEPS setup. This can be understood with regard to the sharply decreasing detection efficiency for photons of higher energy due to the relatively small detector crystal (see Fig. 3.9). Moreover, the peaks stemming from the X-rays of lead are significantly suppressed at the LEPS setup due to an additional copper shielding. Some prominent peaks stemming from natural background are indicated by arrows (energies in units of keV).

were applied to minimize summing effects of coincident γ rays in the spectra. The treatment of summing effects is described in detail in Sec. 3.2.4.

Additionally, a second setup was used in the described experiments which consisted of two planar HPGe *Low-Energy Photon Spectrometers* (LEPS) of almost identical construction and will be denoted by *LEPS setup* in the following. These detectors suffer from a relatively small detector crystal when being used for the detection of photons of energies above a few hundred keV. However, they provide an excellent energy resolution of less than 1 keV for photon energies of about 100 keV. Furthermore, they benefit from a very thin beryllium entrance window making them highly sensitive even to low-energetic photons down to a few keV. These detectors were positioned face-to-face having a distance of only 10 mm to each other. The targets were mounted directly between the two detectors to obtain a high detection efficiency. However, this geometry gave rise to a significant amount of summing effects, which had to be corrected by a careful analysis.

Both setups were covered by thick shieldings of lead to reduce natural background. In addition, the LEPS were shielded by an inner layer of copper to reduce X-rays and low-energy γ rays stemming from the outer lead shielding. The natural background spectrum measured at both setups is shown in Fig. 3.8.

3.2.2 Detection efficiency

The detection efficiency of each detector setup was simulated using the Monte Carlo code GEANT4 [43]. For this purpose, the full geometry of the detectors was implemented into the simulation code with regard to the detailed dimensions including any absorbing layers, e. g., entrance window and dead layers of the detector crystal (see Tab. B.2 of the appendix). In addition to the simulations, efficiencies at certain energies between 14 and 1350 keV were measured using standard calibration sources, which served as a normalization for the simulated efficiency curve. A list of sources used for the experiments of this thesis is shown in Tab. B.1 of the appendix. If not otherwise stated, the efficiency will always refer to the *photopeak efficiency* in the following, i. e., the probability that a photon deposits its full energy in the detector.

As shown in Fig. 3.9, the normalized simulations are in good agreement with the experimental data points and provide a reliable description of the energy-dependent detection efficiency. From the experimental uncertainties and the deviation between experimental data points and normalized simulations, it was estimated that the absolute detection efficiency can be determined with an uncertainty of less than 7% for energies of up to about 1500 keV at each detector setup.

In some of the experiments of this thesis, two independent measurements of the detection efficiency were performed at the beginning and at the end of the beam time, respectively, to confirm the reproducibility of the efficiency calibration. It has been found that the detection efficiency can be accurately reproduced within an uncertainty of about 2% for those setups using a large

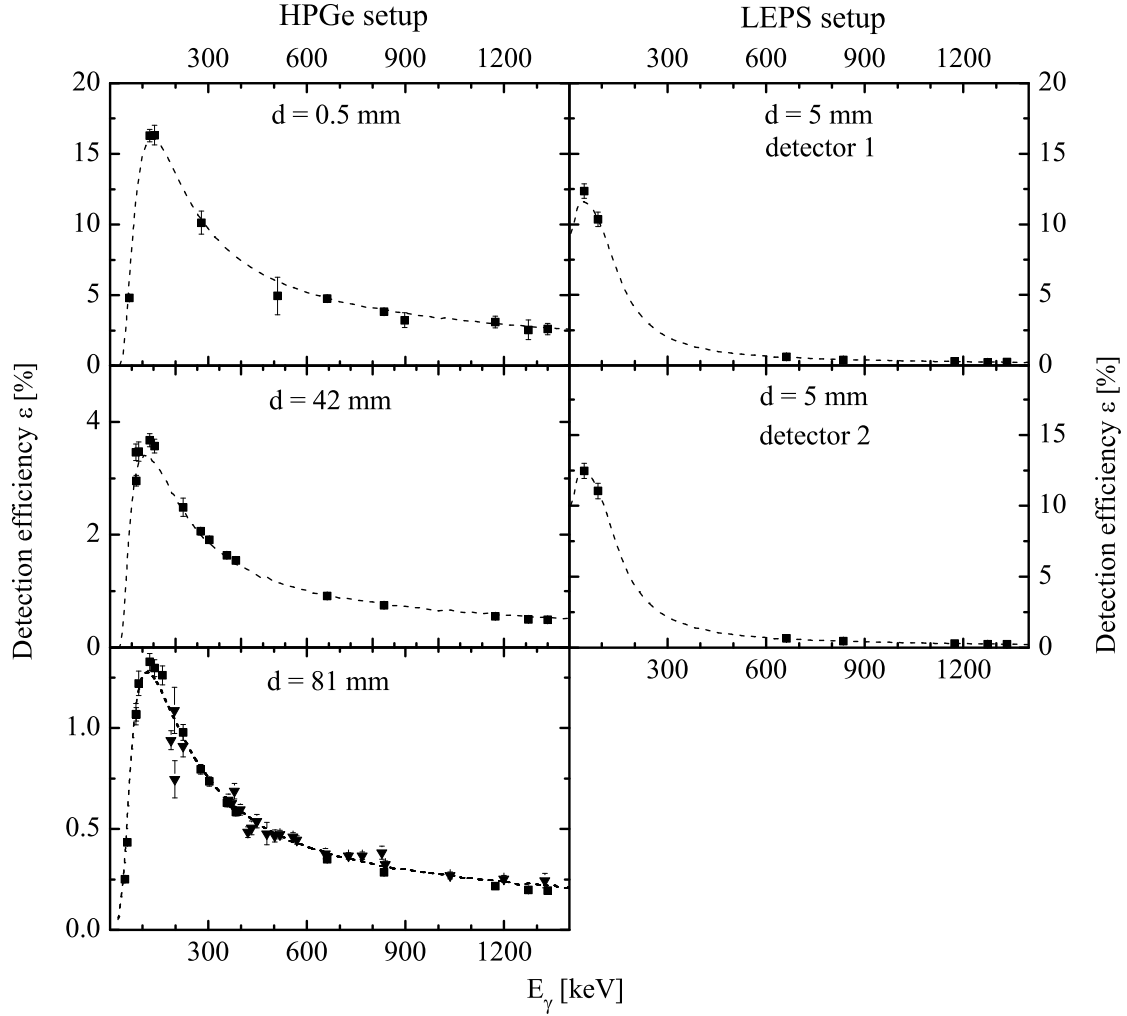


Fig. 3.9: Detection efficiency of the HPGe and LEPS setup. Calibration sources (squares) served as a normalization for simulations of the detection efficiency (dashed line). Due to large summing effects of coincident photons at small distances between detector and source (see Sec. 3.2.4), only those calibration sources without γ cascades were used in these cases. In addition, non-calibrated radioactive sources (triangles) have been used to further confirm the energy dependence of the detection efficiency. *Left panels:* Detection efficiency at the HPGe setup for various distances between detector and source denoted by d . *Right panels:* Detection efficiency of the two different detectors used at the LEPS setup. The distance between the detectors and sources was 5 mm. Both detectors are almost of identical construction so that they nearly provide the same detection efficiency.

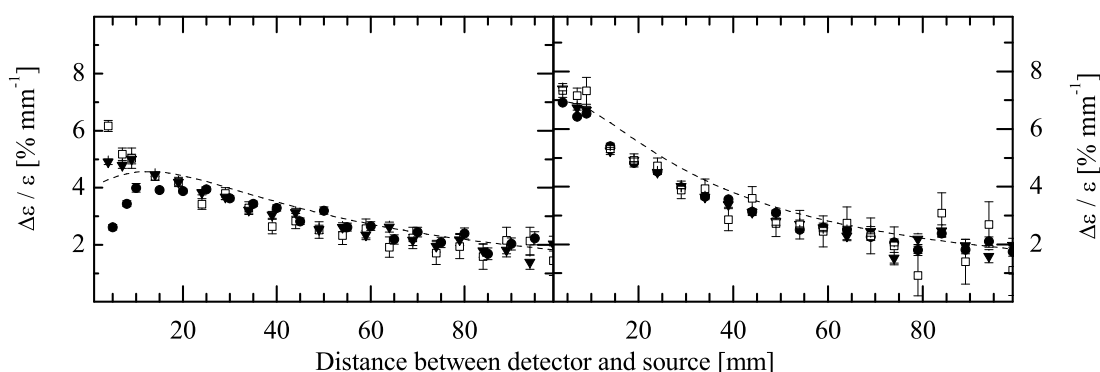


Fig. 3.10: The variation of detection efficiency as a function of distance between source and detector has been simulated for both the HPGe setup and LEPS setup. The plot shows the uncertainty of the detection efficiency assuming a 1 mm uncertainty of distance between detector and source for photon energies of 100 keV (circles), 200 keV (triangles) and 1000 keV (open squares). A calculation based on the geometrical efficiency only is shown as a dashed line. See text for details.

distance between detector and calibration source. However, setups using very small distances showed deviations of about 10% in several measurements.

It has been assumed that these deviations stem from uncertainties of the positioning of the sources in front of the detectors. To confirm this assumption, the sensitivity of the detection efficiency as a function of distance between detector and source has been investigated in simulations. The results are illustrated in Fig. 3.10. The simulations confirm the sensitivity expected for the *geometrical efficiency*, which only refers to the solid angle covered by the detector. Deviations can be understood with regard to the fact that the *intrinsic efficiency*, i. e., the probability for a full energy deposition of a photon hitting the detector, is also a function of distance.

One finds that at the HPGe setup a variation of 1 mm in distance causes a relative uncertainty of the detection efficiency of about 5%, if the source is placed very close to the detector. As expected, the sensitivity decreases towards larger distances giving rise to uncertainties of about 2% per mm variation for a distance of 100 mm.

At the LEPS setup, the sensitivity is found to be slightly higher up to about 8% per mm variation, presumably due to the smaller diameter of the detector crystal. It was found that the results are almost independent of photon energy. Therefore, if one assumes a reasonable uncertainty in the positioning of the sources of about 1 mm the discrepancies found in the measurements can be understood with regard to these results.

3.2.3 Correction for self-absorption and target dimensions

The previous section described how the detection efficiency for photons emitted by point-like sources can be determined. In the experiments of this thesis, however, targets of finite dimensions are used, typically disks with a diameter of 20 mm. Therefore, the efficiencies derived from point-like sources need to be adjusted appropriately to be adopted for the data analysis of photoactivation experiments.

For this purpose, three different effects must be taken into consideration. First, one has to account for self-absorption of photons within the targets. This is especially of importance if low-energetic photons should be observed. Secondly, photons are emitted from any position within the finite target volume. Hence, the assumption of a point-like source is not satisfied. And thirdly, the activity of an irradiated target is not spread homogeneously over the target volume due to the angular distribution of bremsstrahlung used for the irradiation.

To account for these effects, detailed simulations using GEANT4 were performed. The detection efficiency for photons of energy E of a voluminous target can be calculated from:

$$\varepsilon_{\text{Target}}(E) = \varepsilon_{\text{Point}}(E) \times \frac{\varepsilon_{\text{Target}}^{\text{Sim}}(E)}{\varepsilon_{\text{Point}}^{\text{Sim}}(E)}, \quad (3.11)$$

where $\varepsilon_{\text{Point}}$ denotes the experimental detection efficiency for a point-like source as derived in the previous section while $\varepsilon_{\text{Target}}^{\text{Sim}}$ and $\varepsilon_{\text{Point}}^{\text{Sim}}$ refer to the simulated detection efficiency for a target of finite dimensions and a point-like source, respectively. The ratio of $\varepsilon_{\text{Target}}^{\text{Sim}}$ and $\varepsilon_{\text{Point}}^{\text{Sim}}$ states the correction which needs to be applied to the experimentally determined efficiency curve.

It is possible to determine this correction by means of one single comprehensive simulation that takes into consideration all of the effects mentioned above. However, to study each effect separately, $\varepsilon_{\text{Target}}^{\text{Sim}}$ can be written as:

$$\varepsilon_{\text{Target}}^{\text{Sim}}(E) = \frac{\int_0^\Delta \int_0^R \varepsilon^{\text{Sim}}(E, \rho, z) P(\rho) d\rho dz}{\int_0^\Delta \int_0^R P(\rho) d\rho dz}, \quad (3.12)$$

where R and Δ are target radius and thickness, respectively, and ρ and z denote the cylindrical coordinates. ε^{Sim} is the simulated detection efficiency including self-absorption for a photon emitted at the position (ρ, z) , and P denotes the activity distribution of the target as a function of ρ .

The efficiency function ε^{Sim} has been determined for targets of different material and mass. The activity distribution P has been adopted from the angular distribution of the photon flux used for the irradiation, which has been derived from bremsstrahlung simulations (see Sec. 3.3.1) and is illustrated in Fig. 3.11.

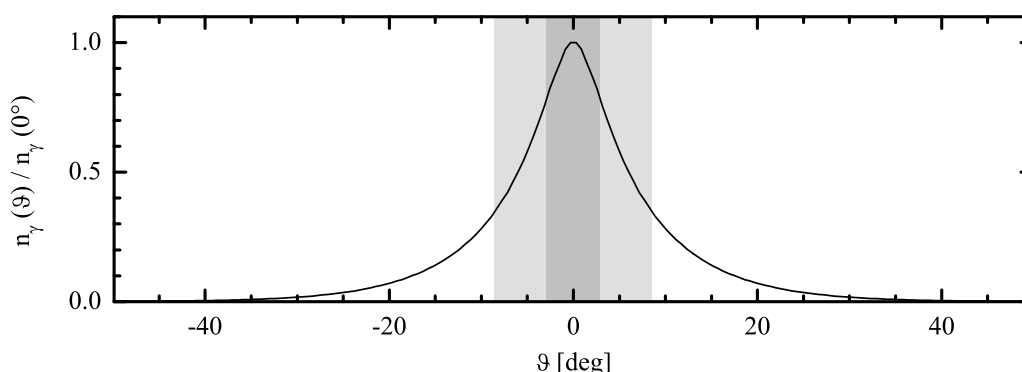


Fig. 3.11: Angular distribution of bremsstrahlung at the photoactivation setup. The graph shows the simulated photon flux n_γ for a maximum photon energy of $E_{\max} = 9500$ keV as a function of ϑ which denotes the angle between beam axis and momentum vector of the bremsstrahlung photon. The distribution has been normalized to $n_\gamma(0^\circ)$. The gray areas indicate the angular regions covered by targets in front of the collimator before (light gray) and after modifications of the setup (dark gray), respectively. The angular region covered by targets behind the collimator is very small. Thus, targets behind the collimator are irradiated almost homogeneously over the target volume.

Extensive simulations have shown that the contribution due to the finite dimensions of the target sensitively depends on the geometry of the detector setup. A correction of about 1% for the HPGe setup using a distance of 81 mm between target and detector and of about 7% for the LEPS setup using a distance of 5 mm has been determined, respectively. In addition, a significant contribution was found to stem from self-absorption of photons within the target depending on target mass and material. Finally, the detection efficiency has been calculated using both a homogeneous activity distribution and a distribution according to the angular distribution of Fig. 3.11. Interestingly enough, the results determined for the two different activity distributions only showed deviations of the order of 1% indicating that the averaged detection efficiency is rather insensitive to the adopted activity distribution.

A selection of correction factors is shown in Tab. C.1 of the appendix. With regard to the uncertainties of the simulations, it was estimated that the correction factors can be determined with an overall uncertainty of less than 5%.

3.2.4 Treatment of summing effects

Whenever a detector is coincidentally hit by two photons, the detector response will appear to stem from only one single event with signal strength corresponding to the summed energy deposition of both photons. In general, two events can be ascribed to be coincident if they occur within a short time interval compared to the time constant of the data acquisition system.

For a setup using HPGe detectors with conventional electronics, the time constant is usually of the order of a few μs . Thus, if the detection rate is restricted to a maximum rate of a few kHz, as this was the case for the experiments of this thesis, random coincidences will only play a minor role. However, a significant amount of coincident events will occur if a decay is measured in which the nucleus de-excites from an excited level by the subsequent emission of several photons (see Fig. 3.12). The time constant of these transitions is usually of the order of 1 ps and, therefore, much shorter than the time constant of the data acquisition system.

In the following, it will be described how coincident events distort a measured spectrum due to summing effects and how this can be corrected in the data analysis. These corrections have already been discussed in previous works, e. g., see Ref. [41]. However, summing effects have played a major role for several decays studied in the experiments of this thesis, and, therefore, it is worthwhile to recapitulate the correction procedure. Moreover, it was found that some of the corrections derived in previous works have to be revised for reasons discussed further below.

To point out the contributions of summing effects, a typical photoactivation experiment will be discussed in which the reaction products decay according to Fig. 3.12, and the activity of the irradiated target has to be determined. For this purpose, one could, e. g., count the number of transitions γ_5 via the detection of the corresponding photons, which yield a peak at energy E_5 and of area N_5 in the observed spectrum (notations are according to Fig. 3.12).

Neglecting any summing effects, the target activity A_0 can be determined according to Eq. (3.8):

$$N_5 = \frac{A_0}{\lambda} \times (1 - e^{-\lambda t}) \times \tau_{\text{dead}} \times I_5^{\gamma+\text{ce}} \times \frac{1}{1 + \alpha_5} \times \varepsilon_5 \quad , \quad (3.13)$$

In the following, $I_i^{\gamma+\text{ce}}$ denotes the probability for the transition γ_i per decay of the parent nucleus due to the emission of either a photon or a conversion electron, α_i is the conversion coefficient, and ε_i is the photopeak efficiency.

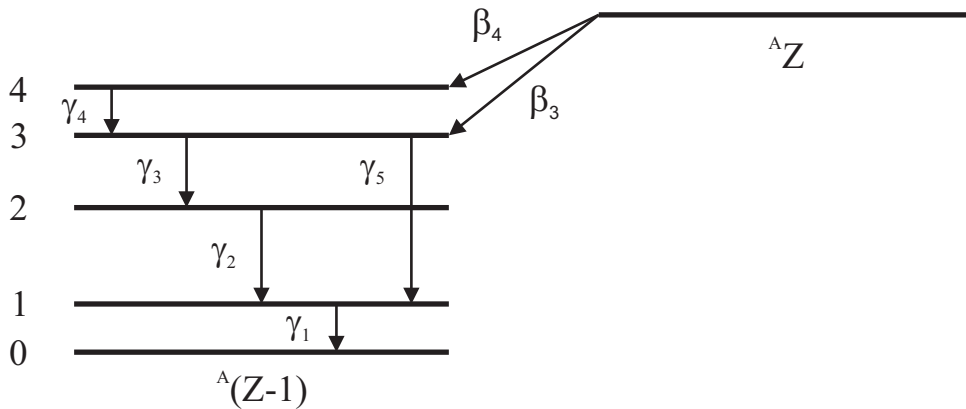


Fig. 3.12: Typical β -decay scheme. Several levels in the daughter nucleus $^A(Z-1)$ can be populated by the β decay and will de-excite by means of various transitions γ_i .

However, due to summing effects the observed spectrum is usually distorted and the observed peak area N_{meas} at energy E_5 will deviate from N_5 . For example, the observed peak area will be reduced compared to N_5 if photons stemming either from γ_1 or γ_4 are measured in coincidence with photons stemming from γ_5 because these events will have a total energy deposition larger than E_5 . On the other hand, the peak area will be increased if photons stemming from γ_2 are measured in coincidence with photons stemming from γ_3 and both photons deposit their full energy in the detector. Thus, N_{meas} is given by:

$$N_{\text{meas}} = N_5 - N_{1+5} - N_{4+5} + N_{2+3} \quad , \quad (3.14)$$

where N_{i+j} refers to events stemming from the coincidence of γ_i and γ_j . To determine N_5 , it is mandatory to calculate the contributions of the terms corresponding to summing effects. This will be briefly described in the following.

With regard to the notation used above, N_{1+5} can be calculated by:

$$N_{1+5} = N_5 \times \frac{1}{1 + \alpha_1} \times \underbrace{\varepsilon_1 \frac{\varepsilon_1^{\text{total}}}{\varepsilon_1}}_{(i)} \quad , \quad (3.15)$$

Term (i) quotes the probability of a photon of energy E_1 to deposit any amount of energy in the detector. It is important to point out that photons need not necessarily deposit their full energy to give contributions to N_{1+5} because any additional energy deposition will shift an event of true energy E_5 to higher energies in the observed spectrum. To calculate term (i), one can adjust the well-known photopeak efficiency by a correction factor $\varepsilon_i/\varepsilon_i^{\text{total}}$, which will be referred to as the *photopeak-to-total ratio* in the following. This ratio has been determined by means of simulations illustrated in Fig. 3.13. Some larger discrepancies can be observed between simulations and experimental data indicating a rather large uncertainty for the adopted photopeak-to-total ratio. However, the contribution of this uncertainty to the overall experimental uncertainty is usually rather small (see Sec. 3.5).

As shown in Fig. 3.13, the photopeak-to-total ratio becomes significant for the correction procedure of summing effects for photon energies $E_\gamma > 100$ keV. Nevertheless, this ratio was not taken into account in previous works (e. g., see Ref. [41]). Therefore, some of the previous experimental results have to be revised, especially if the studied decays gave rise to strong summing effects. Such a revision has been performed for the photoneutron reaction of ^{197}Au in Sec. 3.3.2.

In analogy to the calculation of N_{1+5} , N_{4+5} is given by:

$$N_{4+5} = N_5 \times \frac{I_4^{\gamma+\text{ce}}}{I_4^{\gamma+\text{ce}} + I_3^\beta} \times \frac{1}{1 + \alpha_4} \times \varepsilon_4 \frac{\varepsilon_4^{\text{total}}}{\varepsilon_4} \quad , \quad (3.16)$$

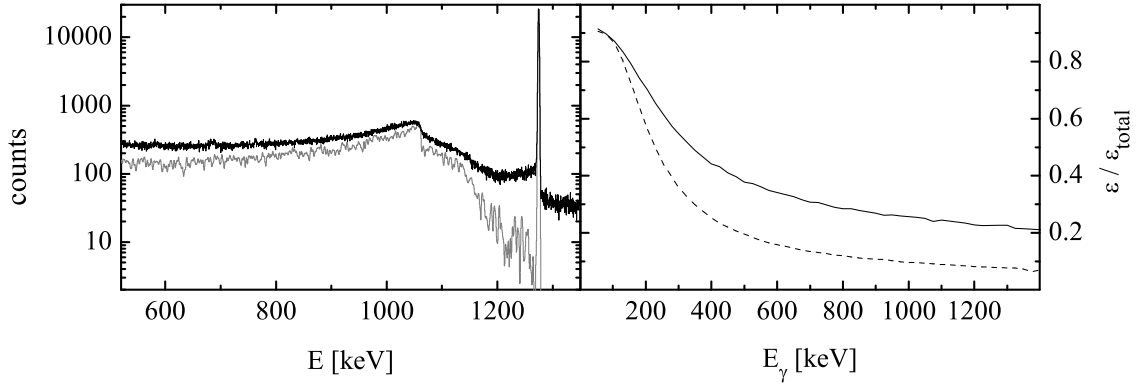


Fig. 3.13: *Left panel:* The decay spectrum of a ^{22}Na source measured with a HPGe detector (black histogram) is compared with a simulation using GEANT4 (gray histogram). The simulated spectrum was folded with a Gaussian function to account for the energy resolution of the detector. Both spectra have been normalized to give the same photopeak area. A large amount of photons do not deposit their full energy in the detector. The ratio of photopeak events to the total number of events in the spectrum is denoted by the *photopeak-to-total ratio* $\varepsilon/\varepsilon_{\text{total}}$. The simulation overestimates the photopeak-to-total ratio by about 30-40%, although the shape of the spectrum is fairly described. *Right panel:* The graph shows results of a simulation for the photopeak-to-total ratio as a function of photon energy for the HPGe setup (solid line) and the LEPS setup (dashed line), respectively. The results were found to be almost independent of the adopted distance between detector and source.

where I_3^β denotes the probability for the population of state 3 due to the β decay of the parent nucleus.

Furthermore, N_{2+3} is determined by:

$$N_{2+3} = \frac{A_0}{\lambda} \times (1 - e^{-\lambda t}) \times \tau_{\text{dead}} \times I_3^{\gamma+\text{ce}} \times \frac{1}{1 + \alpha_3} \times \varepsilon_3 \times \frac{1}{1 + \alpha_2} \times \varepsilon_2 \quad , \quad (3.17)$$

Note that no photopeak-to-total ratio appears in Eq. (3.17) because both photons stemming from γ_2 and γ_3 have to deposit their full energy to yield an event of total energy E_5 .

Using Eq. (3.14) to (3.17), N_5 can be directly derived from the observed peak area N_{meas} :

$$N_5 = \underbrace{\left(1 - \frac{N_{1+5} + N_{4+5} - N_{2+3}}{N_5} \right)^{-1}}_{k_{\text{total}}} \times N_{\text{meas}} \quad . \quad (3.18)$$

It has to be pointed out that the correction factor k_{total} only involves information about the decay scheme and the detection efficiency and is independent of the activity A_0 .

For the experiments of this thesis, correction factors have been determined for each transition used for the analysis of the photoneutron reaction yields. Some decay schemes have been much more complicated than in the example discussed, giving rise to many more correction terms. However, the basic principle of the correction procedure has remained unchanged in these cases. A list of correction factors determined for the decays studied in the experiments of this thesis is shown in Sec. C.2 of the appendix.

Some final remarks shall be added to point out some simplifications implicitly applied for the determination of the correction factor k_{total} . First, any coincidences stemming from more than two transitions have been neglected in the correction procedure. This is a reasonable simplification because all correction terms taken into account are of the order $o(\epsilon^2)$, whereas the leading term N_5 is of the order $o(\epsilon)$. Coincidences of more than two transitions would be at least of the order $o(\epsilon^3)$. Since the detection efficiency is usually much smaller than unity, those correction terms would only give a minor contribution to the total correction factor.

Secondly, it has been assumed that the angular distribution of photons emitted by subsequent transitions is isotropic. However, as long as a large solid angle is covered, i. e., for small distances between detector and source, the detector averages over a large interval of the angular distribution. In this case, corrections due to the angular distribution are almost negligible. Larger corrections are expected with increasing distance, but at large distances summing effects only play a minor role due to the small detection efficiency. Therefore, assuming an isotropic angular distribution will not involve a significant error in the data analysis.

Further discussions about the correction of summing effects can be found in Refs. [50–52].

3.3 Determination of the photon flux

To determine absolute cross sections of photodisintegration reactions, it is mandatory to know the time-integrated photon flux of the irradiation. Due to the very intense photon beam, it is hardly possible to directly measure the photon flux by means of a photon detector placed in-beam straight behind the experimental setup. Thus, the photon flux is adopted from extensive Monte Carlo simulations which have to be normalized to the reaction yields of various standard reactions measured simultaneously during the irradiation. A short description of these simulations will be presented in the next section, whereas the various standard reactions are discussed in Sec. 3.3.2.

3.3.1 Spectral shape of bremsstrahlung

The spectral shape of the photon flux at both target positions in front of and behind the collimator is obtained from detailed simulations using the Monte Carlo code GEANT4 [43]. The simulations account for the electron exit window of the accelerator made out of aluminium of

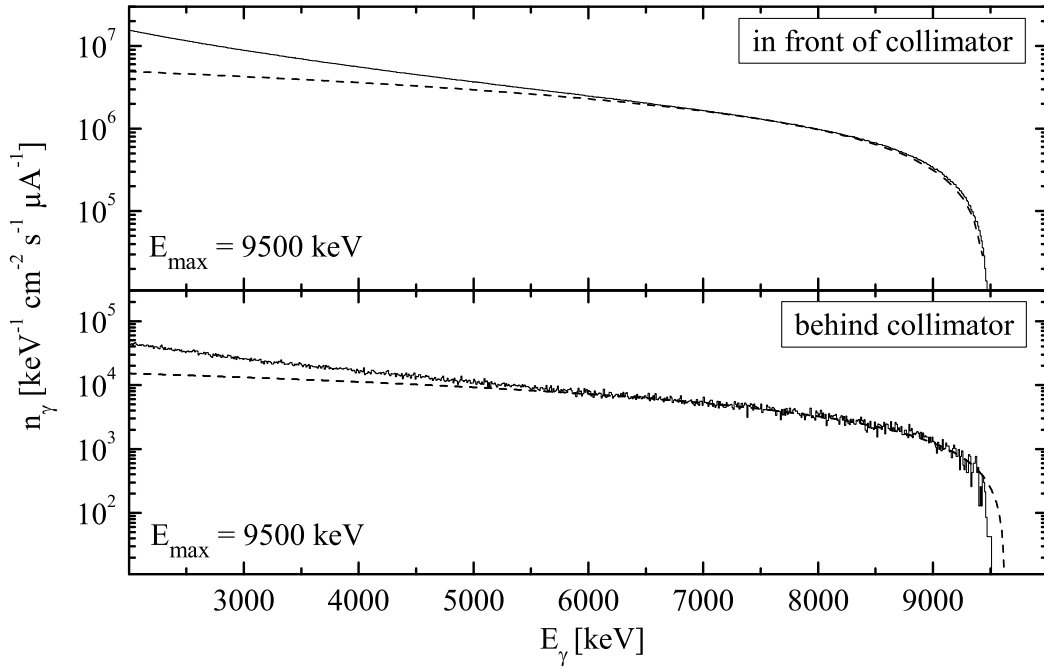


Fig. 3.14: The spectral shape of bremsstrahlung of maximum photon energy $E_{\max} = 9500$ keV obtained from a simulation with GEANT4 (solid line). For photon energies $E_\gamma > 6500$ keV, the spectrum can be accurately described by the parametrization stated in Chapter A of the appendix (dashed line). However, some larger discrepancies appear close to E_{\max} .

130 μm thickness, the copper radiator of 12 mm thickness as well as the thick copper collimator with a length of 955 mm. The entrance and exit hole of the collimator have diameters of 11.4 mm and 19.8 mm, respectively. The simulations have been carried out for a wide range of beam energies. For illustration, a simulated bremsstrahlung spectrum for a beam energy of $E_0 = 9500$ keV is shown in Fig. 3.14. Although simulations have been performed for each beam energy used in the experiment, a parametrization of the energy-dependent photon flux has been derived from a large set of simulations to provide a simple description for a wide energy range. This parametrization will be presented in Chapter A of the appendix.

3.3.2 Absolute normalization of the photon flux

The absolute normalization of the time-integrated photon flux can be derived from the reaction yields of standard reactions with well-known cross sections. For this purpose, the photoneutron reactions $^{187}\text{Re}(\gamma, n)$ and $^{197}\text{Au}(\gamma, n)$ and the photon-scattering reaction $^{11}\text{B}(\gamma, \gamma')$ are dedicated reactions, respectively. Both types of reaction will be discussed in the following.

Normalization of the photon flux via photoneutron reactions

For this technique, standard targets are irradiated both in front of and behind the collimator to normalize the absolute photon flux at both target positions by means of the measured reaction yields. With $N_{\gamma,\text{sim}}(E, E_{\text{max}})$ denoting the simulated spectral distribution of bremsstrahlung of maximum photon energy E_{max} , the normalization factor $N_{\gamma,0}^{E_{\text{max}}}$ for the simulation can be derived from Eq. (3.1):

$$N_{\gamma,0}^{E_{\text{max}}} = \frac{Y^{E_{\text{max}}}}{N_T \int N_{\gamma,\text{sim}}(E, E_{\text{max}}) \sigma(E) dE} , \quad (3.19)$$

where σ denotes the photoneutron cross section of the standard target. Thus, the normalization of the photon flux can be directly determined by the well-known cross section σ and the experimentally determined reaction yield $Y^{E_{\text{max}}}$.

In this thesis, gold and rhenium targets were used as standard targets because the reactions $^{187}\text{Re}(\gamma, n)$ and $^{197}\text{Au}(\gamma, n)$ have been studied in the astrophysically relevant energy region in previous experiments [46, 48]. The cross section of ^{187}Re has been adopted from the empirical parametrization given in Ref. [48]:

$$\sigma^{^{187}\text{Re}}(E) = (81.64 \pm 8.029) \times \left(\frac{E - S_n}{S_n} \right)^{0.5} , \quad (3.20)$$

where S_n quotes the neutron separation energy.

A similar parametrization for the cross section of ^{197}Au has been determined in Ref. [46]. However, this parametrization had to be revised because summing effects stemming from the β decay of ^{196}Au had not been treated properly in the data analysis of this work as outlined in Sec. 3.2.4. A reanalysis of the data yielded a slightly increased cross section, which has been used for the absolute normalization of the photon flux in this thesis:

$$\sigma^{^{197}\text{Au}}(E) = (152.7 \pm 19.5) \times \left(\frac{E - S_n}{S_n} \right)^{0.545} , \quad (3.21)$$

This cross section is about 4.4% larger than quoted in Ref. [46].

Normalization of the photon flux via photon-scattering reactions

A second approach for the normalization of the photon flux is to observe the photon-scattering reaction $^{11}\text{B}(\gamma, \gamma')$ with HPGe detectors behind the collimator (see Fig. 3.2). The reaction yield for a certain transition from a state of energy E_i into a state of energy E_j is given by:

$$Y_{i \rightarrow j} = N_{\text{Bor}} \times N_{\gamma}(E_i, E_{\text{max}}) \times I_{i \rightarrow j} , \quad (3.22)$$

where N_{Bor} is the number of ^{11}B nuclei in the target and $I_{i \rightarrow j}$ denotes the integrated cross section of the observed γ transition. Since the reaction yield $Y_{i \rightarrow j}$ can be derived from the spectra measured with HPGe detectors and $I_{i \rightarrow j}$ is well known for several transitions in ^{11}B up to an energy of about 9000 keV, one can directly determine the absolute photon flux at various energies by analyzing different transitions.

However, an accurate knowledge of the detection efficiency is mandatory for the determination of $Y_{i \rightarrow j}$. Therefore, simulations using GEANT4 have been performed with regard to the detailed geometry of the various detectors used in the experiments (see Tab. B.2 of the appendix). The simulations accounted for several sets of lead and copper absorbers in front of the detectors which are usually used to reduce low-energetic background during the experiment.

Measurements of the detection efficiency using the calibration sources ^{22}Na , ^{54}Mn , and ^{60}Co , respectively, served as a normalization for the simulations. Additionally, a non-calibrated ^{56}Co source that provides many γ transitions up to an energy of about 3500 keV has been used to confirm the energy-dependence of the simulated efficiency. Results for different sets of absorbers used in the experiments of this thesis are illustrated in Fig. 3.15 proving that the simulation provides a reliable description of the energy-dependent detection efficiency. A mean deviation between the experimental data points and the simulated efficiency curve of less than 5% has been determined. However, to account for additional uncertainties due to the extrapolation of the detection efficiency to higher energies where no experimental data was available, an overall uncertainty of 10% has been estimated.

With the knowledge of the detection efficiency, the reaction yield $Y_{i \rightarrow j}$ of the photon-scattering reaction can be determined from the observed γ transitions, and the absolute photon flux at various energies can be derived from Eq. (3.22). The analysis of $Y_{i \rightarrow j}$ involves several additional correction terms, e. g., the angular distribution of the observed photons and the feeding of low-lying levels. However, this shall not be further discussed here, and the reader is referred to Ref. [41] where a detailed description is given.

Finally, the analysis of the photon-scattering reaction provides data points for the absolute photon flux at several photon energies which serve as a normalization for the simulated photon spectrum. For illustration, data points from an experiment using bremsstrahlung of $E_{\text{max}} = 9500$ keV are shown in Fig. 3.16 and compared with normalized simulations using GEANT3 and GEANT4, respectively.

As shown in Fig. 3.16, GEANT3 is not able to accurately describe the spectral shape close to E_{max} . Therefore, previous works had to apply a correction procedure to adjust the simulations to the experimental data point at $E_{\gamma} = 8916.3$ keV [41]. This procedure gave rise to large systematic uncertainties, in particular for experiments performed in front of the collimator where no experimental data for the photon flux had been available to confirm the validity of this correction procedure. Therefore, previous experiments were usually restricted to irradiations behind the collimator.

In comparison, simulations using GEANT4 are in much better agreement with the experimental

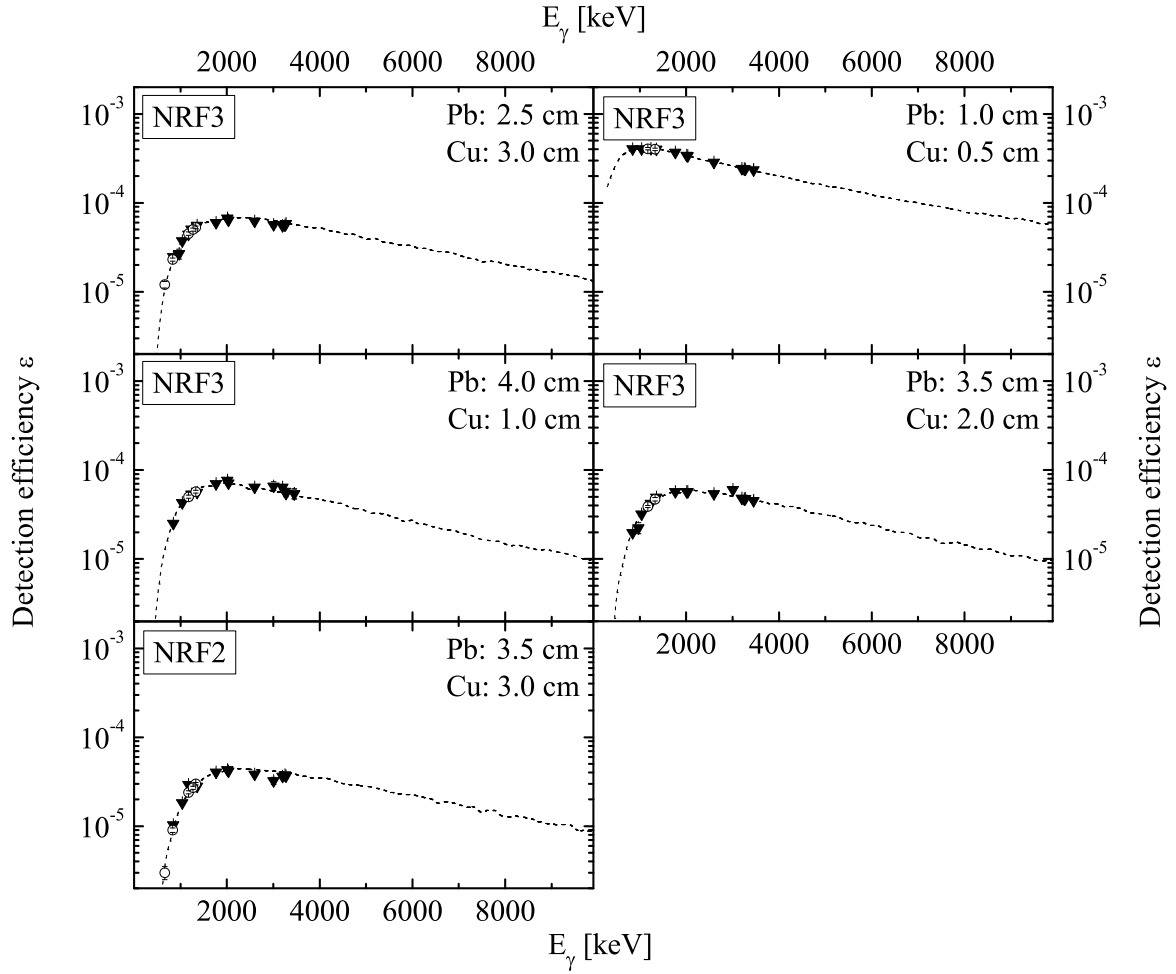


Fig. 3.15: Detection efficiency of HPGe detectors at the photoactivation setup using lead and copper absorbers of various thickness. Specifications of the detectors *NRF2* and *NRF3* are summarized in Tab. B.2 of the appendix. The dashed line shows the simulated efficiency curve using GEANT4, which has been normalized to data points stemming from several calibration sources (open circles). A non-calibrated ^{56}Co source has been used to confirm the energy dependence of the simulated detection efficiency (triangles).

data points showing that a correction procedure no longer needs to be applied. Measurements for many different energies E_{max} have confirmed that these simulations provide a reliable overall description of the photon flux. A mean deviation of about 15% has been found between experimental data and simulation. Therefore, it can be assumed that these simulations also yield an accurate description of the photon flux in front of the collimator within the quoted uncertainty of 15%. Further confirmation of the reliability of bremsstrahlung simulations using GEANT4 will be given in Sec. 3.4.2 where experimental data stemming from direct measurements of bremsstrahlung spectra are provided.

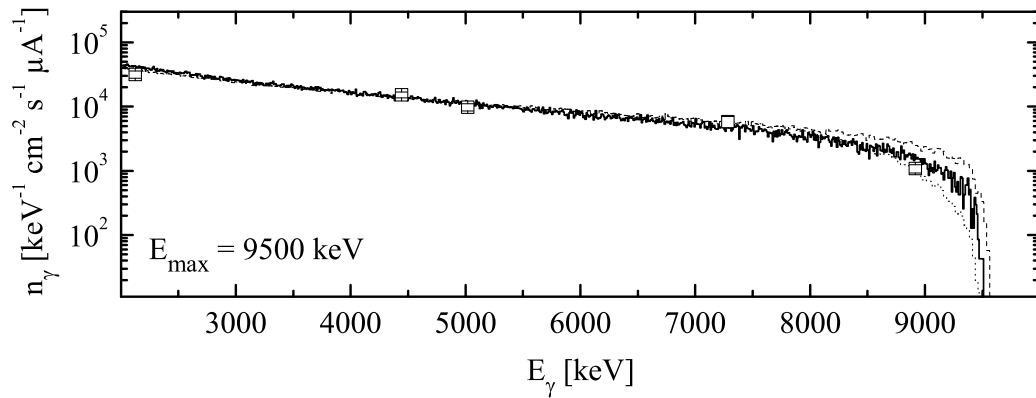


Fig. 3.16: Simulations of a bremsstrahlung spectrum using GEANT3 (dashed line) and GEANT4 (solid line) are compared to experimental data points (open squares) stemming from the photon-scattering reaction $^{11}\text{B}(\gamma, \gamma')$. The data points are in good agreement with the simulation using GEANT4, whereas the simulation using GEANT3 shows a large discrepancy to the data point at $E_\gamma = 8916.3$ keV. Hence, a correction procedure was applied to simulations using GEANT3 in previous works [41]. The dotted line shows the corrected spectrum.

A final remark is that photon-scattering reactions only allow for the normalization of the photon flux behind the collimator. However, with regard to the reliable overall description provided by the simulations, it can be assumed that the determined normalization factor behind the collimator is also valid for the photon-flux simulation at the target position in front of the collimator. This assumption will be confirmed in the next paragraph.

Comparison of various standard reactions

To check the reliability and consistency of the absolute photon flux normalization derived from the various standard reactions, several independent measurements have been performed and normalization factors for the photon flux have been determined by means of each standard reaction. The results are compared in Fig. 3.17.

The normalization factors derived from the various standard reactions are in good agreement to each other. Whereas both photoneutron reactions $^{187}\text{Re}(\gamma, n)$ and $^{197}\text{Au}(\gamma, n)$ yield consistent results within the adopted cross-section uncertainties of these reactions, a deviation of about 20% can be found in comparison to the photon-scattering reaction $^{11}\text{B}(\gamma, \gamma')$. However, this discrepancy can be understood with regard to the assumed uncertainties for the spectral shape of the photon flux.

Moreover, Fig. 3.17 implies that the normalization factors determined for the photon flux behind the collimator are almost equal to those determined independently in front of the collimator.

This is a further indication that the simulations using GEANT4 provide an accurate description of the photon flux both in front of and behind the collimator.

In conclusion, the data shown in Fig. 3.17 have proven the reliability of various standard reactions and confirmed that the absolute photon flux during an irradiation can be determined with an uncertainty of less than 20%.

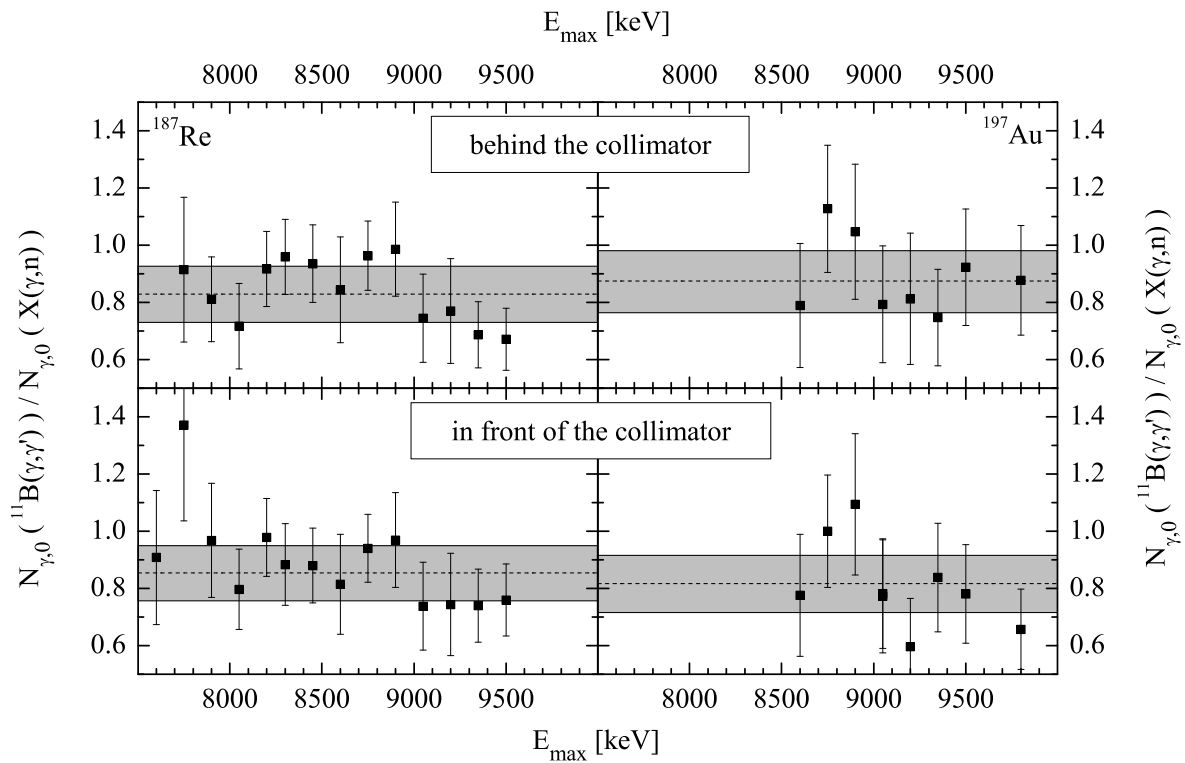


Fig. 3.17: Normalization factors for the photon flux derived from the photoneutron reactions $^{187}\text{Re}(\gamma, n)$ (left panels) and $^{197}\text{Au}(\gamma, n)$ (right panels) are compared to those determined by the photon-scattering reaction $^{11}\text{B}(\gamma, \gamma')$. The data stem from a photoactivation experiment that will be discussed in Sec. 4.1. Since no experimental data for $^{11}\text{B}(\gamma, \gamma')$ were available in front of the collimator, the quoted ratio for each energy has been calculated by means of the same normalization factor $N_{\gamma,0}(^{11}\text{B}(\gamma, \gamma'))$ in front of and behind the collimator. The experimental error bars take into account uncertainties for the spectral shape of the photon flux and uncertainties stemming from the reaction yield determination of the various standard reactions. The gray error band denotes the uncertainty of the adopted photoneutron cross sections of ^{197}Au and ^{187}Re [46, 48], respectively. The various standard reactions are found to be consistent within the quoted uncertainties. The mean ratio is indicated by a dashed line.

3.4 Determination of the beam energy

It is essential to know the absolute beam energy for the determination of photodisintegration cross sections in photoactivation experiments, especially just above the particle threshold. This is illustrated in Fig. 3.18 where the expected reaction yield for the photoneutron reaction $^{154}\text{Sm}(\gamma, n)$ has been calculated as a function of beam energy using a theoretical cross-section prediction. It can be clearly seen, that for beam energies as low as a few hundred keV above the threshold a 25 keV uncertainty of E_0 already gives rise to very large uncertainties of the predicted reaction yield. Unfortunately, this is the most relevant energy region for astrophysical investigations. Therefore, reliable experimental data of astrophysical implication can only be provided if the beam energy is well controlled during the irradiation and systematic uncertainties in the determination of the beam energy are reduced to a minimum.

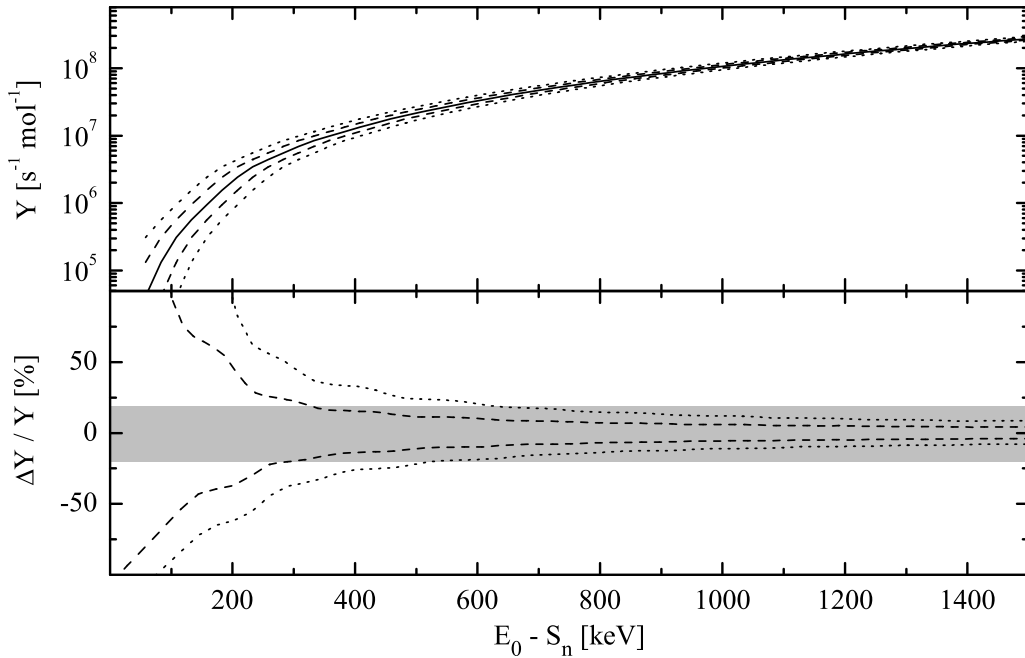


Fig. 3.18: Sensitivity of the photoneutron reaction yield Y to the absolute beam energy E_0 . *Top panel:* The solid line shows the expected photoneutron reaction yield of ^{154}Sm assuming a photoneutron cross section adopted from a NON-SMOKER^{WEB} calculation. The dashed and dotted lines indicate the error bands assuming uncertainties for the beam energy of $\Delta E_0 = 25$ keV and 50 keV, respectively. S_n denotes the neutron separation energy of ^{154}Sm . *Bottom panel:* The relative uncertainty of the predicted reaction yield due to uncertainties of the beam energy is plotted as a function of $E_0 - S_n$. Close to the neutron threshold, this uncertainty clearly dominates other experimental uncertainties indicated by the gray band. A detailed discussion of these uncertainties is provided in Sec. 3.5.

As described in Sec. 3.1, the beam energy is conventionally adjusted by the use of a deflecting magnet in front of the experimental setup. However, only few attempts have been made in the past to confirm the reliability of this technique as applied at the photoactivation setup [53, 54]. The adjustment of beam energy has therefore been subject to large systematic uncertainties, which have only been estimated so far. The intention of this section is to constrain these systematic uncertainties by means of several experimental approaches.

3.4.1 Offline method using a deflecting magnet

The beam energy at the photoactivation setup can be derived from the deflection of the electron beam by a well-calibrated 40° deflecting magnet. The beam energy E_0 is then determined by [55]:

$$E_0 = m_0 c^2 \left(\sqrt{\frac{e^2 \rho^2}{m_0^2 c^2} B^2 + 1} - 1 \right) , \quad (3.23)$$

where m_0 denotes the electron mass and B is the magnetic field strength corresponding to a 40° deflection of electrons with kinetic energy E_0 . The effective radius of curvature ρ depends on the detailed field characteristics of the magnet and can be adopted from analytic calculations. Thus, E_0 can be directly determined by the measured magnetic field B . This technique will be referred to as the *conventional technique* in the discussion of the following sections.

This technique is subject to several uncertainties. First of all, the calculation of ρ requires a detailed knowledge of the magnetic field including fringe fields. Hence, any uncertainties in the magnetic field distribution will give rise to systematic uncertainties of ρ and, thus, of E_0 . Secondly, even if ρ is known with high accuracy, Eq. (3.23) only holds for a central electron beam traversing the symmetry plane of the magnet. Any deviation from this ideal trajectory will result in a wrong assignment of magnetic field and energy. The sensitivity of the energy determination to the adjustment of beam position has been studied in detail in Ref. [53]. It was found that even rather small maladjustments of the beam position give rise to uncertainties of about $\Delta E_0 = 50$ keV. However, this uncertainty only refers to the reproducibility of this technique and does not account for any systematic discrepancies of the absolute beam energy. Finally, it has to be mentioned that this technique as applied at the photoactivation setup is restricted to beam currents below 100 nA because the beam position behind the deflecting magnet has to be observed with fluorescence targets. Hence, one cannot exclude that any energy drifts occur when higher beam currents are used in the experiment.

To constrain these systematic uncertainties, two different measurements have been performed which will be described in the following two sections.

3.4.2 Direct measurement of bremsstrahlung spectra

As a first approach to determine the absolute beam energy E_0 independently of the conventional technique, the spectral distribution of the photon flux at the photoactivation setup has been measured directly using a HPGe detector (detector *NRF4* of Tab. B.2 of the appendix). The detector was placed in-beam directly behind the collimator, and its front side was shielded with copper of 1 cm thickness to reduce the low-energetic photon background. A very low beam current had to be used not to exceed count rates of a few kHz in the detector, which would have caused a significant amount of pile-up effects. Spectra were measured for three different beam energies adjusted via the conventional method of Sec. 3.4.1 to $E_0^{\text{Conv}} = 8000$ keV, 8087 keV, and 8197 keV and are shown in Fig. 3.19.

Since bremsstrahlung spectra, in general, exhibit a sharp cut-off in the spectral distribution, the original idea of this approach was to determine the beam energy from this cut-off, which was expected to be found close to E_0^{Conv} in the measured spectra. However, as shown in Fig. 3.19, the spectra are smeared out significantly at these energies making it hardly possible to clearly identify the position of the cut-off. It has been assumed for further analysis that this smearing-out has been caused by a small fraction of pile-up events which evenly spread over the spectra. The average number of pile-up events per energy bin was determined from events of energy above E_0^{Conv} and has then been subtracted from the spectra as illustrated in Fig. 3.19. Even after this correction, the cut-off still could not be determined accurately due to insufficient statistics and, thus, the idea was to derive E_0 from the shape of the measured spectra instead.

Therefore, the spectral distribution has been simulated in detail with GEANT4 for several energies (denoted by E_0^{Sim}) close to E_0^{Conv} taking into account that the measured spectra are a convolution of photon-flux distribution and detector response. As shown in Fig. 3.19, the overall agreement between measurement and simulation is excellent. Furthermore, the spectral shape in the energy range between 3000 and 6000 keV was found to be almost independent of the adopted energy E_0^{Sim} but differed significantly for energies close to the cut-off.

Hence, as a first step of the analysis, the simulated spectra of various energies E_0^{Sim} have each been normalized to the measured spectra for energies between 3000 to 6000 keV. In a second step, the normalized simulations have been compared to the measurements in the energy range between 6000 to 8000 keV by means of a χ^2 test, whereas the minimum value of χ_{red}^2 has been expected to yield the most probable value of the true beam energy. The results of this analysis are shown in Fig. 3.20.

Due to large statistical uncertainties in both the measured and simulated spectra close to the cut-off, the data points are subject to large fluctuations which hamper a clear determination of the minimum χ_{red}^2 . Nevertheless, the results obtained from this measurement already allow to constrain the uncertainty of the absolute beam energy to about 50 keV and are found to be in good agreement with the beam energies adopted from the conventional method.

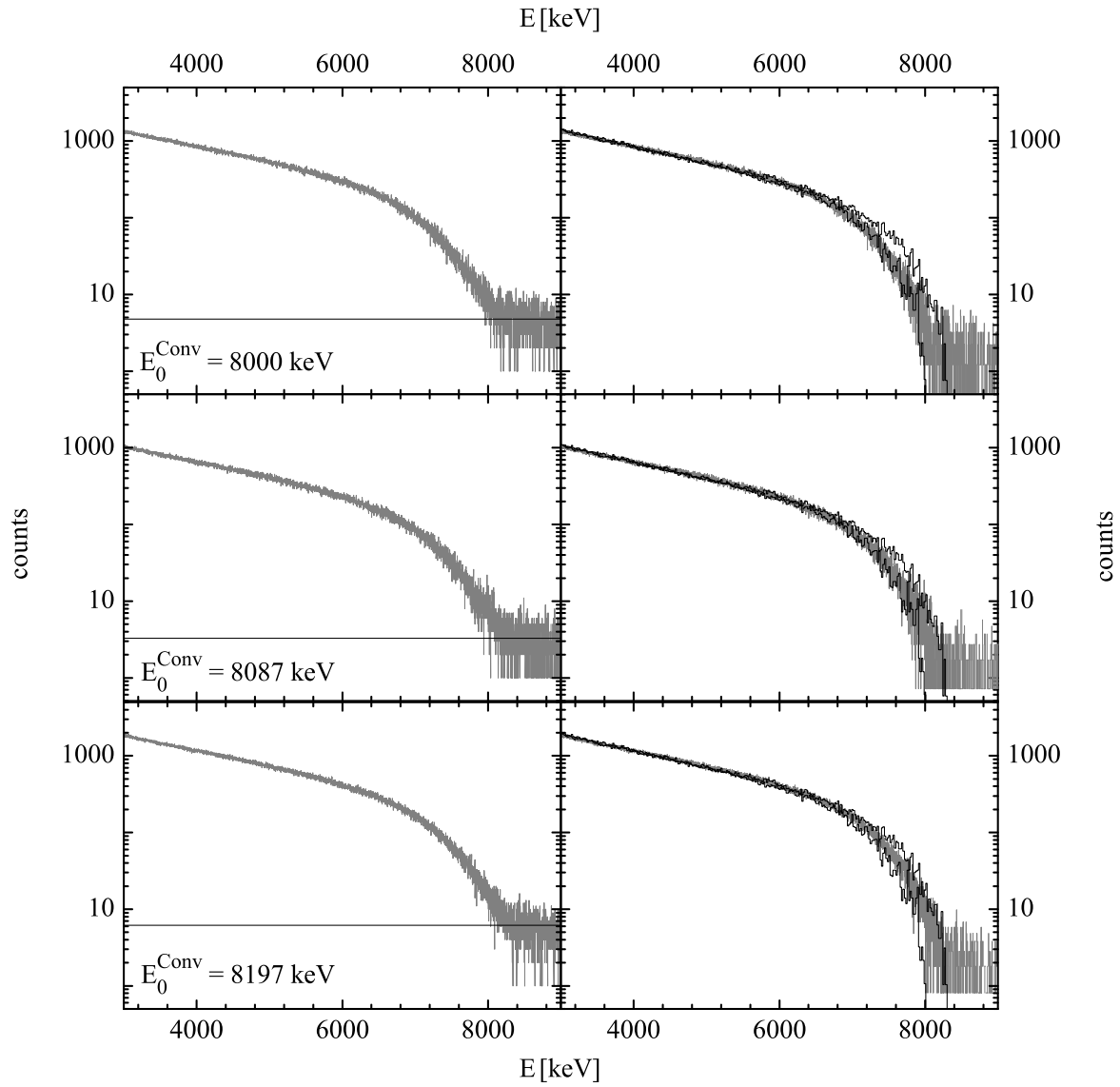


Fig. 3.19: Direct measurement of bremsstrahlung using a HPGe detector at beam energies $E_0^{\text{Conv}} = 8000$ keV, 8087 keV, and 8197 keV, respectively (gray histograms). The beam energy was adjusted by means of the conventional method of Sec. 3.4.1 and each spectrum was accumulated for a period of about 1 h. *Left panel:* The spectra show no clear cut-off close to E_0^{Conv} , presumably due to pile-up effects in the detector. Solid lines indicate the assumed averaged rate of pile-up events per energy bin derived from events of energies $E > E_0^{\text{Conv}}$. *Right panel:* The averaged rate of pile-up events has been subtracted from the measured spectra. For comparison with the corrected spectra, two simulations for beam energies $E_0^{\text{Sim}} = 8025$ keV and 8325 keV are shown (black histograms). Each simulation has been normalized to the corrected spectra for energies between 3000 and 6000 keV. See text for details.

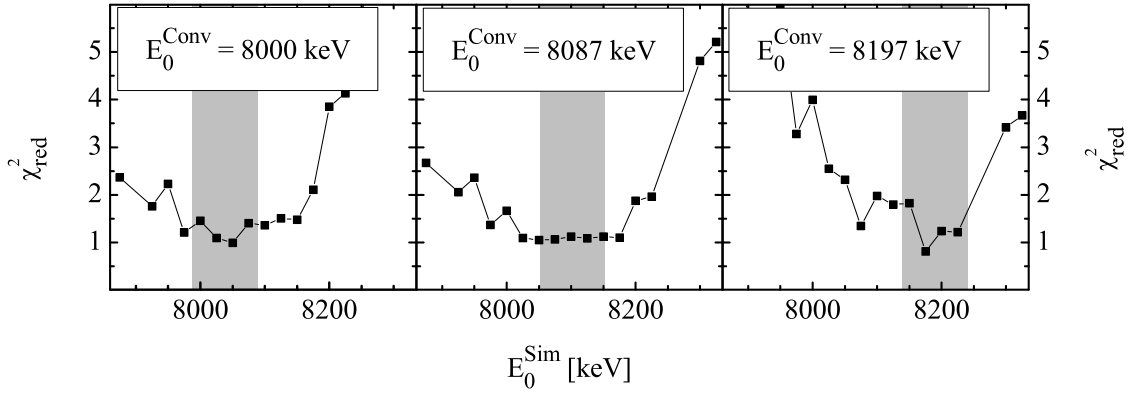


Fig. 3.20: Comparison of directly measured bremsstrahlung spectra with simulations using GEANT4. Simulations have been performed for various beam energies E_0^{Sim} and compared to the measured spectra via a χ^2 test. The beam energy for the measurement (denoted by E_0^{Conv}) has been adjusted by the conventional method of Sec. 3.4.1. Although no clear minimum of χ^2_{red} can be identified, the beam energy can already be estimated with an uncertainty of about 50 keV (gray band). See text for more details.

3.4.3 Photoactivation very close to the neutron threshold

In this section, the approach will be discussed to constrain the beam energy by analyzing the reaction yields of various photoneutron reactions for beam energies very close to the neutron separation energy. As shown in Fig. 3.18, the reaction yield of photoneutron reactions just above the threshold is highly sensitive to the beam energy. While this sensitivity hampers an accurate determination of cross sections close to the threshold, it allows to strongly constrain the absolute beam energy from a measured reaction yield if the cross section is already well known. Unfortunately, there are no reliable experimental cross-section data very close to the neutron threshold available, but it will be demonstrated in this section that a reasonable analysis can already be performed by adopting the cross section from theoretical calculations assuming uncertainties within a factor of 2. Therefore, the idea of this approach is to constrain the beam energy by comparing experimental yields with theoretical predictions.

Several sets of target nuclei with similar neutron separation energies were irradiated for a period of about two hours, each using beam energies close to the neutron threshold. The target specifications are summarized in Tab. 3.1. The beam energy was adjusted by means of the conventional method of Sec. 3.4.1, and irradiations were performed in steps of 25 keV at energies of $E_0^{\text{Conv}} = 9125$ keV, 9150 keV, 9175 keV, 9200 keV, and 9225 keV, respectively. Since experimental conditions such as beam adjustments were kept constant for all of these irradiations, it can be assumed that the various beam energies used for the measurements have been accurately known relatively to each other. This is essential for studying the reaction yield as a function of beam energy.

Isotope	Form	Weight [g]	S_n [keV]	E_γ [keV]	I_γ [%]
^{127}I	KI	4.5 – 5	9143.91	388.6	35.6 ± 0.4
^{140}Ce	CeO_2	2.5 – 3	9202.1	165.85	79.9 ± 0.05
^{121}Sb	Sb_2O_3	4 – 5	9241.96	89.8	79.5 ± 1.6

Tab. 3.1: Specifications of targets irradiated very close to the neutron separation energy S_n . I_γ denotes the intensity per decay for a γ transition of energy E_γ .

The experimental reaction yields were determined after the irradiation by the analysis described in Sec. 3.2 and compared to theoretical predictions. The results are shown in Fig. 3.21. The measured reaction yields highly exceeded the theoretical predictions even if the uncertainty for the adopted cross section is taken into account. This indicates that the true beam energy was actually higher than determined from the conventional method.

To further constrain the beam energy, the experimental data points have been fitted to the theoretical predictions by means of two free parameters, one describing an energy shift of the data points (denoted by ΔE_0^{Conv}) and a second one quoting the absolute normalization of the predicted cross section (denoted by f). The best combination of these two parameters has then been derived from a χ^2 test. In case of the reaction $^{127}\text{I}(\gamma, n)$, a minimum χ_{red}^2 was found for

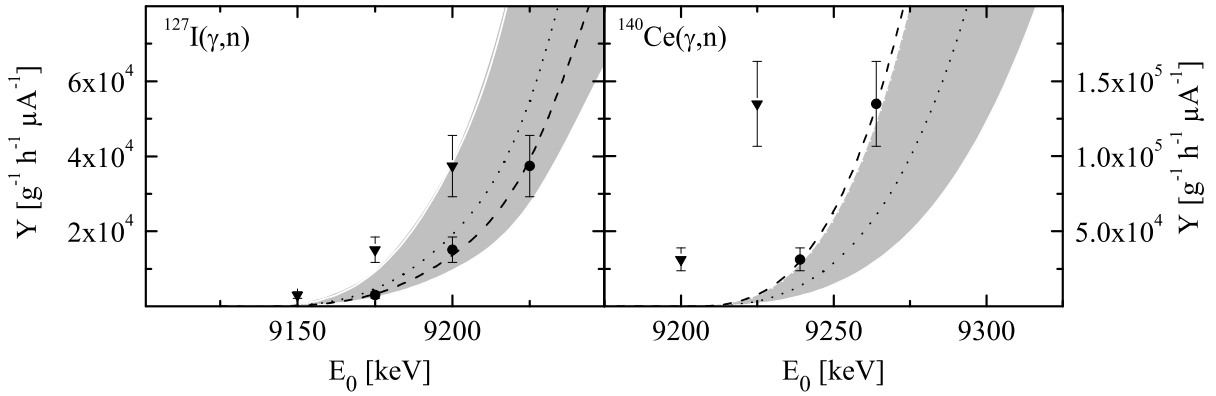


Fig. 3.21: Reaction yields for photoneutron reactions very close to the neutron threshold for $^{127}\text{I}(\gamma, n)$ (left panel) and $^{140}\text{Ce}(\gamma, n)$ (right panel). A theoretical prediction for the reaction yield using the TALYS code [30] is shown by the dotted line. The gray error band accounts for the uncertainty of the theoretical cross-section prediction. The measured reaction yields are shown as triangles assuming a beam energy derived from the conventional method described in Sec. 3.4.1. The error bars quote the experimental uncertainties discussed in Sec. 3.5. To determine the correct beam energy of the irradiation, the data points have been adjusted to the theoretical prediction by means of a χ^2 test which yields a combination of energy-shifted data points (circles) and normalized theoretical predictions (dashed lines). See text for details.

an energy shift of $\Delta E_0^{\text{Conv}} = 25$ keV and a normalization factor $f = 0.71$. For $^{140}\text{Ce}(\gamma, n)$, these parameters have been determined to $\Delta E_0^{\text{Conv}} = 39$ keV and $f = 2.2$. Although the normalization factor found for $^{140}\text{Ce}(\gamma, n)$ is larger than the assumed uncertainty of a factor of 2, the result is still consistent with regard to the rather large experimental error bars quoted for the data points. As shown in Fig. 3.21, the agreement between the energy-shifted experimental data points and the normalized theoretical prediction is excellent, confirming the reliability of this approach. It needs to be added that no data points have been obtained for the reaction $^{121}\text{Sb}(\gamma, n)$ either because the true beam energy was below the neutron threshold or the reaction yield was below the sensitivity limit for detection.

In conclusion, the results of this analysis indicate that the absolute value of the beam energy has been slightly underestimated by the conventional technique quoting a deviation to the true beam energy between 25 keV and 50 keV. However, this deviation is still fully consistent with the uncertainty stated for the reproducibility of the conventional technique.

3.4.4 Charge distribution in a segmented radiator

All of the approaches discussed in the preceding sections are not capable to provide an online control of the beam energy at high beam currents during the experiment. However, it is desirable to record the beam energy as a function of time to correct any energy drifts occurring on relatively short time scales.

For this purpose, a simple idea is to measure the penetration depth of the incident electron beam in the radiator because the range of an electron in matter directly depends on its energy. Although the penetration depth cannot be determined for each single electron in the experiment, a mean penetration depth of the electron beam can be derived from measuring the distribution of charge deposition in the radiator.

This approach has been realized using a fourfold segmented copper radiator with a thickness of 3 mm per segment [54]. It was found that the beam energy can already be accurately determined by the charge ratio of the first two segments as illustrated in Fig. 3.22. This technique is highly sensitive to relative changes in the absolute beam energy, and, thus, provides a reliable online control if the charge ratio is recorded as a function of time during the experiment. For the determination of absolute beam energy the charge ratio as a function of energy can be either derived from simulations or from an experimental calibration using the conventional method described in Sec. 3.4.1. However, as shown in Fig. 3.22, the this way determined calibration curves exhibit rather large discrepancies which have to be fully understood before applying this technique to derive absolute beam energies.

In conclusion, this simple approach allows to monitor energy drifts of less than 25 keV during the experiment. The accuracy might even be increased if more sophisticated methods are applied to analyze the charge distribution, e. g., using a higher segmentation of the radiator.

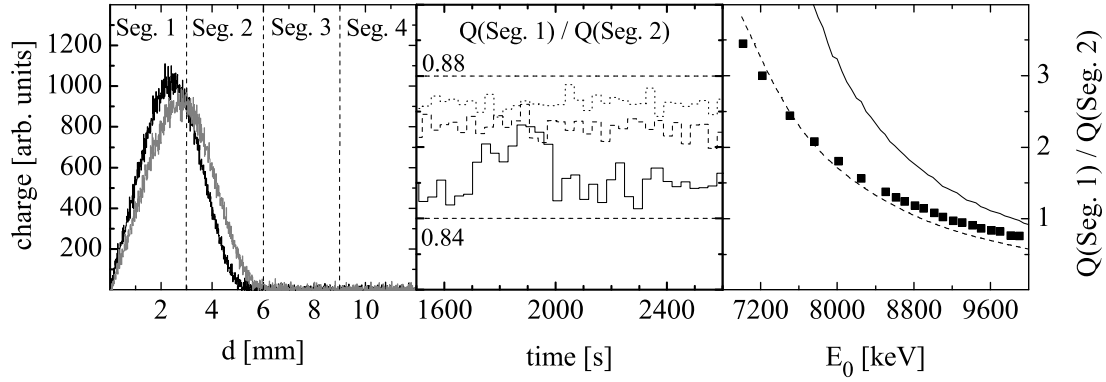


Fig. 3.22: Distribution of deposited charge in a segmented radiator. *Left panel:* Simulated charge deposition of an electron beam of energy $E_0 = 8000$ keV (black histogram) and $E_0 = 9000$ keV (gray histogram), respectively, in a copper radiator as a function of penetration depth d . The vertical dashed lines indicate the segmentation of the radiator. *Middle panel:* Charge ratio of the first two segments measured as a function of time during an irradiation with beam energies of $E_0 = 9175$ keV (dotted histogram), 9200 keV (dashed histogram), and 9225 keV (solid histogram), respectively. The charge ratios were averaged over 30 s yielding mean values between $\frac{Q(\text{Seg.1})}{Q(\text{Seg.2})} = 0.84$ and 0.88 . Fluctuations of beam energy were found to be less than 25 keV. *Right panel:* Charge ratio of the first two segments as a function of beam energy. The data points stem from an experimental calibration by means of the conventional method described in Sec. 3.4.1, whereas the solid line refers to a simulation. In addition, the dashed line shows a simulation for a slightly adjusted thickness of each segment (2.65 mm). Although the absolute value for the charge ratio is much better described by the adjusted simulation, discrepancies concerning the energy dependence have not yet been solved.

3.4.5 Comparison and summary of various techniques

This section gives a short summary of the various experimental techniques for beam energy determination described in the preceding sections. Therefore, the key features of each technique concerning accuracy, effort, and applicability as an online control are compared in Tab. 3.2. Each technique exhibits advantages and disadvantages for the application as an energy monitor in the experiment. Apparently, the accuracy of a certain method increases with the effort of the corresponding measurement. Moreover, only the technique described in Sec. 3.4.4 provides a full online control during the experiment but has not been capable so far to provide the absolute value of beam energy without a previous calibration.

In conclusion, the beam energies derived from the various techniques were found to be in good agreement to each other. It could be confirmed that the absolute beam energy can be adjusted using the conventional technique described in Sec. 3.4.1 with an uncertainty of less than 50 keV. For the experiments presented in this thesis, the absolute beam energy has only been adjusted by

	Accuracy	Effort	I_e^{\max}	Online control
Conventional (Sec. 3.4.1)	< 50 keV	~ 1 min	100 nA	no
Bremsstrahlung (Sec. 3.4.2)	< 50 keV	~ 1 h	10 nA	no
Reaction yield (Sec. 3.4.3)	< 25 keV	~ 1 d	full current	no
Charge ratio (Sec. 3.4.4)	-	~ 1 s	full current	yes

Tab. 3.2: Specifications of various techniques for the determination of beam energy. The accuracy refers to the determination of the absolute beam energy E_0 . Relative changes in energy might be measured with higher accuracy. The typical time needed to perform the measurement and analysis of a certain method is denoted by the effort. The maximum beam current applicable using a certain method is quoted by I_e^{\max} .

means of the conventional method, whereas in more recent experiments additionally the charge ratio has been recorded as a function of time to assure the stability of the accelerator according to Sec. 3.4.4. Hence, a mean uncertainty of beam energy of 25 keV was taken into account. With regard to the huge uncertainties involved in any cross-section determination in the energy range very close to the threshold (see Fig. 3.18), experimental data points for photoneutron reactions have usually been discarded when stemming from irradiations which used beam energies as close as a few hundred keV above the neutron separation energy.

3.5 Systematic and statistical uncertainties

In this section, the uncertainties involved in the analysis of the photoactivation experiments presented in this thesis will be compared and summarized. Therefore, it will be distinguished between systematic uncertainties Δ_{sys} and statistical uncertainties Δ_{stat} . The latter are not correlated between different experimental runs at various beam energies and, therefore, can be reduced by a large number of individual measurements. An overview of the various contributions to the overall uncertainty is illustrated in Fig. 3.23. Each contribution quoted in this figure will be discussed in more detail in the following.

For the determination of reaction yields according to Sec. 3.2, one needs to take into consideration uncertainties of detection efficiency, self-absorption, summing correction, half-life, γ intensity, and the determination of peak areas in the measured spectra. However, the dominating contribution usually stems from the detection efficiency. As described in Sec. 3.2.2, the detection efficiency is derived from simulations which have been normalized to experimental data points obtained from calibration sources. The mean uncertainty has been found to be about 7%. This uncertainty has to be treated as a systematic uncertainty but can usually be further constrained if the reaction yield is derived from several γ transitions of different energy and intensity.

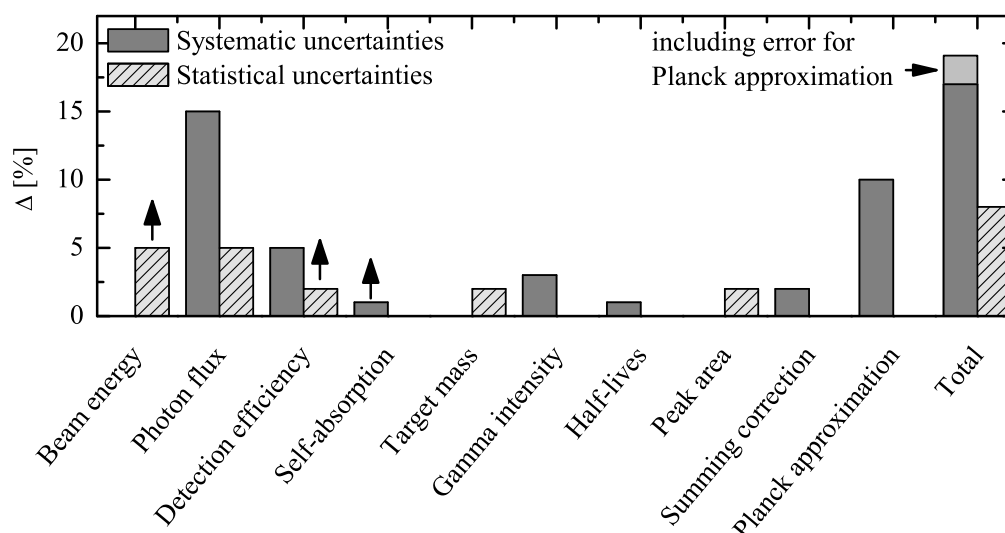


Fig. 3.23: Typical uncertainties of photoactivation experiments of this thesis. The arrows indicate a lower limit for the corresponding uncertainty if its absolute value is very sensitive to experimental conditions. The overall uncertainty is calculated by means of a Gaussian error propagation. See text for details.

Furthermore, it was outlined in Sec. 3.2.2 that an additional uncertainty arises from the positioning of targets in front of the detector which gives a contribution of up to 11% depending on the distance between detector and target. This uncertainty, however, can be treated statistically and, therefore, is reduced when averaging over many individual data points.

Contributions stemming from self-absorption, summing correction, half-life, γ intensity, and the determination of peak areas are usually relatively small and of the order of a few percent. The uncertainty of summing corrections will only show larger contributions in a few cases discussed in Sec. 4.4 of the next chapter.

When deriving absolute cross sections from the measured reaction yields and comparing experimental data with theoretical predictions, one needs to account for the uncertainties arising from the determination of photon flux and target mass. Whereas uncertainties of the target mass are almost negligible, a significant uncertainty stems from the determination of the photon flux as described in Sec. 3.3. On the one hand, a systematic contribution has to be taken into consideration due to an uncertainty in the adopted spectral shape of the photon flux. On the other hand, additional systematic uncertainties arise from the absolute normalization of the photon flux due to the uncertainties of the corresponding cross sections of the involved standard reactions. Hence, one has to account for uncertainties of the photoneutron cross sections of ^{187}Re and ^{197}Au and of the integrated cross sections of the γ transitions of ^{11}B , respectively. The overall systematic uncertainty stemming from the photon-flux determination has been estimated to be

approximately 15 to 20%. Moreover, the determination of the reaction yield of these standard reactions involves additional statistical uncertainties of about 5%.

As pointed out in Sec. 3.4, it is essential for the data analysis applied in this thesis to reliably adopt the absolute beam energy used for irradiation. As outlined, an uncertainty of 25 keV has been estimated for the determination of beam energy. Depending on the energy range studied in the experiment, this gives rise to large contributions to the overall uncertainty, in particular, if photoneutron reactions very close to the neutron threshold are measured. For the analysis of this thesis, it was assumed that this uncertainty can be treated statistically, i. e., the overall uncertainty is reduced by averaging over many independent measurements.

Finally, if astrophysically relevant ground-state reaction rates are determined according to the method described in Sec. 3.1.2, the uncertainty for the approximation of thermal Planck spectra has to be taken into account. Depending on how many data points and, hence, how many bremsstrahlung spectra are adopted for the approximation, contributions to the overall uncertainty of the order of 10% have been found.

In conclusion, the total uncertainty for the experiments of this thesis are mainly of systematic nature dominated by the photon flux determination. If statistical uncertainties are reduced by averaging over several data points, a total uncertainty of about 20 to 25% has to be accounted for when comparing experimental data with theoretical predictions.

Chapter 4

Experimental results

In this chapter, the results of several photoactivation experiments will be presented in which photoneutron reactions of various isotopes for incident photon energies just above the neutron separation energy have been studied. All experiments have been performed at the photoactivation setup of the superconducting electron linear accelerator S-DALINAC as described in the preceding chapter. The experimental results will be compared to theoretical predictions calculated with the TALYS and NON-SMOKER^{WEB} code, respectively. These two statistical model codes have been described in Sec. 2.3.

The first two sections will focus on the investigation of isotopes in the rare-earth region, where only few experimental data for photoneutron cross sections in the astrophysically relevant energy region close to the neutron threshold have been available so far. Therefore, photoneutron reactions of several isotopes ranging from ^{160}Gd down to the neutron-shell closure at ^{140}Ce have been studied to provide a reliable set of experimental data, which serve as a test for theoretical predictions.

The second part of this chapter will address photoneutron reactions in the heavy-mass region $A \geq 185$ which have already been studied extensively in previous photoactivation experiments [19, 26, 46–48, 56, 57]. To further expand this data set, the photoneutron reactions of $^{191,193}\text{Ir}$ and ^{192}Os have been measured, and the experimental results have been compared to theoretical calculations.

Finally, this chapter closes with a short overview and discussion concerning the obtained results.

4.1 Photoneutron reactions of rare-earth isotopes

4.1.1 Experiment and data analysis

The photoneutron reactions of the isotopes $^{148,150}\text{Nd}$, ^{154}Sm , and $^{154,160}\text{Gd}$ have been simultaneously measured in a single photoactivation experiment by the irradiation of naturally composed targets.

Thin metallic disks were used as neodymium and gadolinium targets ($m = 40 - 50$ mg). Since both elements are highly oxidative, the targets were prepared and weighed under the condition

of an argon atmosphere to avoid any oxidation of the material before weighing and, hence, to reduce systematic uncertainties in the determination of target mass. The samarium targets were made of Sm_2O_3 powder and pressed to thin disks ($m = 500 - 1750$ mg). The powder was heated before the target preparation to remove any amount of water within the material. Each target had a diameter of 20 mm. The target specifications are summarized in Tab. 4.1.

The targets were mounted directly in front of the photon collimator system at a distance of

Isotope	Form	N [%]	m [mg]	S_n [keV]	E_γ [keV]	I_γ [%]
^{148}Nd	metal foil	5.76	40-50	7332.9	91.1	27.9 ± 1.1
					531.0	13.1 ± 0.9
^{150}Nd	metal foil	5.64	40-50	7379.9	114.3	19.2 ± 1.5
					155.9	5.93 ± 0.31
					211.3	25.9 ± 1.4
					267.7	6.03 ± 0.28
					270.1	10.6 ± 0.5
^{154}Gd	metal foil	2.18	40-50	8894.8	97.4	29.0 ± 0.8
					103.2	21.1 ± 0.6
^{160}Gd	metal foil	21.86	40-50	7451.4	58.0	2.49 ± 0.07
					226.0	0.217 ± 0.002
					348.3	0.239 ± 0.003
					363.6	11.8 ± 0.1
^{154}Sm	Sm_2O_3	22.70	500-1750	7967.6	69.7	4.73 ± 0.04
					97.4	0.772 ± 0.019
					103.2	29.3 ± 0.2
^{187}Re	metal foil	62.60	320-340	7363.0	122.6	0.603 ± 0.003
					137.2	9.47 ± 0.30
^{197}Au	metal foil	100	50-160	8072.4	333.03	22.9 ± 0.95
					355.73	87.0 ± 3.0
					426.10	6.6 ± 0.3

Tab. 4.1: Specifications of targets and calibration targets used for the photoactivation experiments of isotopes in the rare-earth region. The abundance of the isotopes is denoted by N . m and S_n are target mass and neutron separation energy, respectively. The energies of the analysed γ transitions subsequent to the β decays of the reaction products are quoted by E_γ . The γ intensities per decay I_γ were taken from Ref. [58].

about 6.5 cm to the radiator. The irradiation was performed at various beam energies starting at $E_0 = 7450$ keV just above the neutron threshold of $^{148,150}\text{Nd}$. The energy was increased in steps of 150 and 200 keV up to $E_0 = 9800$ keV. Each activation run lasted between 6 and 24 h.

The absolute normalization of the photon flux was derived from the photon-scattering reaction of ^{11}B behind the collimator. In addition, gold and rhenium targets were simultaneously irradiated both in front of and behind the collimator to confirm the normalization by means of the standard reactions $^{187}\text{Re}(\gamma, n)$ and $^{197}\text{Au}(\gamma, n)$. The determination of the absolute normalization has been discussed in detail in Sec. 3.3.2.

After the irradiation, the activity of the reaction products was measured at the LEPS setup, which provides a high detection efficiency and sensitivity for low-energetic photons (see Sec. 3.2.1). Summing effects for the observed γ transitions have been carefully corrected as described in Sec. 3.2.4. In most cases, the corrections were found to be smaller than 10%. A list of the applied correction factors is shown in Tab. C.2 of the appendix. Nevertheless, the determined activity was confirmed for a few selected targets at the HPGe setup using a large distance of 81 mm between target and detector, where summing effects were almost negligible. The self-absorption of photons within the targets was accounted for by the analysis described in Sec. 3.2.3. For the very thin gadolinium and neodymium targets, a correction of less than 20% had to be applied. The relatively massive samarium targets, however, required a correction of up to a factor of 5 for the low-energetic γ transitions. Some correction factors are shown in Tab. C.1 of the appendix.

Additionally, in case of the decays of ^{147}Nd and ^{153}Sm , the activity was measured as a function of time to verify the half-lives quoted in the literature [58]. Exemplarily, this measurement is illustrated in Fig. 4.1 for the decay of ^{147}Nd . The determined half-lives of 10.88 ± 0.07 d and 45.98 ± 0.06 h for ^{147}Nd and ^{153}Sm , respectively, show some small deviations to the published values 10.98 ± 0.01 d and 46.50 ± 0.21 h.

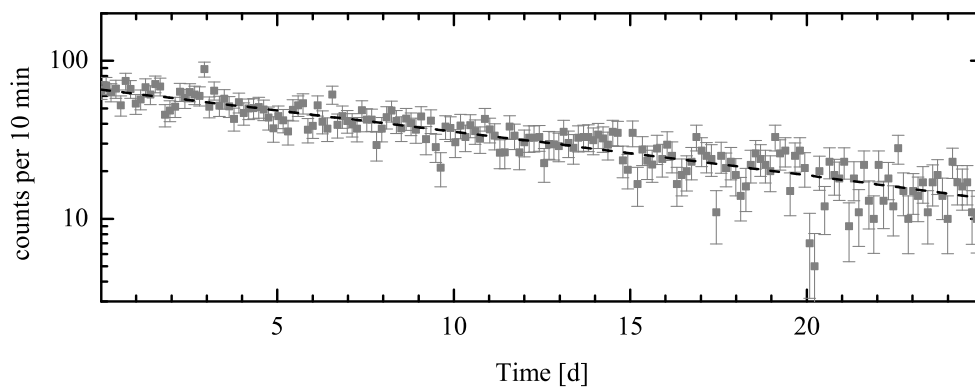


Fig. 4.1: Determination of the half-life of ^{147}Nd . The activity has been measured as a function of time and the half-life has been derived from an exponential fit (dashed line). For purposes of clarity, only every 20th data point has been plotted in the figure.

4.1.2 Results

The energy-integrated cross sections of the photoneutron reactions measured in the experiment have been compared to theoretical predictions calculated with the TALYS and the NON-SMOKER^{WEB} code, respectively, and averaged normalization factors $\langle f \rangle$ for the calculations have been determined as described in Sec. 3.1.1. Experimental data points stemming from irradiations with maximum photon energies E_{\max} as close as 300 keV to the neutron threshold have been omitted for the determination of $\langle f \rangle$ because these data points were subject to large uncertainties due to uncertainties of the absolute beam energy (see Sec. 3.4). The results for the various photoneutron reactions are illustrated in Fig. 4.2, Fig. 4.3 and Fig. 4.4 and summarized in Tab. 4.12 at the end of this chapter.

The error bars in the figures only refer to the statistical uncertainties of each measurement, whereas the gray error band denotes the overall uncertainty $\Delta_{\text{total}} \langle f \rangle$ for each averaged normalization factor and is derived from a Gaussian error propagation of all statistical and systematic uncertainties (see Sec. 3.5 for a detailed discussion about the experimental uncertainties).

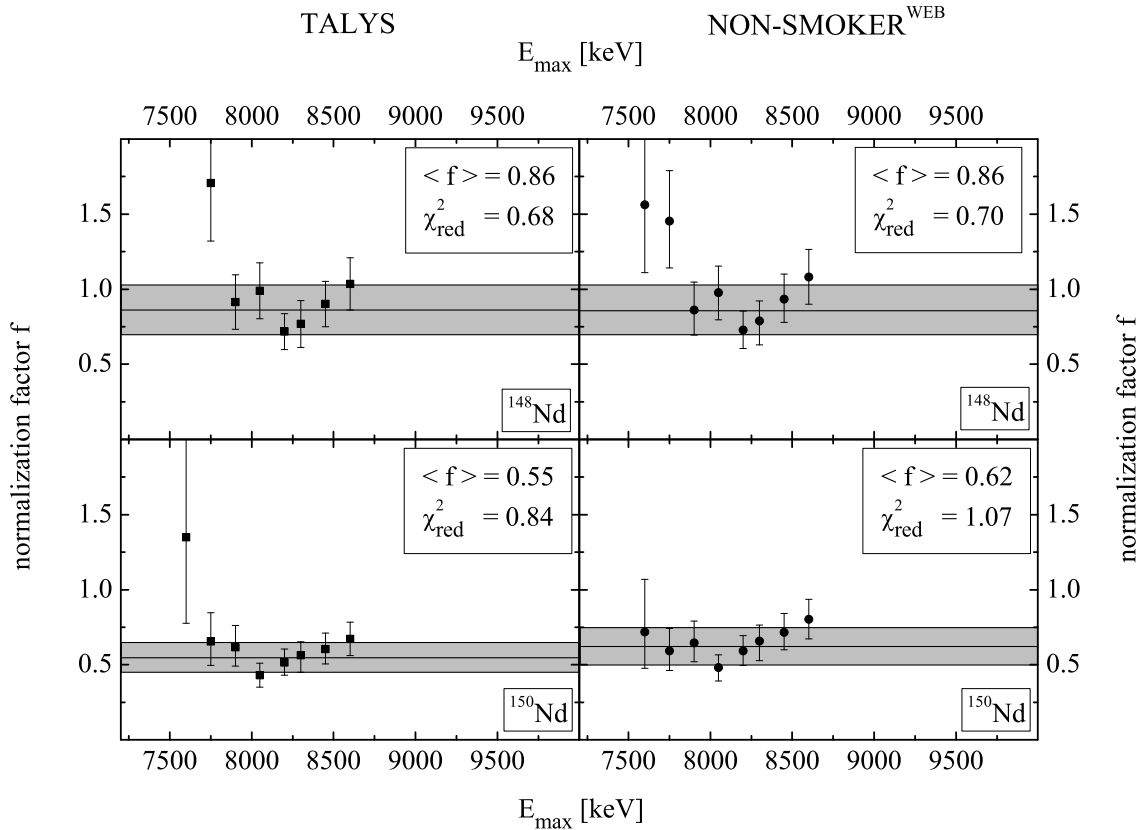


Fig. 4.2: Normalization factors f derived for two different theoretical predictions of the photoneutron cross section of $^{148,150}\text{Nd}$ at various photon energies E_{\max} .

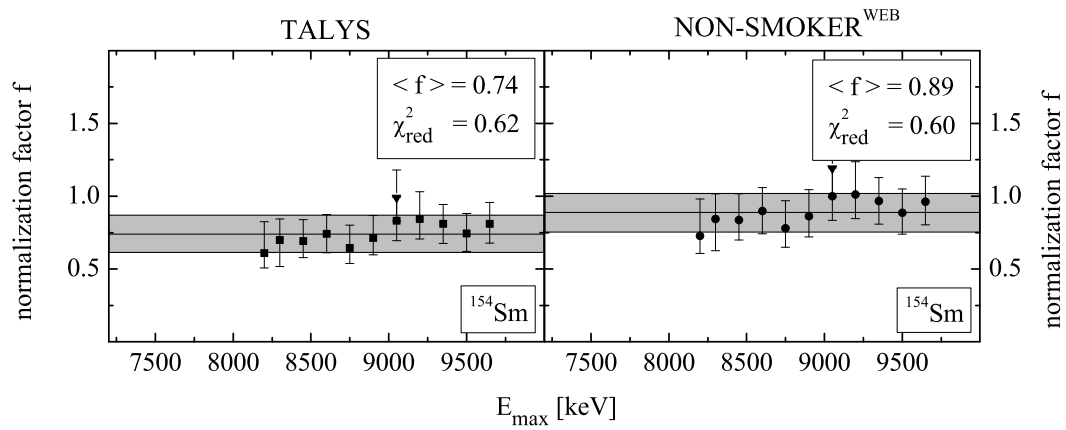


Fig. 4.3: Normalization factors f derived for two different theoretical predictions of the photoneutron cross section of ^{154}Sm at various photon energies E_{max} . The triangular data point at $E_{\text{max}} = 9050$ keV refers to an independent measurement to test the reproducibility of the experimental results.

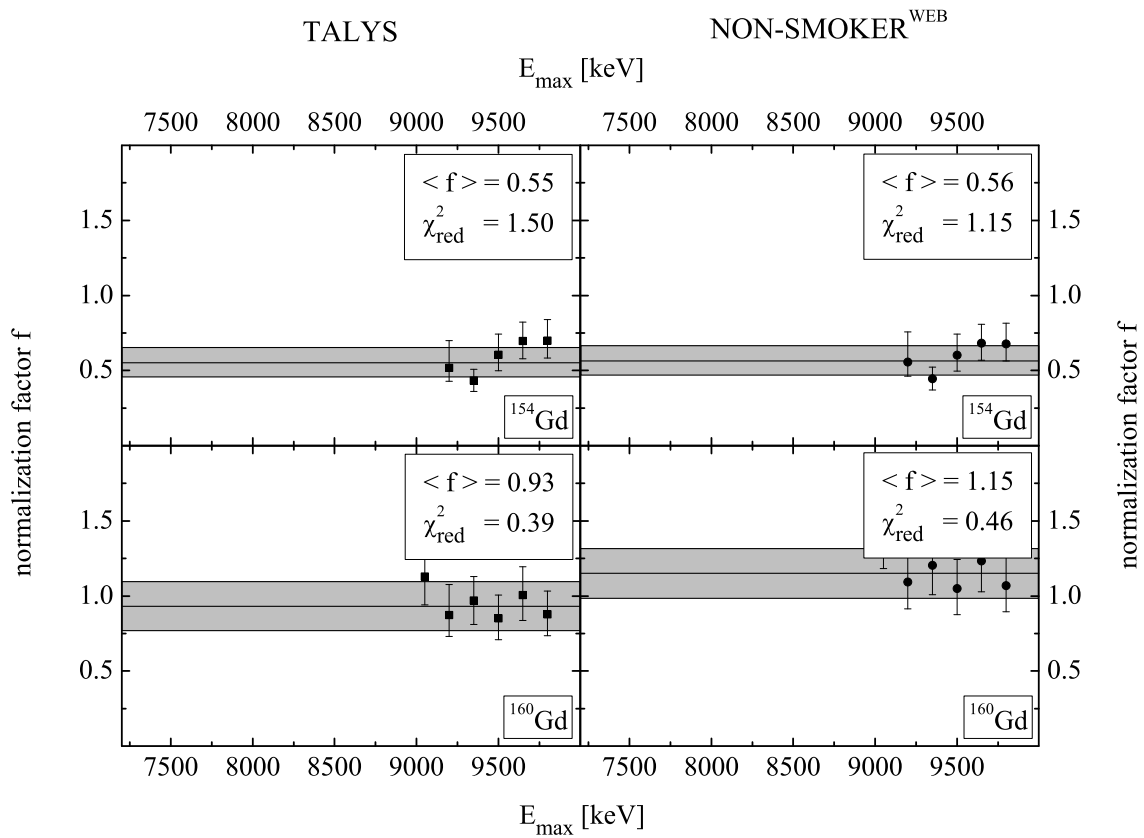


Fig. 4.4: Normalization factors f derived for two different theoretical predictions of the photoneutron cross section of $^{154,160}\text{Gd}$ at various photon energies E_{max} .

Both statistical model codes are in fair agreement with the experimental data points. A χ^2 test confirmed that the normalization factors f derived from irradiations of various maximum photon energies E_{\max} can be assumed to be independent of E_{\max} within the experimental uncertainties. With regard to the normalization factor derived for each isotope a mean deviation of 24% and 27% and a mean normalization factor of 0.82 and 0.73 has been found for the NON-SMOKER^{WEB} and for the TALYS calculation, respectively. One may conclude that the predictions slightly overestimate the photoneutron cross sections in the rare-earth region.

The results have also been compared to various experiments which investigated the photoneutron cross section in the energy region of the giant dipole resonance but also provided data for the low-energy tail down to the neutron separation energy. These data were obtained by using several experimental techniques like absorption and activation measurements using bremsstrahlung as well as direct measurements of the energy dependence of the photoneutron cross section using a quasimonoenergetic photon beam produced by the annihilation in flight of monoenergetic positrons. Details of these experiments are given in Refs. [59–64], and the results are shown in Fig. 4.5 in comparison with the two theoretical predictions which were normalized with the factors derived from the experiments of this thesis. For the isotopes ^{148}Nd , ^{154}Sm , and ^{160}Gd , the normalized calculations appear to be slightly below the experimental data points but are still fully consistent within the quoted uncertainties of the derived normalization factors. On the other hand, larger deviations have been found for ^{150}Nd and ^{154}Gd . For ^{150}Nd , a comparison close to the neutron emission threshold is not possible because no experimental data from previous works are available in this energy region. For ^{154}Gd , a non-negligible photoneutron cross section was even stated below the neutron separation energy of $S_n = 8894.8$ keV in Ref. [61]. This indicates systematic uncertainties of these experimental data and might explain the discrepancy to the normalized predictions of this thesis.

In addition to the determination of normalization factors, the astrophysically relevant ground-state reaction rates $\lambda^{\text{g.s.}}$ of $^{148,150}\text{Nd}$, ^{154}Gd , and ^{154}Sm have been derived for stellar temperatures between 2 and 3×10^9 K using the approximation of a thermal Planck spectrum as described in Sec. 3.1.2. For ^{160}Gd , too few data points were available in the relevant energy region, i. e., in the Gamow-like window, to perform an appropriate analysis. Since the experimental data points very close to the neutron emission threshold are subject to large uncertainties, they have been discarded for the analysis to increase the reliability of the experimental determination of the ground-state reaction rates. Consequently, the approximation of the Planck spectrum became less accurate. For comparison, the ground-state reaction rates were calculated according to Eq. (3.3) using the unnormalized theoretical predictions for the photoneutron cross sections. The results are shown in Tab. 4.2 and Tab. 4.3. The energy range between the neutron emission threshold and the upper energy limit quoted in the table has been estimated to contribute about 99% to the total ground-state reaction rate. $\Delta\lambda_{\text{Exp,Yield}}^{\text{g.s.}}$ and $\Delta\lambda_{\text{Exp,Approx}}^{\text{g.s.}}$ account for the uncertainty of the experimental reaction yield and of the approximation of the Planck spectrum within the Gamow-like window, respectively. Consistent with the normalization factors $\langle f \rangle$ found for the corresponding isotopes, the predictions slightly overestimate the ground-state reaction rates.

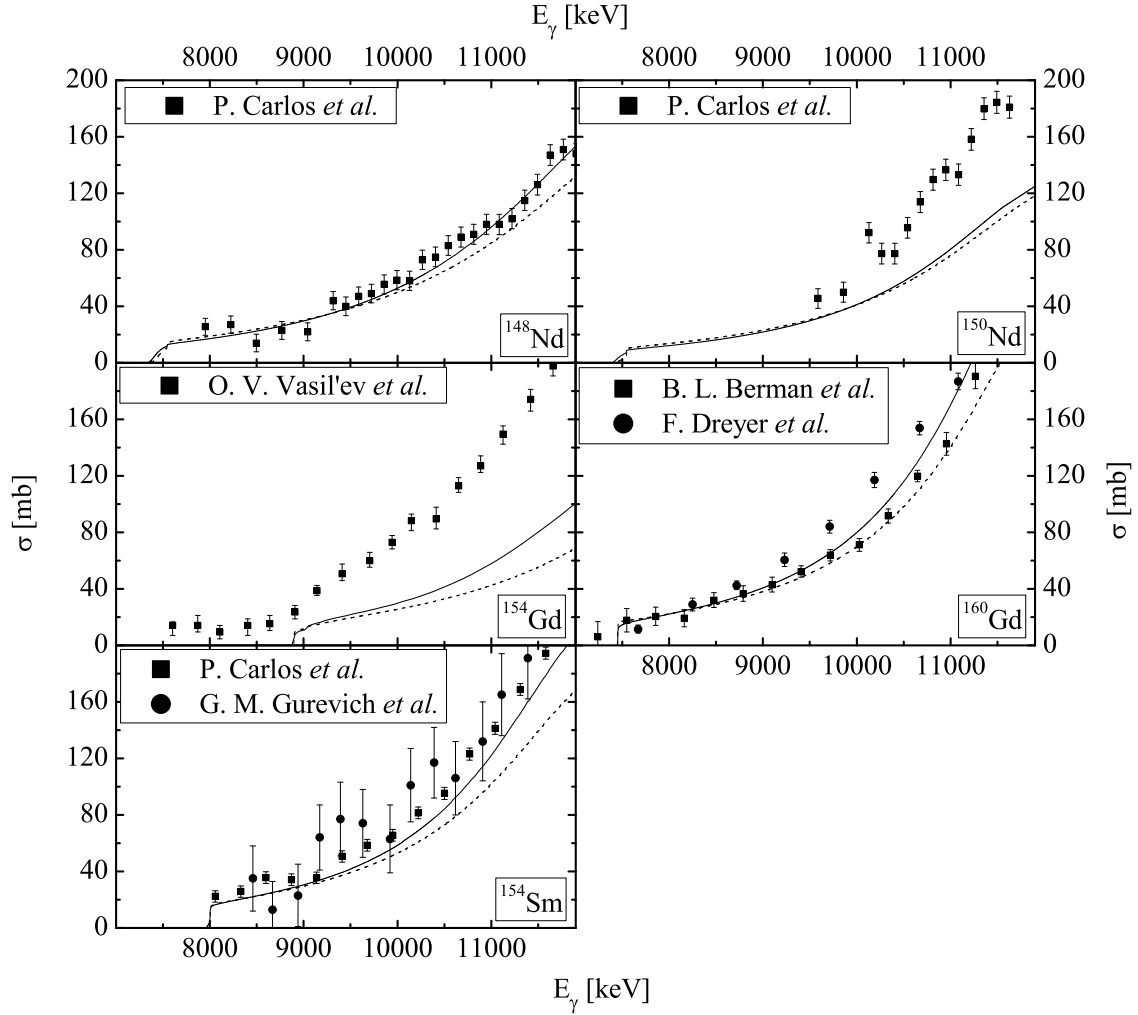


Fig. 4.5: Comparison of experimental data of the photoneutron cross section σ stemming from various experiments [59–64] and theoretical predictions using the TALYS (dashed line) and NON-SMOKER^{WEB} code (solid line), respectively. The theoretical calculations were normalized by the factors presented in Tab. 4.12. Note that the error bands of the theoretical predictions due to the experimental uncertainties of the applied normalization factors have been omitted in the graphs.

^{148}Nd			
Temperature [10^9 K]	2.0	2.5	3.0
Upper energy limit [keV]	8380	8655	8945
$\lambda_{\text{Exp}}^{\text{g.s.}}$	5.97×10^{-3}	6.45×10^1	2.92×10^4
$\Delta\lambda_{\text{Exp, Yield}}^{\text{g.s.}}$	1.10×10^{-3}	1.17×10^1	0.54×10^4
$\Delta\lambda_{\text{Exp, Approx}}^{\text{g.s.}}$	1.64×10^{-3}	1.39×10^1	0.99×10^4
$\lambda_{\text{TALYS}}^{\text{g.s.}}$	1.09×10^{-2}	8.19×10^1	3.31×10^4
$\lambda_{\text{N.S.}}^{\text{g.s.}}$	1.20×10^{-2}	8.62×10^1	3.39×10^4

^{150}Nd			
Temperature [10^9 K]	2.0	2.5	3.0
Upper energy limit [keV]	8440	8715	9010
$\lambda_{\text{Exp}}^{\text{g.s.}}$	3.52×10^{-3}	4.09×10^1	1.78×10^4
$\Delta\lambda_{\text{Exp, Yield}}^{\text{g.s.}}$	0.64×10^{-3}	0.74×10^1	0.33×10^4
$\Delta\lambda_{\text{Exp, Approx}}^{\text{g.s.}}$	0.85×10^{-3}	0.99×10^1	0.67×10^4
$\lambda_{\text{TALYS}}^{\text{g.s.}}$	9.10×10^{-3}	7.74×10^1	3.25×10^4
$\lambda_{\text{N.S.}}^{\text{g.s.}}$	9.44×10^{-3}	7.16×10^1	2.91×10^4

^{154}Sm			
Temperature [10^9 K]	2.0	2.5	3.0
Upper energy limit [keV]	8930	9205	9505
$\lambda_{\text{Exp}}^{\text{g.s.}}$	4.78×10^{-4}	7.45×10^0	5.04×10^3
$\Delta\lambda_{\text{Exp, Yield}}^{\text{g.s.}}$	0.85×10^{-4}	1.32×10^0	0.88×10^3
$\Delta\lambda_{\text{Exp, Approx}}^{\text{g.s.}}$	0.54×10^{-4}	0.46×10^0	0.28×10^3
$\lambda_{\text{TALYS}}^{\text{g.s.}}$	7.87×10^{-4}	1.11×10^1	6.79×10^3
$\lambda_{\text{N.S.}}^{\text{g.s.}}$	6.53×10^{-4}	9.21×10^0	5.65×10^3

Tab. 4.2: Astrophysical ground-state reaction rates of $^{148,150}\text{Nd}$ and ^{154}Sm determined experimentally by the approximation approach of a thermal Planck spectrum at three different temperatures are compared with theoretical predictions of two statistical model codes. The notation is described in Sec. 4.1.2.

¹⁵⁴ Gd			
Temperature [10 ⁹ K]	2.0	2.5	3.0
Upper energy limit [keV]	9850	10120	10400
$\lambda_{\text{Exp}}^{\text{g.s.}}$	2.74×10^{-6}	1.12×10^{-1}	1.49×10^2
$\Delta\lambda_{\text{Exp,Yield}}^{\text{g.s.}}$	0.50×10^{-6}	0.21×10^{-1}	0.29×10^2
$\Delta\lambda_{\text{Exp,Approx}}^{\text{g.s.}}$	0.48×10^{-6}	0.34×10^{-1}	0.52×10^2
$\lambda_{\text{TALYS}}^{\text{g.s.}}$	5.10×10^{-6}	2.07×10^{-1}	2.58×10^2
$\lambda_{\text{N.S.}}^{\text{g.s.}}$	5.01×10^{-6}	2.06×10^{-1}	2.58×10^2

Tab. 4.3: Astrophysical ground-state reaction rates of ¹⁵⁴Gd determined experimentally by the approximation approach of a thermal Planck spectrum at three different temperatures are compared with theoretical predictions of two statistical model codes. The notation is described in Sec. 4.1.2.

4.2 Photoneutron reactions near the neutron-shell closure

The experimental results of the preceding section have confirmed the predictive power of two statistical model calculations for photoneutron cross sections of several isotopes in the rare-earth region. To extend the data set for this mass region, the photoneutron reactions of ^{140,142}Ce have been investigated in an independent photoactivation experiment. These isotopes are near or even at the $N=82$ neutron-shell closure, where some of the assumptions involved in statistical model calculations, e. g., a sufficiently high level density for a statistical treatment, are often not entirely fulfilled. Therefore, it is interesting to investigate if any significant deviations between experiment and theory can be observed when approaching the neutron magic number.

4.2.1 Experiment and data analysis

In this experiment, several naturally composed cerium targets (disks of 20 mm diameter) were irradiated in front of the collimator using maximum photon energies between $E_{\text{max}} = 8250$ keV and 9900 keV (see Tab. 4.4). The duration of each activation run was between 12 and 24 h for each set of targets. Compared to the other photoactivation experiments discussed in this thesis, the distance between radiator and target position was increased to about 19 cm due to slight modifications on the beam line and radiator setup. It was found that this has reduced the photon flux by almost a factor of 6. Nevertheless, the obtained reaction yields were fully sufficient for a proper analysis, and statistical uncertainties were still far below the systematic ones.

The photon-flux normalization was performed by means of the two standard targets gold and rhenium measured simultaneously at the target position of the cerium targets in front of the

Isotope	Form	N [%]	m [mg]	S_n [keV]	E_γ [keV]	I_γ [%]
^{140}Ce	CeO_2	88.48	~ 800	9202	165.858	79.9 ± 0.5
^{142}Ce	CeO_2	11.08	~ 800	7169.1	145.443	48.29 ± 0.2

Tab. 4.4: Specifications of cerium targets used for the photoactivation experiments. For details about the calibration targets gold and rhenium and for the notations used in the table, see Tab. 4.1.

collimator. In this experiment, no normalization of the photon flux behind the collimator was determined.

After the irradiation, the activity of each target was measured at the HPGe setup using a distance of 42 mm between target and detector. This distance proved to be a good compromise with regard to detection efficiency and summing effects, which could be neglected in the analysis. Corrections due to self-absorption were determined to be less than 10% as seen from Tab. C.1 of the appendix.

Finally, the energy-integrated cross section of the photoneutron reactions of $^{140,142}\text{Ce}$ were derived from the activity of the reaction products as described in Sec. 3.2.

4.2.2 Results

The experimental data have been compared to statistical model calculations using the TALYS and NON-SMOKER^{WEB} code. The results for the determined normalization factors are illustrated in Fig. 4.6 and summarized in Tab. 4.12 at the end of this chapter.

In case of ^{140}Ce , averaged normalization factors of 1.29 and 1.65 for the TALYS and NON-SMOKER^{WEB} code, respectively, have been determined showing that the theoretical predictions seem to underestimate the photoneutron cross section in the energy region close to the neutron threshold. Note that the photoneutron cross section of ^{140}Ce has already been investigated to some extent in the analysis described in Sec. 3.4.3. This analysis has indicated an even larger normalization factor of 2.2 for the TALYS calculation. The discrepancy between the independently derived normalization factors might be explained by the fact that the analysis of Sec. 3.4.3 is very sensitive to the photoneutron cross section just a few keV above the threshold, whereas the result presented in this section has been determined by averaging the cross section over a wide energy range of several hundred keV. In other words, if the energy dependence of the cross section is not exactly described by theory, this might have a significant influence on the obtained results.

Nevertheless, one can also not fully exclude that the discrepancy stems from experimental errors. Unfortunately, due to the rather high neutron separation energy of $S_n = 9202$ keV only three data points have been obtained for the photoneutron reaction of ^{140}Ce . As shown in Fig. 4.6, these data points exhibit strong fluctuations, which is expressed by the large value

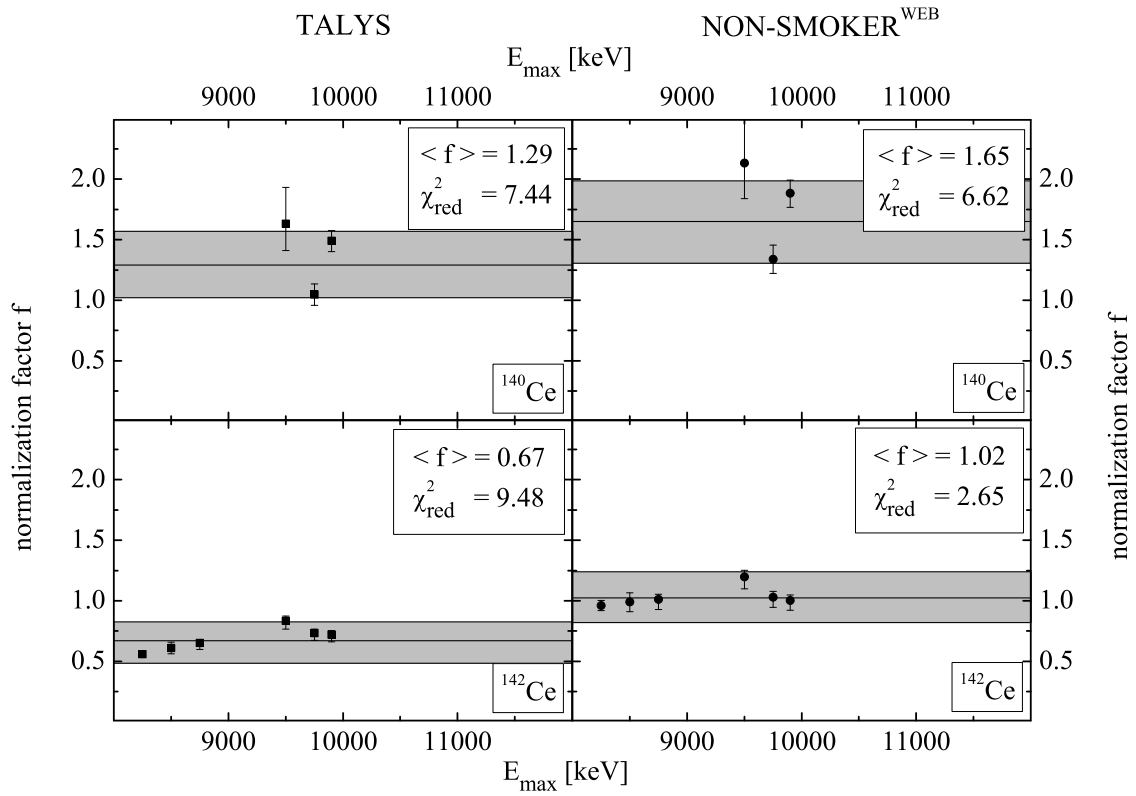


Fig. 4.6: Normalization factors f derived for two different theoretical predictions of the photoneutron cross section of $^{140,142}\text{Ce}$ at various energies E_{max} .

obtained from a χ^2 test. This calls for further systematic investigations of this reaction in the future.

For the photoneutron cross section of ^{142}Ce , an excellent agreement with the prediction using the NON-SMOKER^{WEB} code was found, whereas the TALYS code overestimates the cross section. Similar to the analysis of ^{140}Ce , a rather large value was determined for χ^2_{red} due to discrepancies between the experimental data points. For example, a much lower value of χ^2_{red} will be obtained if the data point at $E_{\text{max}} = 9500$ keV is discarded. Although one cannot entirely exclude that the discrepancies arise from uncertainties of the involved theoretical predictions, they rather have to be ascribed to experimental errors.

Finally, the normalized theoretical predictions have been compared to experimental data of previous experiments which have measured the photoneutron reactions by means of the positron annihilation in flight technique [65]. The results are shown in Fig. 4.7.

In case of ^{140}Ce , some larger discrepancies between the experimental data and the normalized calculations can be seen for energies close to the threshold. It has to be pointed out that the experimental data of Ref. [65] quote some non-negligible cross section even below the neu-

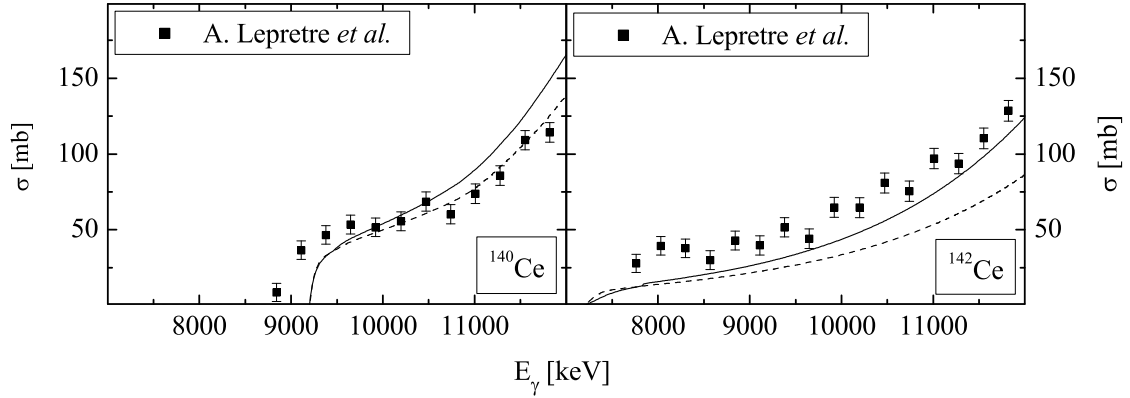


Fig. 4.7: Comparison of experimental data of the photoneutron cross section σ of $^{140,142}\text{Ce}$ stemming from measurements using the positron annihilation in flight technique [65] and theoretical predictions using the TALYS (dashed line) and NON-SMOKER^{WEB} code (solid line), respectively. The theoretical calculations were normalized by the factors presented in Tab. 4.12. Note that the error bands of the theoretical predictions due to the experimental uncertainties of the applied normalization factors have been omitted in the graphs.

tron separation energy of $S_n = 9202.1$ keV. This indicates some systematic experimental errors. Therefore, the data points close to the threshold should be treated under reserve. At larger energies, however, the normalized prediction using the TALYS code is in very good agreement with the data points, whereas the cross section is still overestimated by the normalized NON-SMOKER^{WEB} calculation. In case of ^{142}Ce , both normalized theoretical predictions are systematically below the data points, although the energy dependence of the cross section is rather well described.

In conclusion, the investigation of $^{140,142}\text{Ce}$ has confirmed the applicability of statistical model codes even for isotopes near and at the neutron-shell closure. The determined normalization factors of up to 1.65 are still consistent with the expected uncertainties of these theoretical calculations. However, the experimental data showed some strong fluctuations, and the derived normalization factors from this photoactivation experiment should be verified in future investigations.

4.3 The photoneutron reaction of ^{192}Os

Among the photoneutron reactions studied in this thesis, the reaction $^{192}\text{Os}(\gamma, n)$ exhibits the peculiarity that the first excited state of the reaction product ^{191}Os is an isomeric state with a half-life of 13.1 h, which is long enough to be observed in the experiment. This allows to distinguish between reaction channels of the photoneutron reaction populating the ground state

and the isomeric state, respectively. Hence, this photoneutron reaction provides an additional test for the predictions of statistical model codes.

To estimate the contribution of each reaction channel, one needs to take a closer look at the quantum numbers of the states involved in the reaction. In general, the dominating channels of a photoneutron reaction are those where the parent nucleus is excited by an E1 transition and then decays by the emission of an s -wave neutron. Magnetic excitations, e. g., M1 transitions, or electric excitations of higher multipolarity, e. g., E2 transitions, are usually suppressed by several orders of magnitude, whereas the angular momentum barrier hampers the emission of neutrons of larger angular momentum, e. g., via a p or d wave.

In case of the photoneutron reaction of ^{192}Os , which has a ground state of spin and parity $J^\pi = 0^+$, it follows that mainly states of ^{191}Os with $J^\pi = \frac{1}{2}^-$ and $J^\pi = \frac{3}{2}^-$ will be populated. Other states can only be accessed by magnetic excitations or electric excitations of higher multipolarity or by the emission of neutrons of larger angular momentum. This is outlined in Tab. 4.5. With regard to the level scheme of ^{191}Os illustrated in Fig. 4.8, one can conclude that a direct population of the ground state of ^{191}Os having spin and parity $J^\pi = \frac{9}{2}^-$ is highly suppressed, whereas the first excited state of $J^\pi = \frac{3}{2}^-$ can be easily accessed.

		Neutron emission		
		s wave: $\frac{1}{2}^+ \otimes 0^+$	p wave: $\frac{1}{2}^+ \otimes 1^-$	d wave: $\frac{1}{2}^+ \otimes 2^+$
Excitation	E1: $0^+ \otimes 1^-$	$\frac{1}{2}^-, \frac{3}{2}^-$	$\frac{1}{2}^+, \frac{3}{2}^+, \frac{5}{2}^+$	$\frac{1}{2}^-, \frac{3}{2}^-, \frac{5}{2}^-, \frac{7}{2}^-$
	M1: $0^+ \otimes 1^+$	$\frac{1}{2}^+, \frac{3}{2}^+$	$\frac{1}{2}^-, \frac{3}{2}^-, \frac{5}{2}^-$	$\frac{1}{2}^+, \frac{3}{2}^+, \frac{5}{2}^+, \frac{7}{2}^+$
	E2: $0^+ \otimes 2^+$	$\frac{3}{2}^+, \frac{5}{2}^+$	$\frac{1}{2}^-, \frac{3}{2}^-, \frac{5}{2}^-, \frac{7}{2}^-$	$\frac{1}{2}^+, \frac{3}{2}^+, \frac{5}{2}^+, \frac{7}{2}^+, \frac{9}{2}^+$

Tab. 4.5: Accessible states of ^{191}Os in the photoneutron reaction $^{192}\text{Os}(\gamma, n)$ with regard to the conservation of spin and parity

For a quantitative investigation, the intensity of each individual reaction channel has been calculated by means of the TALYS code as a function of incident photon energy. To compare with photoactivation experiments, the theoretical prediction has been weighted with the spectral distribution of bremsstrahlung. The results are shown in Fig. 4.8. As expected, the direct population of the ground state is negligible, whereas the isomeric state is highly populated. Anyhow, one should be aware of the fact that excited states of higher energy will decay either to the ground state or to the isomeric state via electromagnetic transitions on a very short time scale. Hence, if theoretical predictions shall be compared to experimental data stemming from photoactivation experiments, one needs to quantitatively treat this de-excitation to determine the final ratio between the population of ground state and isomeric state. Unfortunately, it was found that the TALYS code was not capable of reliably treating this de-excitation and, thus, no quantitative prediction could be obtained.

Anyway, with some simple considerations, one can already provide a rough estimation for the final population. Since the de-excitation will be dominated by transitions of low multipolarity,

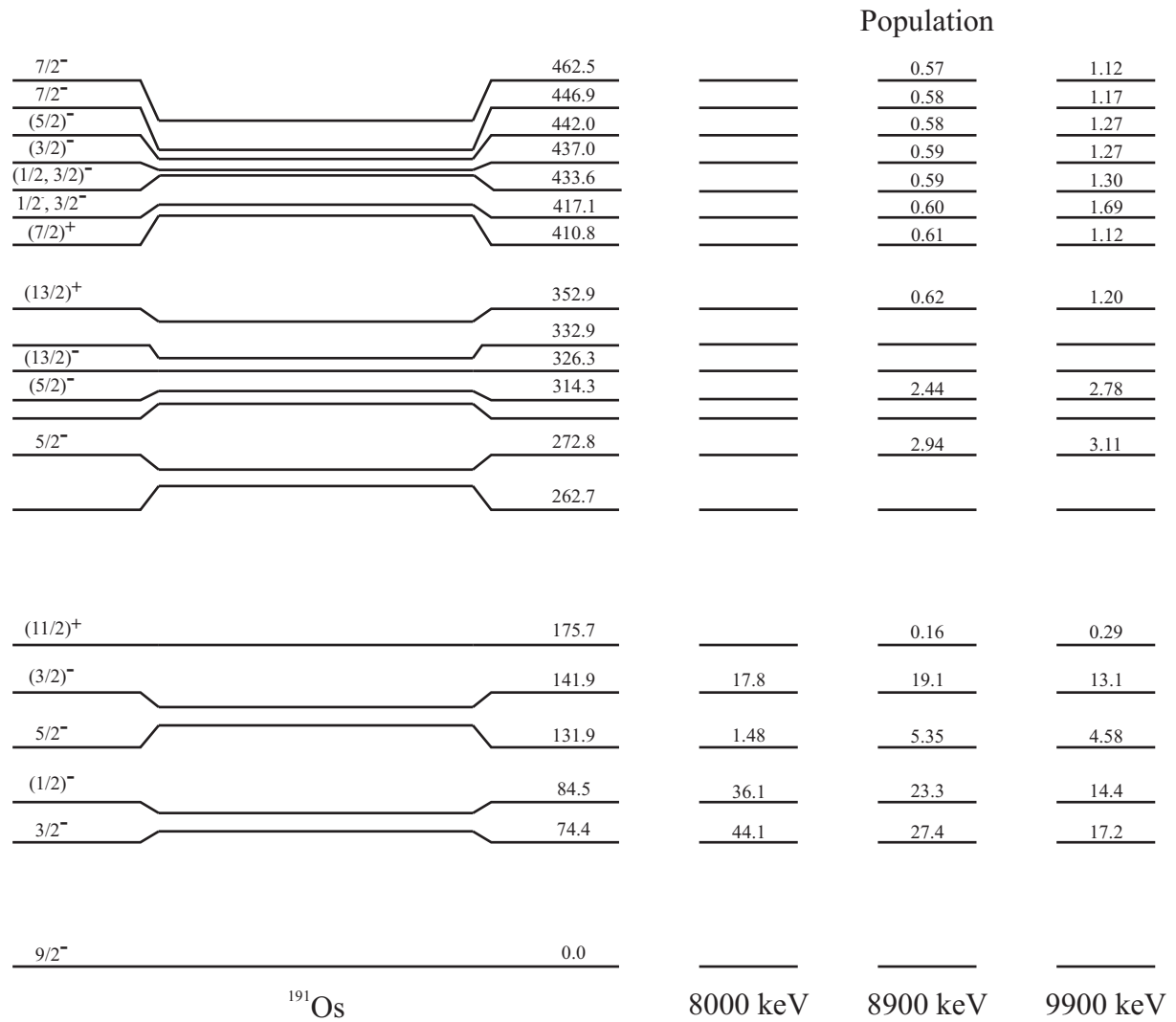


Fig. 4.8: Level scheme of ^{191}Os up to energies of 470 keV obtained from Ref. [58]. For some of the states no data for spin and parity was available. The population probability (in %) of the levels in ^{191}Os of the reaction $^{192}\text{Os}(\gamma, n)$ has been predicted by the TALYS code for incident photons following a bremsstrahlung distribution of energies $E_{\text{max}} = 8000$ keV, 8900 keV, and 9900 keV, respectively. Probabilities of less than 0.1% have been omitted in the figure. See text for more details.

one can assume that only states of spin $J \geq \frac{5}{2}$ will decay with a non-negligible branching to the ground state, whereas states of lower spin will favor the decay to the isomeric state. Under this assumption, only the state at $E_x = 131.9$ keV can significantly populate the ground state if bremsstrahlung of maximum photon energy $E_{\text{max}} = 8000$ keV is used for the irradiation (see Fig. 4.8). Since the predicted population of this state is only 1.48%, the final population of the ground state can be expected to be of the order of 1% or less.

With increasing photon energy, the direct population of lower-energetic states decreases, whereas

the population of higher-energetic states increases. Hence, the number of possible transitions to the ground state will increase, in particular those exhibiting multi-step de-excitations. Therefore, one can also expect an increase of the ground-state population. For example, at a maximum photon energy of $E_{\text{max}} = 9900$ keV the summed population of all states of spin $J \geq \frac{5}{2}$ up to an energy of 470 keV already exhibits about 17%. A detailed calculation of the final population of the ground state has to involve all branching ratios for the de-excitation of each excited state. Such an analysis, however, goes beyond the scope of this thesis.

In conclusion, one expects to find a very low final population of the ground state of the order of 1% or less in photoactivation experiments for irradiations of rather low photon energy and, presumably, a larger population at higher photon energies. Indeed, this has been confirmed by the experiment discussed in the next section.

4.3.1 Experiment and data analysis

The reaction $^{192}\text{Os}(\gamma, n)$ was investigated in two different experiments. In a first experiment, the irradiation of ^{192}Os was performed together with the investigation of the rare-earth isotopes discussed in Sec. 4.1. The targets used in this experiment were prepared from naturally composed OsO_2 powder which was pressed to thin disks of 20 mm diameter. The target specifications are summarized in Tab. 4.6.

After the irradiation, the activity of the irradiated targets was measured at the LEPS setup. In spite of the high detection efficiency, no correction for summing effects had to be applied in case of the decay of ^{191}Os , but the self-absorption in the massive targets required a correction by up to a factor of 2 (see Tab. C.1 of the appendix). Moreover, due to the population of the isomeric state of ^{191}Os in the photoneutron reaction, a more sophisticated analysis of the experimental data than described in Sec. 3.2 was necessary. As discussed further below, it was found that this data analysis has to involve the time dependence of the target activity, which had not been measured in this experiment.

For this reason, a second photoactivation experiment of ^{192}Os was carried out where the photo-disintegration was measured with bremsstrahlung of maximum photon energy $E_{\text{max}} = 8250$ keV, 8900 keV, 9350 keV and 9900 keV, respectively. The activity of the reaction product was recorded as a function of time for a period of several days after the irradiation. In this second experiment, only the time dependence of the activity was studied and no photon-flux calibration had to be performed.

In this section, it will be briefly outlined how one can extract the population of ground state and isomeric state from the time dependence of the target activity. Since a detailed description of this analysis is presented in Ref. [66], only the basic ideas will be provided.

In the following, N_{gs} and N_{m} denote the number of ^{191}Os nuclei in the ground state and in the isomeric state, respectively. The ground state decays to ^{191}Ir with a half-life of $T_{1/2}(\beta) = 15.4$ d. The β decay of the isomeric state would require a first-forbidden transition and, hence, is

Isotope	Form	N [%]	m [mg]	S_n [keV]	E_γ [keV]	I_γ [%]
^{192}Os	OsO_2	41.0	400 - 550	7558.09	129.431	26.50 ± 0.04

Tab. 4.6: Specifications of osmium targets used for the photoactivation experiments. These targets were used in two independent photoactivation experiments as discussed in the text. The notation used in the table is described in Tab. 4.1.

highly suppressed compared to the internal transition with $T_{1/2}(\text{IT}) = 13.1$ h feeding the ground state. During the photoactivation experiment, the ground state and isomeric state of ^{191}Os are populated with a certain rate λ_{gs} and λ_{m} , respectively. These quantities shall already include the subsequent de-excitation of excited states in the reaction product ^{191}Os and refer to the final population of the ground state and isomeric state, respectively (For clarification: λ_{gs} should not be confused with the astrophysically relevant ground-state reaction rate, which is denoted by $\lambda^{\text{g.s.}}$ in this thesis). With regard to this notation, the time evolution of N_{gs} and N_{m} is given by a set of coupled differential equations:

$$\frac{dN_{\text{gs}}}{dt} = \lambda_{\text{IT}}N_{\text{m}}(t) - \lambda_{\beta}N_{\text{gs}}(t) + \lambda_{\text{gs}}\Phi(t) \quad (4.1)$$

$$\frac{dN_{\text{m}}}{dt} = -\lambda_{\text{IT}}N_{\text{m}}(t) + \lambda_{\text{m}}\Phi(t) \quad . \quad (4.2)$$

The decay constants λ_{β} and λ_{IT} refer to the β decay of the ground state and the internal transition of the isomeric state, respectively. $\Phi(t)$ accounts for the time dependence of the photon-flux intensity during the irradiation and is known from experiment. The differential equations also hold for the time after irradiation when $\Phi(t) = 0$. Thus, one can solve the differential equations using λ_{gs} and λ_{m} as free parameters and obtains the solutions for the number of nuclei in the ground state and isomeric state as a function of time, i. e., $N_{\text{gs}}(t, \lambda_{\text{gs}}, \lambda_{\text{m}})$ and $N_{\text{m}}(t, \lambda_{\text{m}})$.

The rates λ_{gs} and λ_{m} can then be determined if N_{gs} and N_{m} are each measured for a certain point of time after the irradiation. Due to its very small γ intensity, however, the internal transition of the isomeric state cannot be detected using HPGe detectors and, therefore, N_{m} cannot be determined directly. But it is possible to measure N_{gs} as a function of time by observing the γ transitions subsequent to the β decay of the ground state to ^{191}Ir . The reaction rates λ_{gs} and λ_{m} can then be obtained from a fit of $N_{\text{gs}}(t_{\text{act}}, \lambda_{\text{gs}}, \lambda_{\text{m}})$ to the measured decay curve.

This data analysis has been applied to the time dependence of the target activity measured in the second photoactivation experiment described above. Since no photon-flux normalization was performed in this experiment, it was not possible to determine the absolute rates λ_{gs} and λ_{m} , but the measurement was sufficient to yield the ratio of both quantities. The data analysis and the obtained results are illustrated in Fig. 4.9.

The ratio $\lambda_{\text{gs}}/\lambda_{\text{m}}$ is small being less than 3% at $E_{\text{max}} = 8250$ keV indicating that the ground state of ^{191}Os is only scarcely populated in the photoneutron reaction of ^{192}Os . However, the ratio

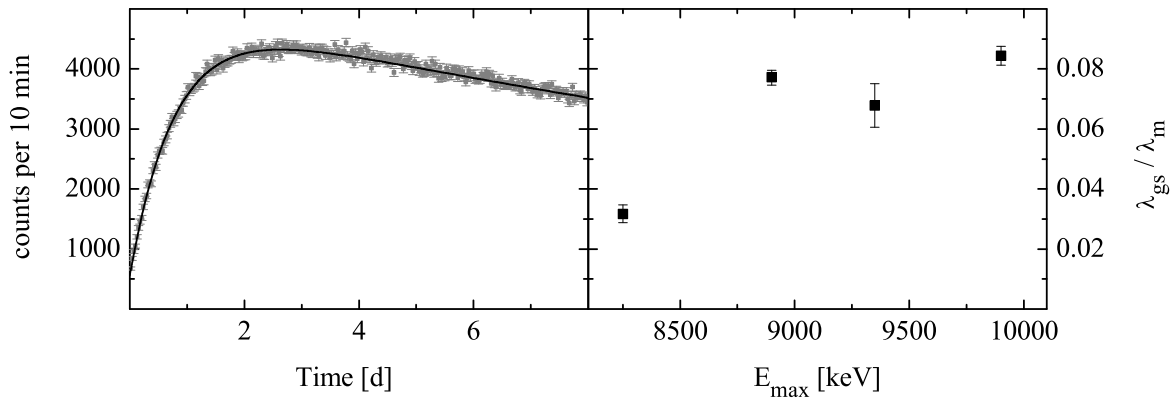


Fig. 4.9: Ratio of population of the ground state and isomeric state of ^{191}Os after the photoneutron reaction $^{192}\text{Os}(\gamma, n)$. *Left panel:* The activity of a target irradiated with bremsstrahlung of maximum photon energy $E_{\text{max}} = 8900$ keV has been measured as a function of time by observing the γ transition of energy $E_{\gamma} = 129.431$ keV subsequent to the β decay of ^{191}Os to ^{191}Ir (gray data points). The photoneutron reaction rates λ_{gs} and λ_{m} to the ground state and the isomeric state of ^{191}Os , respectively, can be derived from a fit of the solutions of Eq. (4.1) and Eq. (4.2) (solid line). See text for more details. *Right panel:* The ratio of population $\lambda_{\text{gs}}/\lambda_{\text{m}}$ has been determined for irradiations of four different energies E_{max} .

increases with incident photon energies up to about 8% at $E_{\text{max}} = 9900$ keV. Such a dependence has indeed been expected with regard to the discussion made in the preceding section. The experimental uncertainty of this analysis has been estimated to be less than 10% [66].

The determined ratios $\lambda_{\text{gs}}/\lambda_{\text{m}}$ have then been adopted for the data analysis of the first photoactivation experiment where N_{gs} has been measured for one single point of time only. Note that in this experiment a normalization of the photon flux has been performed. Therefore, the absolute rates λ_{gs} and λ_{m} could be derived from the well-known time dependence of N_{gs} and from the ratio $\lambda_{\text{gs}}/\lambda_{\text{m}}$. This analysis is described in more detail in Ref. [66].

For the sake of completeness, it shall be mentioned that the measured time dependence of the activity of ^{191}Os for times much larger than $T_{1/2}(\text{IT})$ also yielded the half-life of the β decay of ^{191}Os . The determined value of $T_{1/2}(\beta) = 15.02 \pm 0.28$ d was found to be in fair agreement with the published value of $T_{1/2}(\beta) = 15.4 \pm 0.1$ d [58].

4.3.2 Results

As mentioned above, both statistical model codes were not capable to reliably treat the de-excitation of ^{191}Os after the photoneutron reaction of ^{192}Os and, thus, could not provide the final population of ground state and isomeric state in this reaction product. Hence, the experimental data could only be compared with predictions for the total photoneutron cross section which

refers to the sum of λ_{gs} and λ_{m} . The results are shown in Fig. 4.10 and summarized in Tab. 4.12 at the end of this chapter. The theoretical predictions are in excellent agreement with the experimental data within the experimental error bars. Whereas the TALYS code slightly overestimates the cross section by about 20%, the normalization factor for the NON-SMOKER^{WEB} calculation is almost unity. With regard to the large uncertainties stemming from the uncertainties of the absolute beam energy (see Sec. 3.4), the first data point above the neutron threshold has been omitted for the determination of the averaged normalization factor $\langle f \rangle$.

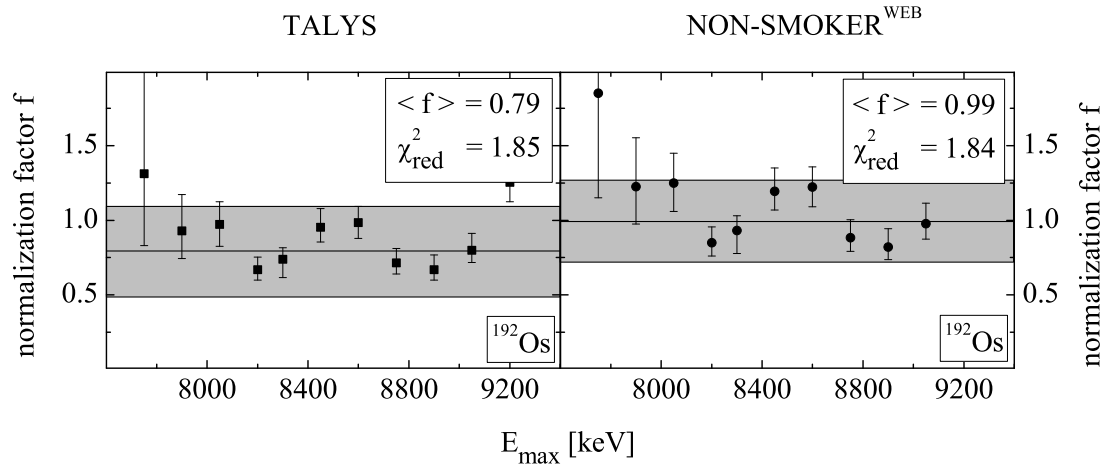


Fig. 4.10: Normalization factors f derived for two different theoretical predictions of the photoneutron cross section of ^{192}Os at various energies E_{max} .

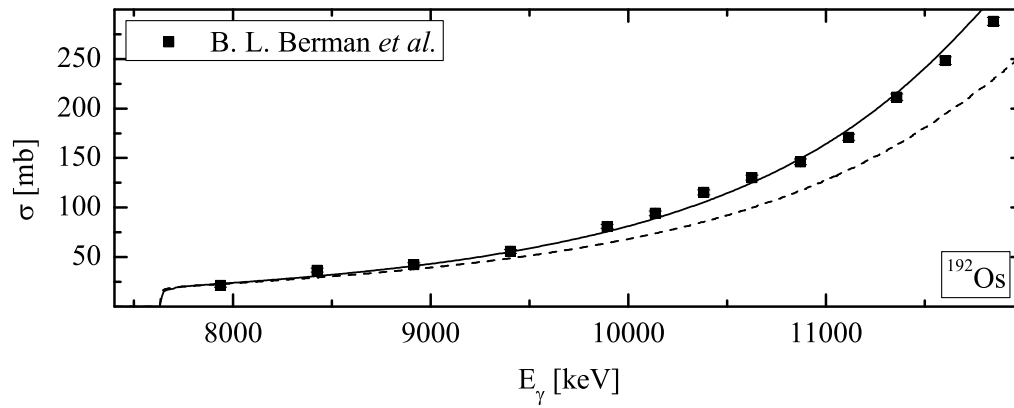


Fig. 4.11: The photoneutron cross section σ of ^{192}Os derived from an experiment using quasimonoenergetic photons [67] is compared with two theoretical predictions using the TALYS code (dashed line) and the NON-SMOKER^{WEB} code (solid line), respectively. Both calculations have been normalized by the factors presented in Tab. 4.12. The error bands of the calculations due to the uncertainties of the applied normalization factors have been omitted in the graph.

Furthermore, the results have been compared to experimental data stemming from a direct measurement of the photoneutron cross section with quasimonoenergetic photons produced by the positron annihilation in flight technique [67] (see Fig. 4.11). Whereas the normalized NON-SMOKER^{WEB} calculation is in very good agreement with the data of this experiment, the normalized TALYS calculation shows some larger discrepancies at energies above 9000 keV.

Finally, the experimental data obtained from the photoactivation experiments of this thesis have been used to calculate the ground-state reaction rates via an approximation of a Planck spectrum as described in Sec. 3.1.2. The results are summarized in Tab. 4.7. In accordance with the normalization factors derived for the predictions of the photoneutron cross section, the calculations very well agree with the experimental data within the quoted uncertainties.

^{192}Os			
Temperature [10^9 K]	2.0	2.5	3.0
Upper energy limit [keV]	8560	8830	9130
$\lambda_{\text{Exp}}^{\text{g.s.}}$	5.11×10^{-3}	5.10×10^1	2.47×10^4
$\Delta\lambda_{\text{Exp,Yield}}^{\text{g.s.}}$	1.03×10^{-3}	1.03×10^1	0.50×10^4
$\Delta\lambda_{\text{Exp,Approx}}^{\text{g.s.}}$	0.57×10^{-3}	0.25×10^1	0.16×10^4
$\lambda_{\text{TALYS}}^{\text{g.s.}}$	6.24×10^{-3}	5.75×10^1	2.65×10^4
$\lambda_{\text{N.S.}}^{\text{g.s.}}$	4.88×10^{-3}	4.55×10^1	2.12×10^4

Tab. 4.7: Astrophysical ground-state reaction rates of ^{192}Os determined experimentally by the approximation approach of a thermal Planck spectrum at three different temperatures are compared with theoretical predictions of two statistical model codes. The notation is described in Sec. 4.1.2.

4.4 The photoneutron reactions of $^{191,193}\text{Ir}$

4.4.1 Experiment and data analysis

The photoneutron reactions of $^{191,193}\text{Ir}$ were measured in a photoactivation experiment using bremsstrahlung at seven different energies ranging from $E_{\text{max}} = 7875$ keV just above the neutron separation energy of ^{193}Ir up to 9900 keV. Naturally composed iridium targets (disks of 20 mm diameter) were mounted in front of the collimator at a distance of about 6.5 cm to the radiator and were irradiated for a duration of 12 to 24 h each. The target specifications are shown in Tab. 4.8. For the absolute normalization of the photon flux, the two standard targets gold and rhenium were measured simultaneously at the target position in front of the collimator. No normalization of the photon flux was performed behind the collimator in this experiment.

Isotope	Form	N [%]	m [mg]	S_n [keV]	E_γ [keV]	I_γ [%]
^{191}Ir	metal foil	37.3	330	8026.5	186.68	52.44 ± 2.052
					518.55	33.972 ± 1.114
					557.95	30.096 ± 0.912
					569.30	28.50 ± 0.912
^{193}Ir	metal foil	62.7	330	7771.85	295.957	28.72 ± 0.14
					308.455	29.68 ± 0.15
					316.506	82.71 ± 0.21
					468.069	47.81 ± 0.24
					612.462	5.34 ± 0.08

Tab. 4.8: Specifications of iridium targets used for the photoactivation experiments. For details about the calibration targets gold and rhenium and for the notations used in the table, see Tab. 4.1.

After the irradiation, the β decays of the reaction products were measured at the HPGe setup using a distance of only 0.5 mm between target and detector. The large solid angle covered by the detector for this geometry gave rise to a large amount of summing effects as seen from the decay spectrum in Fig. 4.12.

Therefore, these summing effects had to be analyzed and corrected in detail according to the method described in Sec. 3.2.4. Especially for the decay of ^{190}Ir to ^{190}Os , a large number of levels in the daughter nucleus can be populated by the decay, which leads to a complex decay scheme [58]. Thus, for some of the analyzed γ transitions the correction procedure involved up to a few hundred terms in the analysis. Although all of these terms were taken into account, it was found that the major contribution of the correction stem from only a few coincident transitions. Anyhow, corrections of larger than 50% were determined for some of the γ transitions used for the data analysis of the photoneutron cross section. A list of the correction factors determined for this experiment is shown in Tab. C.3 of the appendix.

Accounting for these corrections, the target activity has been calculated from Eq. (3.8) independently for each of the analyzed γ transitions. It was found that the obtained activities agreed within a deviation of less than 5%, which confirms the reliability of the correction procedure. It needs to be emphasized, however, that this correction procedure is subject to some systematic uncertainties. The analysis relies on an accurate description of the detector response to derive the photopeak-to-total ratio described in Sec. 3.2.4. This ratio has been obtained from simulations using GEANT4, which showed some larger discrepancies to experimental data (see Fig. 3.13). An uncertainty of 30% was taken into account for this ratio, which led to a systematic uncertainty of about 10% for the determined correction factors and, thus, for the overall experimental uncertainty.

Finally, some minor corrections had to be applied due to self-absorption in the target. The

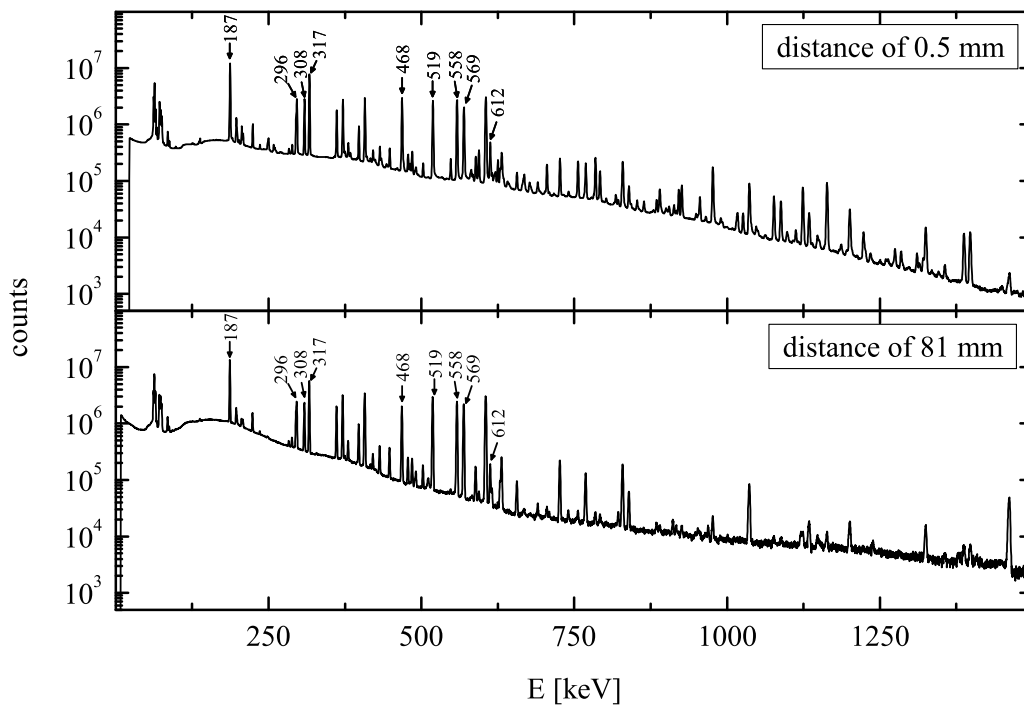


Fig. 4.12: Decay spectrum of an irradiated naturally composed iridium target. The decay was measured at the HPGe setup using a distance of 0.5 mm (top panel) and 81 mm (bottom panel) between target and detector. For better comparison, the spectra were normalized to the peak area corresponding to the strong transition at $E_\gamma = 186.68$ keV. Most of the peaks at energies above 600 keV can be identified as summing peaks stemming from the coincident detection of two lower-energetic γ transitions. Due to the much lower detection efficiency at large distance between target and detector, these summing effects have almost disappeared in the corresponding spectrum. Transitions used for the analysis of the reaction yield are marked with arrows (energies in units of keV).

corrections were found to be approximately 10%. Furthermore, for one of the irradiated targets the activity was measured as a function of time and half-lives of 11.9 ± 0.44 d and 75.0 ± 1.27 d for ^{190}Ir and ^{192}Ir have been derived, respectively, consistent with the published values of 11.78 ± 0.10 d and 73.827 ± 0.013 d [58].

Similar to ^{191}Os discussed in the previous section, both nuclei ^{190}Ir and ^{192}Ir have two isomeric states each which can be populated in the photoneutron reactions of $^{191,193}\text{Ir}$. Hence, one has principally to apply the same analysis for these reactions as described for the photoneutron reaction of ^{192}Os . However, the situation for the photoneutron reactions of $^{191,193}\text{Ir}$ is somewhat different and allows to apply the standard analysis of Sec. 3.2 if one is only interested in the total photoneutron cross section. This can be understood with regard to the quantum numbers of the states involved in the photoneutron reaction.

Both parent nuclei $^{191,193}\text{Ir}$ have a ground state of spin and parity $J^\pi = \frac{3}{2}^+$. Hence, mainly states

of rather low spin in $^{190,192}\text{Ir}$ will be populated by the corresponding photoneutron reaction as illustrated in Tab. 4.9. The ground state of ^{190}Ir is of spin $J^\pi = 4^-$ and, thus, difficult to access in the photoneutron reaction of ^{191}Ir . The same applies for the second isomeric state at $E_x = 376.4$ keV which has a spin $J^\pi = 11^-$. Instead, the population of the first isomeric state of spin $J^\pi = 1^-$ at $E_x = 26.1$ keV will be favored. This state decays to the ground state by internal transition with a half-life of 1.12 h. Because the waiting time between the end of irradiation and the beginning of the activity measurement took many hours for each irradiated target in this experiment, almost all ^{190}Ir nuclei had already decayed to their ground state at the time of measurement. For this reason, the standard analysis of Sec. 3.2 could be applied.

The same argumentation holds for the photoneutron reaction of ^{193}Ir . For ^{192}Ir , the ground state and second isomeric state at $E_x = 168.14$ keV have spin $J^\pi = 4^+$ and $J^\pi = 11^-$, respectively, and can hardly be accessed. On the other hand, the first isomeric state at $E_x = 56.72$ keV has spin $J^\pi = 1^-$ and will be highly populated. This state, however, has a half-life of only 1.45 min resulting in a quick decay to the ground state, which again allows to apply the standard analysis of Sec. 3.2.

		Neutron emission		
		<i>s</i> wave: $\frac{1}{2}^+ \otimes 0^+$	<i>p</i> wave: $\frac{1}{2}^+ \otimes 1^-$	<i>d</i> wave: $\frac{1}{2}^+ \otimes 2^+$
Excitation	E1: $\frac{3}{2}^+ \otimes 1^-$	0^- to 3^-	0^+ to 4^+	0^- to 5^-
	M1: $\frac{3}{2}^+ \otimes 1^-$	0^+ to 3^+	0^- to 4^-	0^+ to 5^+
	E2: $\frac{3}{2}^+ \otimes 2^+$	0^+ to 4^+	0^- to 5^-	0^+ to 6^+

Tab. 4.9: Accessible states of $^{190,192}\text{Ir}$ in the photoneutron reaction $^{191,193}\text{Ir}(\gamma, n)$ with regard to the conservation of spin and parity

4.4.2 Results

The experimentally determined energy-integrated cross sections of the photoneutron reactions of $^{191,193}\text{Ir}$ were used to derive normalization factors for the predicted cross sections of the TALYS and NON-SMOKER^{WEB} code as shown in Fig. 4.13. An excellent agreement with the experimental data was found for the NON-SMOKER^{WEB} code for both photoneutron reactions $^{191}\text{Ir}(\gamma, n)$ and $^{193}\text{Ir}(\gamma, n)$. On the other hand, the TALYS code overestimates the photoneutron cross section of ^{193}Ir by almost 50%. Although the cross section of ^{191}Ir seems to be very well predicted by the TALYS code, this calculation needs to be treated under reserve, because a wrong neutron separation energy for this isotope of $S_n = 8072.35$ keV is adopted in the code causing a systematic error. One might expect that the theoretical prediction yields a larger reaction yield if the correct but lower neutron separation energy of $S_n = 8026.5$ keV is used.

However, for both statistical model codes the normalization factors proved to be constant as a function of maximum photon energy E_{max} within the experimental uncertainties. This has been

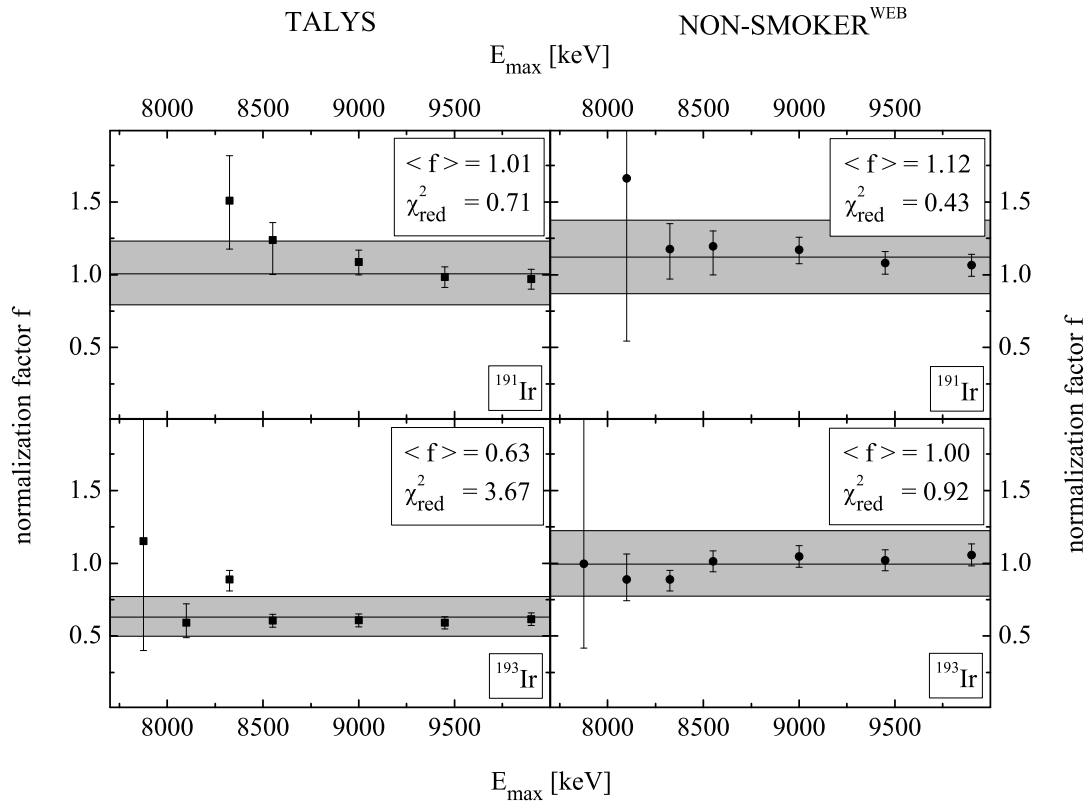


Fig. 4.13: Normalization factors f derived for two different theoretical predictions of the photoneutron cross section of $^{191,193}\text{Ir}$ at various energies E_{max} .

confirmed by a χ^2 test, although a somewhat larger value for χ^2 was found for the normalization of the TALYS code calculation in case of the photoneutron reaction of ^{193}Ir . The results for the averaged normalization factors are summarized in Tab. 4.12. As already discussed for the analysis of the other experiments, the first data point above the neutron threshold has been omitted for the determination of the averaged normalization factor $\langle f \rangle$.

Furthermore, the normalized theoretical predictions have been compared to previous experimental data of the photoneutron cross section of $^{191,193}\text{Ir}$ which stem from experiments using also bremsstrahlung [68]. These data are shown in Fig. 4.14 and quote a significantly larger photoneutron cross section close to the neutron threshold than found in the experiment of this thesis. Moreover, the energy dependence of these data points is rather inadequately described by the normalized calculations.

Finally, the astrophysically relevant ground-state reaction rates have been directly derived from experiment by the approximation of a thermal Planck spectrum. The reaction rates in comparison with the theoretical predictions are stated in Tab. 4.10 and Tab. 4.11 and confirm the results obtained for the averaged normalization factors.

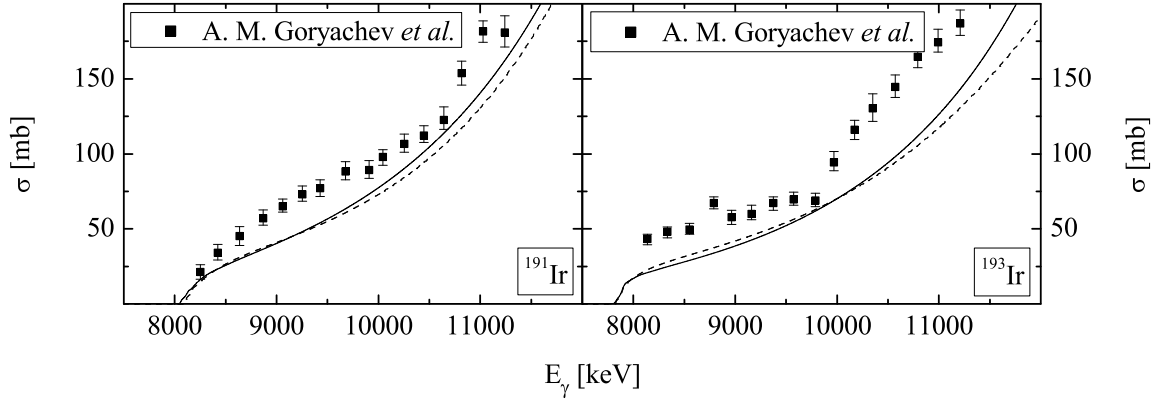


Fig. 4.14: The photoneutron cross sections of $^{191,193}\text{Ir}$ derived from photodisintegration experiments using bremsstrahlung [68] are compared with two theoretical predictions using the TALYS code (dashed line) and the NON-SMOKER^{WEB} code (solid line), respectively. Both calculations have been normalized by the factors presented in Tab. 4.12. The error bands of the calculations due to the uncertainties of the applied normalization factors have been omitted in the graphs.

^{191}Ir			
Temperature [10^9 K]	2.0	2.5	3.0
Upper energy limit [keV]	9140	9430	9750
$\lambda_{\text{Exp}}^{\text{g.s.}}$	3.04×10^{-4}	5.13×10^0	3.60×10^3
$\Delta\lambda_{\text{Exp,Yield}}^{\text{g.s.}}$	0.71×10^{-4}	1.20×10^0	0.84×10^3
$\Delta\lambda_{\text{Exp,Approx}}^{\text{g.s.}}$	0.54×10^{-4}	0.59×10^0	0.27×10^3
$\lambda_{\text{TALYS}}^{\text{g.s.}}$	2.60×10^{-4}	4.56×10^0	3.26×10^3
$\lambda_{\text{N.S.}}^{\text{g.s.}}$	2.68×10^{-4}	4.50×10^0	3.14×10^3

Tab. 4.10: Astrophysical ground-state reaction rates of ^{191}Ir determined experimentally by the approximation approach of a thermal Planck spectrum at three different temperatures are compared with theoretical predictions of two statistical model codes. The notation is described in Sec. 4.1.2.

¹⁹³ Ir			
Temperature [10^9 K]	2.0	2.5	3.0
Upper energy limit [keV]	8840	9124	9431
$\lambda_{\text{Exp}}^{\text{g.s.}}$	1.08×10^{-3}	1.46×10^1	8.21×10^3
$\Delta\lambda_{\text{Exp,Yield}}^{\text{g.s.}}$	0.25×10^{-3}	0.34×10^1	1.94×10^3
$\Delta\lambda_{\text{Exp,Approx}}^{\text{g.s.}}$	0.17×10^{-3}	0.16×10^1	0.65×10^3
$\lambda_{\text{TALYS}}^{\text{g.s.}}$	1.89×10^{-3}	2.39×10^1	1.37×10^4
$\lambda_{\text{N.S.}}^{\text{g.s.}}$	1.27×10^{-3}	1.57×10^1	8.85×10^3

Tab. 4.11: Astrophysical ground-state reaction rates of ¹⁹³Ir determined experimentally by the approximation approach of a thermal Planck spectrum at three different temperatures are compared with theoretical predictions of two statistical model codes. The notation is described in Sec. 4.1.2.

4.5 Overview

This chapter closes with a short overview of the experimental results presented in this thesis. In the previous sections the investigation of the photoneutron cross sections of ten isotopes has been described in detail. The experimental data have been compared to the predictions of two statistical model codes, the TALYS code by Koning *et al.* and the NON-SMOKER^{WEB} code by Rauscher. According to the analysis described in Sec. 3.1.1, normalization factors have been derived for the predicted photoneutron cross sections for incident photon energies just above the neutron threshold. The results for the averaged normalization factor of each of the studied photoneutron reactions are shown in Tab. 4.12. The systematic and statistical uncertainties of the measurements are denoted by $\Delta_{\text{sys}}\langle f \rangle$ and $\Delta_{\text{fit}}\langle f \rangle$, respectively. These uncertainties have been discussed in detail in Sec. 3.5. $\Delta_{\text{fit}}\langle f \rangle$ was derived from averaging the normalization factors measured at different incident photon energies E_{max} with regard to the statistical uncertainties of each individual data point. The total uncertainty $\Delta_{\text{total}}\langle f \rangle$ was then obtained from a Gaussian error propagation of $\Delta_{\text{sys}}\langle f \rangle$ and $\Delta_{\text{fit}}\langle f \rangle$.

Both theoretical model codes proved to reliably predict the photoneutron cross sections for a wide range of isotopes. For all isotopes studied in this thesis the theoretical predictions agreed with the experimental data within a factor of 2. Even in case of the isotopes ^{140,142}Ce near and at the neutron-shell closure the deviations between experiment and theory were consistent with the assumed uncertainties of the calculations. Averaging over all normalization factors a mean normalization factor of 0.81 and 0.99 has been determined for the TALYS and NON-SMOKER^{WEB} code, respectively. This suggests a slightly better agreement between experiment and theory for the NON-SMOKER^{WEB} code. However, it has to be emphasized that both values are still consistent within the experimental uncertainties. Therefore, any further conclusion on

	TALYS				NON-SMOKER ^{WEB}			
	$\langle f \rangle$	$\Delta_{\text{total}} \langle f \rangle$	$\Delta_{\text{fit}} \langle f \rangle$	$\Delta_{\text{sys}} \langle f \rangle$	$\langle f \rangle$	$\Delta_{\text{total}} \langle f \rangle$	$\Delta_{\text{fit}} \langle f \rangle$	$\Delta_{\text{sys}} \langle f \rangle$
¹⁴⁸ Nd	0.86	0.176	0.052	0.169	0.86	0.176	0.052	0.169
¹⁵⁰ Nd	0.55	0.111	0.037	0.105	0.62	0.127	0.047	0.118
¹⁵⁴ Gd	0.55	0.102	0.052	0.088	0.56	0.100	0.045	0.090
¹⁶⁰ Gd	0.93	0.151	0.039	0.145	1.15	0.186	0.051	0.179
¹⁵⁴ Sm	0.74	0.119	0.029	0.115	0.89	0.143	0.034	0.139
¹⁴⁰ Ce	1.29	0.295	0.059 [†]	0.289	1.65	0.339	0.078 [†]	0.330
¹⁴² Ce	0.74	0.135	0.013 [†]	0.134	1.02	0.205	0.019 [†]	0.204
¹⁹¹ Ir	1.01	0.221	0.042	0.217	1.12	0.244	0.041	0.241
¹⁹³ Ir	0.63	0.136	0.020	0.135	1.00	0.216	0.031	0.214
¹⁹² Os	0.79	0.162	0.028	0.159	0.99	0.204	0.043	0.200

Tab. 4.12: Overview of the experimentally determined normalization factors $\langle f \rangle$ for the theoretical predictions of various photoneutron cross sections using the TALYS and NON-SMOKER^{WEB} code derived from the experimental data of this thesis. For those uncertainties marked with a *dagger*, deviations between data points stemming from irradiations of different maximum photon energies E_{max} were found to be significantly larger than expected from the assumed statistical uncertainties. Hence, these values have to be treated under reserve.

a systematic overestimation or underestimation of one of the statistical model codes can hardly be drawn.

Moreover, with regard to the normalization factor $\langle f \rangle$ derived for each isotope both codes exhibit a similar mean deviation to the experimental data, which was determined to be about 25% for the TALYS code and 20% for the NON-SMOKER^{WEB} code. This indicates the predictive power of the two statistical model codes. Although the quoted experimental uncertainty is also about 20%, it has to be pointed out that many of the isotopes have been simultaneously irradiated. Hence, systematic uncertainties, in particular the uncertainty stemming from the photon-flux determination, are significantly reduced when comparing the normalization factors of those isotopes measured relatively to each other. One can conclude that the discrepancy between experimental data and theory is not only due to experimental uncertainties in many cases but, indeed, indicates the uncertainty of the calculations.

Furthermore, the normalized theoretical predictions have also been compared to experimental data of the photoneutron cross section stemming from previous experiments. The aim of these experiments was to study the photoneutron cross sections in the energy range of the giant dipole resonance, but in many cases data was also provided for energies down to the neutron separation energy. For some of the reactions, the normalized theoretical predictions showed quite good agreement with these data. On the other hand, for other reactions significant discrepan-

cies have been observed both for the absolute value and for the energy dependence of the cross section. Since some measurements quoted reaction yields even for incident photon energies below the neutron threshold (e. g. see Fig. 4.7), some of the discrepancies might be ascribed to experimental errors. In other cases, however, the normalized predictions were in excellent agreement with the experimental data close to the neutron threshold but showed larger deviations when approaching the giant dipole resonance (e. g. see Fig. 4.11). This deviation rather stems from uncertainties of the predicted energy dependence of the cross section and indicates that, in general, the derived normalization factors cannot be assumed to be energy-independent over a wide energy range. This calls for further investigations providing reliable experimental data with high energy resolution for energies starting at the neutron separation energy up to the giant dipole resonance.

Chapter 5

Discussion

The photoactivation experiments presented in the previous chapter have provided experimental data for the photoneutron cross sections of various isotopes just above the neutron threshold. In the first section of this chapter, it will be discussed how theoretical models can be improved on the basis of these data. The second section will provide a comprehensive overview of photoneutron reactions measured at the S-DALINAC in the last years and discuss the global predictive power of statistical model calculations for photoneutron ground-state reaction rates.

5.1 Sensitivity of statistical model calculations to nuclear physics input

As discussed in detail in Sec. 2.2, photoneutron cross sections measured under laboratory conditions only have a minor direct impact on astrophysical investigations because they do not account for the thermal population of excited states in the parent nucleus, which plays an essential role for reaction rates under stellar conditions. For this reason, the experimental data should rather be used to constrain the nuclear models involved in the theoretical calculations in order to improve the reliability of theoretical predictions for cross sections of astrophysical implications.

It has been outlined in Sec. 2.3.1 that statistical model codes involve a large variety of nuclear models for the description of quantities such as nuclear level density, optical-model potential and γ -ray strength function. The intention of this section is to discuss the sensitivity of statistical model calculations to the various nuclear input parameters.

With regard to the experimental data provided in this thesis, it is interesting to study how modifications of nuclear models affect the derived normalization factors $\langle f \rangle$ for the theoretical predictions of photoneutron cross sections. For this purpose, the experimental data of Sec. 4.1 have been reanalyzed for several isotopes of the rare-earth region using the NON-SMOKER^{WEB} code by means of different sets of nuclear input parameters.

To investigate the sensitivity to each single parameter, the absolute value of nuclear level density, neutron transmission coefficient (neutron width), and radiative transmission coefficient (γ

width) has been varied within a factor of 2. The normalization factors have then been recalculated according to the analysis described in Sec. 3.1.1, and the results have been compared to the normalization factors derived for the default parameters. However, to directly see the impact of the various parameters it is more suitable to compare the inverse of the averaged normalization factor $\langle f \rangle$. For a fixed maximum photon energy E_{\max} this quantity is directly proportional to the predicted energy-integrated cross section $I_{\sigma}^{\text{Theory}}$ (see Eq. (3.2)). Accordingly, the inverse of the normalization factor $\langle f \rangle$ averaged over various energies E_{\max} will be denoted by $\langle I_{\sigma}^{\text{Theory}} \rangle$ in the following. The results are illustrated in the left panel of Fig. 5.1.

As shown, $\langle I_{\sigma}^{\text{Theory}} \rangle$ is rather insensitive to the applied nuclear level densities. In particular, the calculations are almost independent of the adopted level density of the residual nucleus i . This can be understood with regard to the fact that maximum photon energies E_{\max} just above the neutron threshold were used for the irradiation. For this reason, only low-lying states of well-defined quantum numbers can be accessed in the residual nucleus by photoneutron reactions. According to Eq. (2.18), these states are treated separately in the calculations and, thus, independent of any adopted nuclear level density.

Moreover, the calculations also prove to be rather insensitive to variations of the neutron width and, thus, to the neutron transmission coefficient. Within variations of a factor of 2, $\langle I_{\sigma}^{\text{Theory}} \rangle$ changes by less than 20% for the studied isotopes. On the other hand, a high sensitivity has been found to variations of the γ width and, therefore, to the radiative transmission coefficients, showing that $\langle I_{\sigma}^{\text{Theory}} \rangle$ increases almost linearly with this parameter. This dependence can be observed for each of the studied isotopes. Thus, the normalization factors $\langle f \rangle$ derived in this thesis seem to provide a sensitive test for the γ -ray strength function adopted for the theoretical calculations. It should therefore be the aim of future studies to constrain the γ -ray strength function on the basis of the experimental data given in this thesis to improve the reliability of theoretical predictions for photodisintegration reactions relevant for explosive nucleosynthesis.

Furthermore, it has been suggested in previous works [19, 26, 48] that experimental data for photoneutron reactions could also be used to adjust the neutron-capture cross section of the inverse reactions. In particular, such an approach would be worthwhile to improve the neutron-capture cross sections of short-lived branching points in the s process, which cannot be measured directly in neutron-capture experiments (see Sec. 2.1.3). In previous works, it was assumed that a normalization factor determined for a theoretical calculation of a certain photoneutron cross section can also be applied to the calculation of the neutron-capture cross section of the inverse reaction, provided that both cross sections have been predicted by means of the same theoretical model. Such an approach, however, only seems reasonable if both the photoneutron and neutron-capture reaction show a similar sensitivity to the various nuclear input parameters adopted for the calculations.

For comparison with the results obtained for the sensitivity of $\langle I_{\sigma}^{\text{Theory}} \rangle$, the Maxwellian Averaged capture Cross Section (MACS) described in Sec. 2.2 has been calculated for the inverse reactions assuming a typical stellar temperature for the s process of $kT = 30$ keV. According

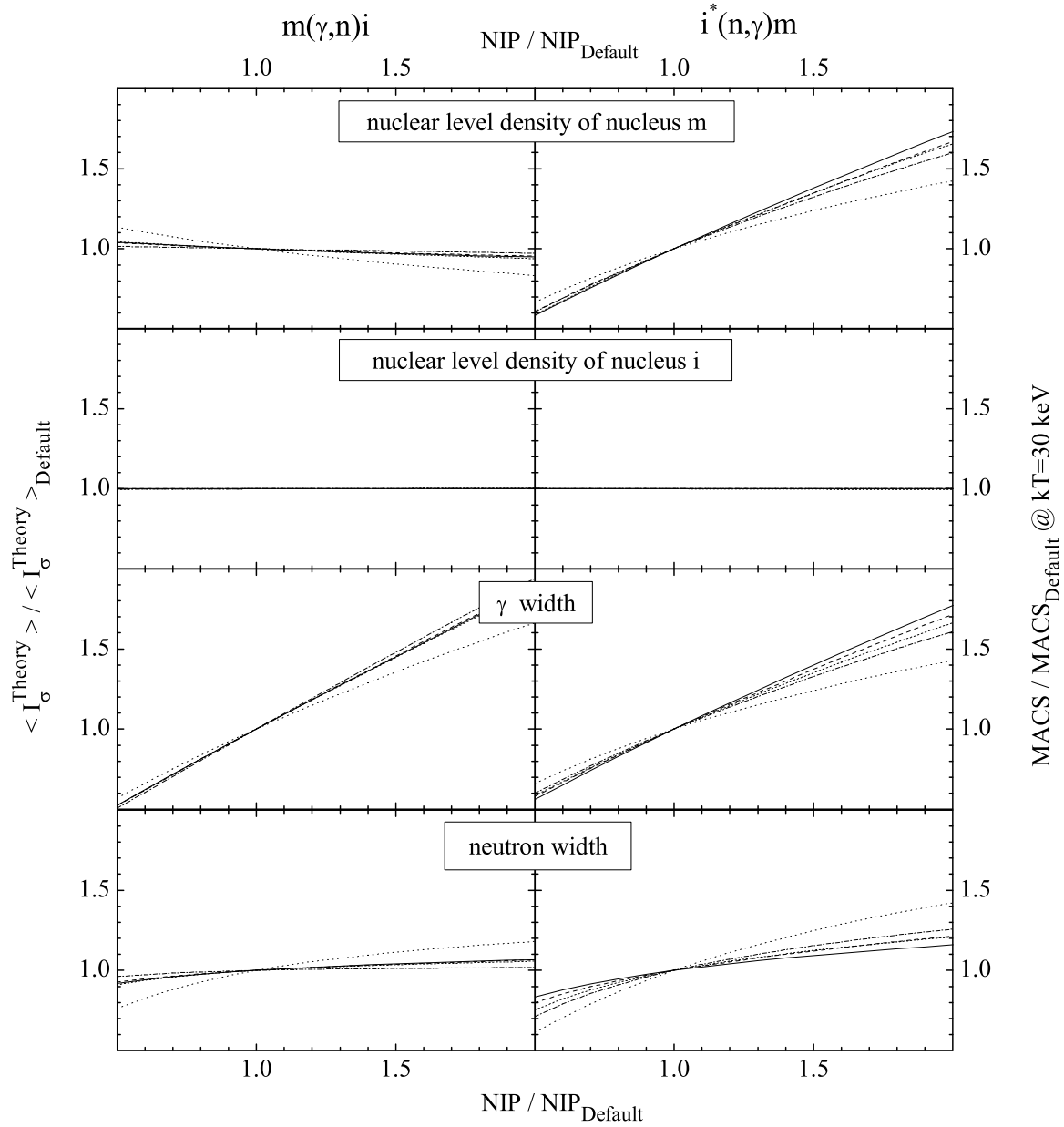


Fig. 5.1: Sensitivity of statistical model calculations to nuclear physics input. The averaged energy-integrated photoneutron cross section $\langle I_{\sigma}^{\text{Theory}} \rangle$ has been calculated for ^{148}Nd (solid line), ^{150}Nd (dashed line), ^{154}Gd (dotted line), ^{160}Gd (dashed-dotted line), and ^{154}Sm (short-dashed line) as a function of the absolute values of the nuclear input parameters (NIP) (left panel). For comparison the MACS at temperature $kT = 30$ keV of the inverse reaction is shown in the right panel. The results have been normalized to the calculations for the default parameters ($\text{NIP}_{\text{Default}}$). The *asterisk* indicates that the initial nucleus i is thermally excited in case of the neutron-capture reaction. See text for details.

to the analysis described above, several nuclear input parameters have been varied, and the calculated MACS has been compared with the calculation based on the default parameters. The results are shown in the right panel of Fig. 5.1.

Parallel to the predictions for the photoneutron reaction, the MACS shows a high sensitivity to the γ width and almost no sensitivity to the nuclear level density of the parent nucleus i . Moreover, a rather low sensitivity to the neutron width can be observed. However, in contrast to the photoneutron reaction, the nuclear level density of the compound nucleus m has a significant impact on the calculated MACS. This seems plausible, because neutron and nucleus i form a highly excited compound state. Thus, the subsequent radiative transitions can access a huge number of final states which need to be treated by appropriate nuclear models for the level density. This already illustrates the difficulty in deriving neutron-capture cross sections from the inverse photoneutron reaction. Even if the γ -ray strength function was reliably determined by photoneutron reactions, one would still have to deal with the uncertainties stemming from the description of the level density. A detailed discussion on uncertainties of nuclear level densities can be found in Ref. [35] quoting a mean uncertainty of about 50%. Hence, without setting further constraints on these nuclear models, a direct determination of neutron-capture cross sections from photoactivation experiments is hardly possible. Nevertheless, it can be expected that theoretical predictions for neutron-capture cross sections can be significantly improved if photoneutron reactions yield reliable descriptions for the γ -ray strength function.

As described in Sec. 2.3.1, the dominating contributions for the radiative transmission coefficients and, thus, for the γ -ray strength function stem from E1 transitions, which are based on a Lorentzian representation of the giant dipole resonance (GDR). The main parameters involved in these representations are the energy E^{GDR} and width Γ^{GDR} of the GDR, respectively. In case of statically deformed nuclei the GDR is described by two oscillations, one along and the other one perpendicular to the axis of rotational symmetry. Thus, one has to adopt E^{GDR} and Γ^{GDR} for each oscillation. To test the sensitivity of the theoretical predictions to these parameters, calculations for $\langle I_{\sigma}^{\text{Theory}} \rangle$ and the MACS have been performed within a variation of 10% for E^{GDR} and Γ^{GDR} . The results are illustrated in Fig. 5.2. As expected, both $\langle I_{\sigma}^{\text{Theory}} \rangle$ and the MACS increase when either E^{GDR} approaches the neutron threshold or Γ^{GDR} increases. The dependence on the different parameters appears to be similar for both types of reactions, although $\langle I_{\sigma}^{\text{Theory}} \rangle$ shows a slightly stronger sensitivity than the MACS. However, one should keep in mind that the GDR parameters for stable isotopes have usually been measured accurately. Many experiments quote uncertainties of the order of 1% or even less (e. g., see Ref. [59]). Therefore, these parameters should only give a minor contribution to the overall uncertainty of theoretical predictions for nuclei close to the valley of stability. The contributions, however, might become significant for exotic nuclei where the GDR parameters are a lot less constrained. Moreover, rather large uncertainties are expected to stem from the γ -ray strength function at lower photon energies, which can not be accurately described by the low-energy tail of a simple Lorentzian curve. Therefore, experimental data for this energy region as provided by the experiments of this thesis are mandatory.

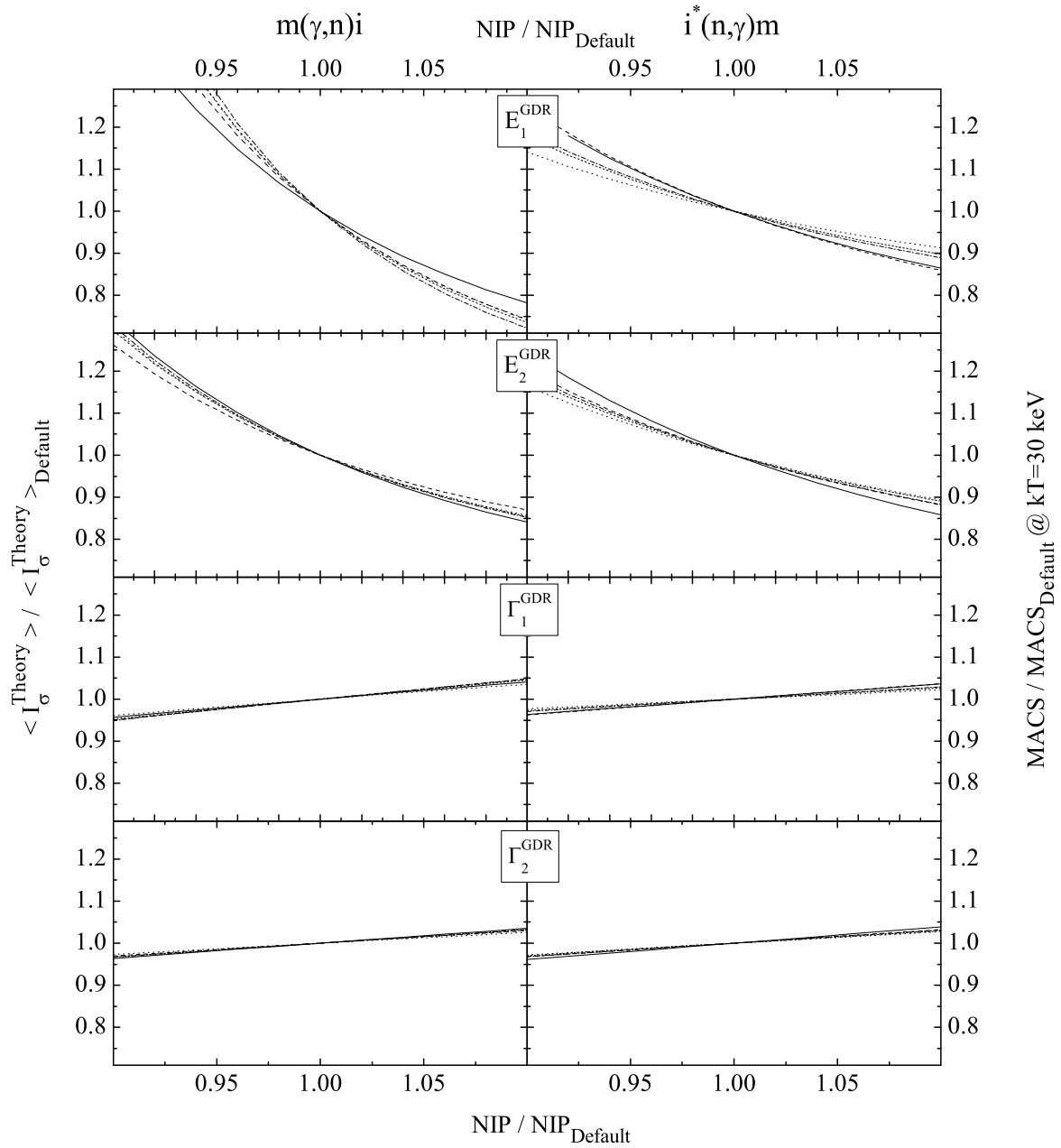


Fig. 5.2: Sensitivity of statistical model calculations to the GDR parameters. The averaged energy-integrated photoneutron cross section $\langle I_{\sigma}^{\text{Theory}} \rangle$ has been calculated for ^{148}Nd (solid line), ^{150}Nd (dashed line), ^{154}Gd (dotted line), ^{160}Gd (dashed-dotted line), and ^{154}Sm (short-dashed line) as a function of the GDR parameters (NIP) (left panel). For comparison the MACS at temperature $kT = 30$ keV of the inverse reaction is shown in the right panel. The results have been normalized to the calculations for the default parameters ($\text{NIP}_{\text{Default}}$). The *asterisk* indicates that the nucleus i is thermally excited in case of the neutron-capture reaction. See text for details.

Finally, different neutron optical-model potentials have been adopted to study the uncertainties of statistical model calculations arising from the various descriptions. As illustrated in Fig. 5.3, the results have been compared to the default calculation based on the potential by Jeukenne *et al.* [31]. In accordance with the results found for the neutron width, the calculations show a rather low sensitivity to the adopted model. Larger discrepancies can only be observed for the descriptions by Bauge *et al.* [72, 73].

In conclusion, it has been found that photoneutron reactions are mainly sensitive to the γ width, whereas other nuclear input parameters such as nuclear level densities and the neutron optical-model potential have proven to give only minor contributions to the overall uncertainty of predicted photoneutron cross sections. Thus, experimental data stemming from photoactivation experiments serve as a reliable test for different descriptions of the γ -ray strength function. However, these experiments only yield an energy-integrated cross section averaged over a large energy interval above the neutron threshold and are, therefore, less suited to constrain the energy

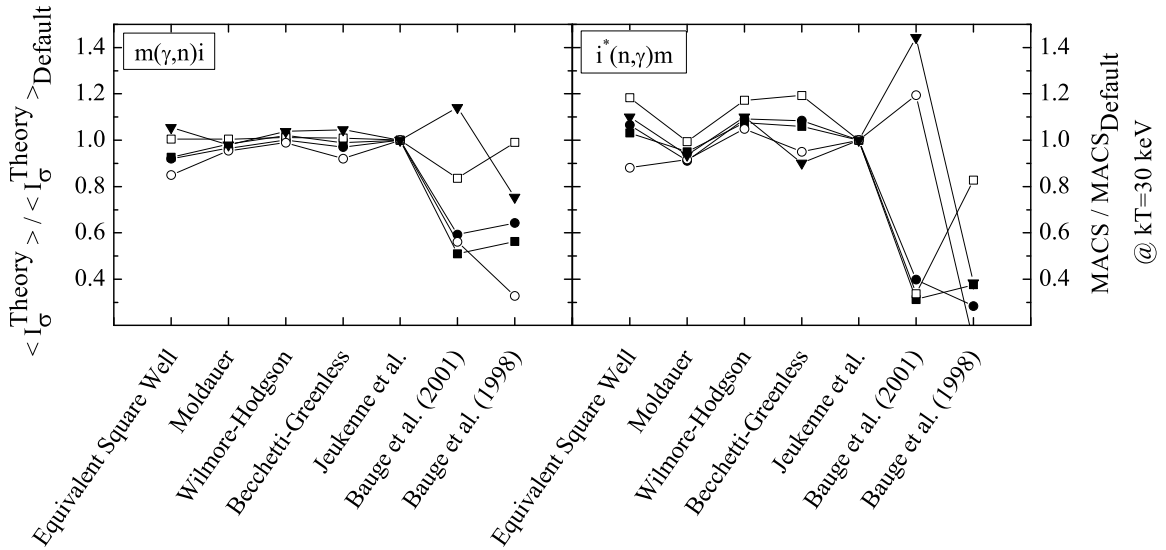


Fig. 5.3: Sensitivity of statistical model calculations to the neutron optical-model potential. The averaged energy-integrated photoneutron cross section $\langle I_{\sigma}^{\text{Theory}} \rangle$ has been calculated for ^{148}Nd (squares), ^{150}Nd (circles), ^{154}Gd (open circles), ^{160}Gd (open squares), and ^{154}Sm (triangles) for different neutron optical-model potentials using an empirical parametrization (Equivalent Square Well) and descriptions by Moldauer [69], Wilmore and Hodgson [70], Becchetti and Greenless [71], Jeukenne *et al.* [31], and Bauge *et al.* [72, 73] (left panel). For comparison the MACS at temperature $kT = 30$ keV of the inverse reaction is shown in the right panel. The results have been normalized to the calculations using the model of Jeukenne *et al.*. The data points have been connected by lines to guide the eye. The *asterisk* indicates that the nucleus i is thermally excited in case of the neutron capture reaction. See text for details.

dependence predicted by theory. This demands more sophisticated experimental techniques discussed in the outlook of this thesis.

5.2 Global predictive power of statistical model codes

This section will provide a global overview of the predictive power of statistical model calculations for photoneutron reactions just above the neutron separation energy. For this purpose, Tab. 5.1 gives a summary of all astrophysically relevant ground-state reaction rates, which have been measured in photoactivation experiments at the S-DALINAC in the last years. For comparison, the reaction rates have been calculated by means of the TALYS and NON-SMOKER^{WEB} code. For all but the experimental values marked with a *dagger*, the reaction rates have been determined using the approximation of Planck spectra as described in Sec. 3.1.2. For those values marked with a *dagger*, the photoneutron cross section has been adopted from an empirical parametrization derived from experiment as given in the references, and the ground-state reaction rate has been calculated according to Eq. (3.3). Note that no ground-state reaction rates were determined for the isotopes $^{140,142}\text{Ce}$ and ^{160}Gd discussed in this thesis.

For easier comparison, the ratios of experimental and theoretical rates have been plotted in Fig. 5.4 as a function of neutron number. A mean ratio $\langle \lambda_{\text{Exp}}^{\text{g.s.}} / \lambda_{\text{Theo}}^{\text{g.s.}} \rangle$ of 0.82 and 1.01 and a mean deviation between experiment and theory of 20.0% and 18.5% have been derived for the TALYS and NON-SMOKER^{WEB} code, respectively. No systematic dependence of the deviation with neutron number has been observed, e. g., when approaching neutron-shell closures. Thus, this result proves the excellent overall agreement between experiment and theory for photoneutron reactions with regard to the experimental uncertainties as already stated for the results found in the experiments of this thesis (see Sec. 4.5).

However, there seems to be a systematic deviation of about 25% between the two different statistical model codes. This becomes even more evident if both codes are directly compared to each other as illustrated in Fig. 5.4. This discrepancy definitely calls for further investigation in the future.

In conclusion, statistical model calculations have proven to provide reliable predictions for photoneutron reactions in the astrophysically relevant energy region just above the neutron threshold. The predicted reaction rates for almost all studied isotopes agreed with the experimental results within less than a factor of 2 with a mean deviation of only about 20%. However, only one experimental data point has yet been provided for isotopes with mass numbers $A < 140$. Further experiments are necessary to confirm the predictive power of theoretical calculations in this mass region.

Considering the fact that only global nuclear input parameters have been adopted for the calculations, the quoted uncertainty, indeed, indicates the predictive power of the theoretical models. This accuracy is sufficient for many astrophysical investigations where further improvement is

Isotope	N	$\lambda_{\text{Exp}}^{\text{g.s.}}$	$\lambda_{\text{TALYS}}^{\text{g.s.}}$	$\lambda_{\text{N.S.}}^{\text{g.s.}}$	Ref.
^{96}Zr	56	$6.63 \pm 0.31^{\dagger}$	6.96	5.98	[26]
^{148}Nd	88	64.5 ± 18.2	81.9	86.2	this thesis
^{150}Nd	90	40.9 ± 12.4	77.4	71.6	this thesis
^{154}Sm	92	7.45 ± 1.40	11.1	9.21	this thesis
^{154}Gd	90	0.112 ± 0.040	0.207	0.206	this thesis
^{187}Re	112	$91.1 \pm 10.9^{\dagger}$	99.2	74.0	[48]
^{190}Pt	112	$0.567 \pm 0.167^{\dagger}$	0.199	0.140	[47]
^{191}Ir	114	5.13 ± 1.34	4.56	4.50	this thesis
^{192}Os	116	51.0 ± 10.3	57.5	45.5	this thesis
^{192}Pt	114	0.372 ± 0.060	0.619	0.534	[47]
^{193}Ir	116	14.6 ± 3.80	23.9	15.7	this thesis
^{196}Hg	116	$0.427 \pm 0.071^{\dagger}$	0.364	0.248	[56]
^{197}Au	118	6.16 ± 0.83	7.45	5.32	[56]
^{198}Pt	120	60.8 ± 7.30	80.4	61.2	[47]
^{198}Hg	118	2.00 ± 0.27	1.75	1.41	[56]
^{204}Hg	124	57.2 ± 8.90	108	80.1	[56]

Tab. 5.1: Overview of astrophysically relevant ground-state reaction rates $\lambda_{\text{Exp}}^{\text{g.s.}}$ for a stellar temperature of $T = 2.5 \times 10^9$ K measured at the S-DALINAC using the approximation of Planck spectra as described in Sec. 3.1.2. For comparison, calculations using the TALYS ($\lambda_{\text{TALYS}}^{\text{g.s.}}$) and NON-SMOKER^{WEB} code ($\lambda_{\text{N.S.}}^{\text{g.s.}}$), respectively, are shown. All rates are quoted in units of s^{-1} . Experimental rates marked with a *dagger* have been derived from an empirical parametrization of the photoneutron cross section. The experimental rate quoted for ^{196}Hg has to be treated under reserve because the analysis was based on a wrong neutron separation energy of $S_n = 8839$ keV in Ref. [56]. The neutron number of each isotope is denoted by N . See text for details.

hampered by uncertainties for the description of astrophysical scenarios rather than by uncertainties stemming from the nuclear physics input. However, it should be emphasized again that experiments are only capable to test predictions for ground-state reaction rates, and additional uncertainties need to be taken into account for the calculations of stellar rates.

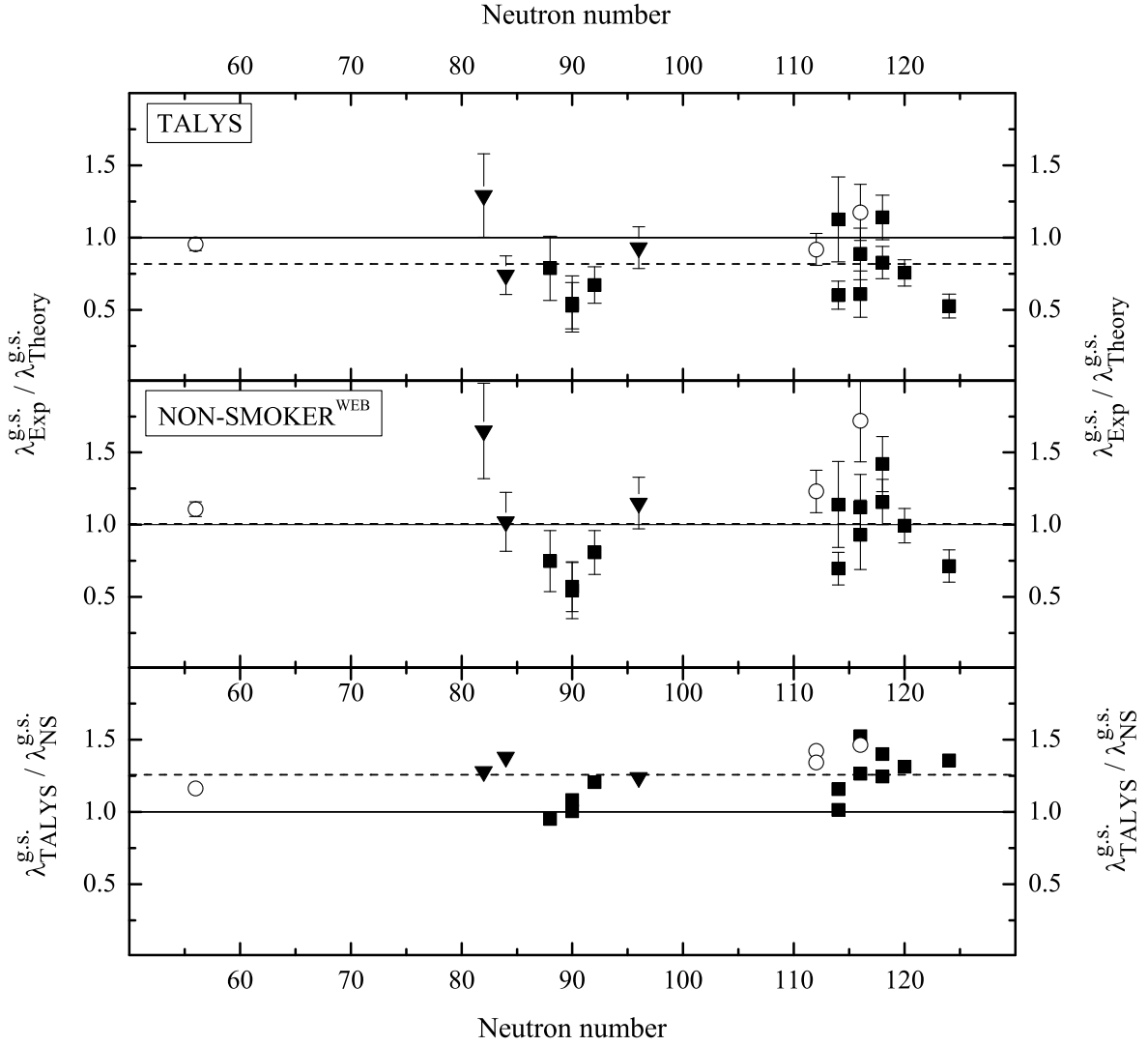


Fig. 5.4: Predictive power of statistical model calculations for astrophysically relevant ground-state reaction rates at a stellar temperature of $T = 2.5 \times 10^9$ K. Predictions stemming from the TALYS ($\lambda_{\text{TALYS}}^{\text{g.s.}}$) and NON-SMOKER^{WEB} code ($\lambda_{\text{N.S.}}^{\text{g.s.}}$) are compared with the experimentally determined rates $\lambda_{\text{Exp}}^{\text{g.s.}}$ stated in Tab. 5.1. The squares represent data points derived from the approximation of Planck spectra as described in Sec. 3.1.2, whereas open circles stem from an empirical parametrization of the photoneutron cross section. No reaction rates have been determined for the data points shown as triangles, which refer to the photoneutron reactions of $^{140,142}\text{Ce}$ and ^{160}Gd . These data points represent the averaged normalization factor $\langle f \rangle$ as stated in Tab. 4.12. The mean ratio in each plot is indicated by a dashed line. See text for more details.

Chapter 6

Summary and outlook

Photoneutron reactions play an important role in explosive astrophysical scenarios and, thus, for the nucleosynthesis of the elements heavier than iron. To provide a reliable description of the various nucleosynthetic processes, astrophysical reaction networks have to account for a huge number of reactions. Most of the reaction rates have to be predicted by theory. Therefore, it is mandatory to provide as many experimental data as possible to constrain and improve the theoretical models.

The intention of this thesis has been to provide reliable experimental data for photoneutron reactions for a wide range of isotopes and to discuss the results with regard to their astrophysical implication. For the first time, photoneutron reactions have been measured for several rare-earth isotopes in the astrophysically relevant energy region just above the neutron threshold. In addition, several isotopes of mass numbers $A \approx 190$ have been investigated to confirm the results of previous works in the heavy-mass region.

To improve the reliability of the experimental results in comparison to previous experiments, several systematic experimental uncertainties have been constrained in this thesis which had only been estimated so far. On the one hand, it has been pointed out that the uncertainty of the beam energy causes large systematic errors in photoactivation experiments, and, therefore, several experimental techniques have been applied in this thesis to constrain this uncertainty. On the other hand, the reliability of the data analysis could be improved using the advanced Monte Carlo code GEANT4. For the first time, the spectral distribution of bremsstrahlung could be reproduced by simulations without applying a correction procedure necessary in previous works.

The experimental data for photoneutron reactions derived from the experiments of this thesis showed a good agreement with the theoretical predictions of two different statistical model codes. Considering all experimental data available for photoneutron cross sections just above the neutron emission threshold, a mean uncertainty of about 20% has been derived for the theoretical calculations. This confirms the predictive power of the theoretical models. Nevertheless, it should be the aim of future investigations to further reduce this uncertainty.

In this context, the advantages and disadvantages of photoactivation experiments have been discussed in this thesis. Photoactivation experiments using bremsstrahlung combine the advantages of a very intense photon flux with the excellent energy resolution of HPGe detectors.

Therefore, these experiments are exceptionally well suited to provide a comprehensive set of data for a wide range of nuclei including even isotopes of very low abundance.

On the other hand, photoactivation experiments are restricted to the investigation of reactions where the reaction products can be detected by means of their α or β decay. For several unstable isotopes, however, the decay cannot be measured via the detection of subsequent γ transitions because either the half-life is too large or the γ intensity is too small. In these cases, a promising approach is to count the number of reaction products by means of *Accelerator Mass Spectrometry* (AMS). This technique exhibits an outstanding selectivity and sensitivity, typically many orders of magnitude higher than conventional mass spectrometry. Thus, AMS is capable to even distinguish between isobars and to count single atoms. Initially, AMS has been exclusively applied to the detection of light isotopes, in particular ^{14}C . Recent developments, however, have proven that this technique can also be used for the investigation of heavy isotopes [74]. One can expect that AMS will soon become applicable for a wide range of isotopes as a complement to conventional photoactivation experiments.

It has been shown that photoactivation experiments as described in this thesis serve as a sensitive test for the absolute value of the photoneutron cross section but are rather insensitive to its energy dependence. To further improve the nuclear models involved in statistical model calculations, in particular the γ -ray strength function, it is mandatory to provide reliable experimental data for the shape of the cross section. Although a large number of photoneutron reactions has been studied in the 70s, these experiments have usually been subject to large statistical and systematic uncertainties close to the neutron threshold. Thus, they do not serve as a reliable test for theoretical predictions in the astrophysically relevant energy region.

However, in the scope of the *Sonderforschungsbereich 634* a *tagged-photon facility* has recently been built at the S-DALINAC. At this facility, a monoenergetic electron beam is scattered in a thin radiator and produces high-energetic bremsstrahlung photons. In contrast to the photoactivation setup, the energies of the scattered electrons are measured by a magnetic spectrometer afterwards so that the energy of each bremsstrahlung photon can be determined by the well-defined energy of the incident electron and scattered electron. Therefore, this facility allows to perform experiments with quasimonoenergetic photons. It has been designed to provide photons in the energy range between 6 and 20 MeV with an excellent energy resolution of better than 25 keV [75] making it a unique tool to provide high-resolution data for photodisintegration reactions with astrophysical implication. This facility will certainly give a substantial contribution to the improvements of nuclear models relevant for astrophysical studies.

Although the statistical model codes used in this thesis have proven their predictive power for a wide range of isotopes, it has to be emphasized that most of the isotopes of astrophysical implication are far from the valley of stability, i. e., they are very difficult to access in the laboratory. Nevertheless, experimental data is obligatory to confirm the reliability of theoretical calculations even for exotic nuclei. In this context, highly advanced *radioactive beam facilities* such as *FAIR* (Facility for Antiproton and Ion Research) at the *GSI* in Darmstadt will definitely

open a new field of experimental possibilities in the next decades and, thus, play a key role for improvements of explosive nucleosynthetic processes.

Finally, it shall be mentioned that the quoted accuracy for predictions of photoneutron cross sections is sufficient for many subfields of Nuclear Astrophysics with regard to the uncertainties for other types of reactions. In the p process, e. g., the main uncertainties of astrophysical network calculations stem from rather inadequate descriptions of the α potential as underlined by Arnould and Goriely in Ref. [23]. Thus, experimental investigations, in particular, should address (γ, α) and (α, γ) reactions in the future to extend the very rare experimental data available so far. For this purpose, recently, a first photoactivation experiment to study the reaction $^{143}\text{Nd}(\gamma, \alpha)$ has been performed at the S-DALINAC [76]. This experiment, however, showed that the investigation of these reactions is extremely challenging due to the very small cross sections in the astrophysically relevant energy region. This calls for more sophisticated experimental techniques in the future.

In conclusion, more than fifty years after the pioneering work of B²FH, many questions of the nucleosynthesis of heavy elements are still unanswered. Even though the theoretical models have made large progress in the description of many astrophysical scenarios, further improvements demand reliable empirical observations from astronomers and highly accurate experimental data from nuclear physicists. Experimental investigations of thermonuclear reaction rates such as photodisintegration reactions for astrophysical network calculations have often met the limits of experimental possibilities. However, the enthusiasm and ambition of scientists will push on the development of sophisticated experimental techniques providing a deep insight into more and more features of Nuclear Physics. There is no doubt that also in the next fifty years Nuclear Astrophysics will have some surprises in store and, therefore, definitely remain an important, exciting and fascinating field of research.

Bibliography

- [1] D. Mendelejeff, *Zeitschrift für Chemie* **12** (1869) 405.
- [2] V. M. Goldschmidt, *J. Chem. Soc.* (1937) 655.
- [3] R. A. Alpher, H. Bethe, G. Gamow, *Phys. Rev.* **73** (1948) 803.
- [4] E. Burbidge, G. Burbidge, W. Fowler, F. Hoyle, *Rev. Mod. Phys.* **29** (1957) 547.
- [5] G. Wallerstein, I. Iben, P. Parker, A. M. Boesgaard, G. M. Hale, A. E. Champagne, C. A. Barnes, F. Käppeler, V. V. Smith, R. D. Hoffman, F. X. Timmes, C. Sneden, R. N. Boyd, B. S. Meyer, D. L. Lambert, *Rev. Mod. Phys.* **69** (1997) 995.
- [6] W. Hauser, H. Feshbach, *Phys. Rev.* **87** (1952) 366.
- [7] E. Anders, N. Grevesse, *Geochim. Cosmochim. Acta* **53** (1989) 197.
- [8] N. Grevesse, M. Asplund, A. J. Sauval, *Space Sci. Rev.* **130** (2007) 105.
- [9] K. Langanke, G. Martinez-Pinedo, *Rev. Mod. Phys.* **75** (2003) 819.
- [10] C. Fröhlich, G. Martinez-Pinedo, M. Liebendörfer, F.-K. Thielemann, E. Bravo, W. Hix, K. Langanke, N. Zinner, *Phys. Rev. Lett.* **96** (2006) 142502.
- [11] Z. Y. Bao, H. Beer, F. Käppeler, F. Voss, K. Wisshak, T. Rauscher, *At. Data Nucl. Data Tables* **76** (2000) 70.
- [12] KADONIS - Karlsruhe Astrophysical Database of Nucleosynthesis in Stars,
<http://www.kadonis.org>.
- [13] M. Busso, R. Gallino, G. J. Wasserburg, *Annu. Rev. Astron. Astrophys.* **37** (1999) 239.
- [14] S. Jaag, F. Käppeler, *Phys. Rev. C* **51** (1995) 3465.
- [15] R. Reifarth, C. Arlandini, M. Heil, F. Käppeler, P. V. Sedyshev, A. Mengoni, M. Herman, T. Rauscher, R. Gallino, *Astrophys. J.* **582** (2003) 1251.
- [16] K. Wisshak, R. Gallino, F. Käppeler, M. Krücka, A. Mengoni, S. Raman, F. Voss, *Phys. Rev. C* **73** (2006) 015802.

- [17] S. Marrone, U. Abbondanno, G. Aerts, F. Alvarez-Velarde, H. Alvarez-Pol, S. Andriamonje, J. Andrzejewski, G. Badurek, P. Baumann, F. Becvar, J. Benlliure, E. Berthomieux, F. Calvino, D. Cano-Ott, R. Capote, P. Cennini, V. Chepel, E. Chiaveri, N. Colonna, G. Cortes, D. Cortina, A. Couture, J. Cox, S. Dababneh, M. Dahlfors, S. David, R. Dolfini, C. Domingo-Pardo, I. Duran-Escribano, M. Embid-Segura, L. Ferrant, A. Ferrari, R. Ferreira-Marques, H. Fraiss-Koelbl, K. Fujii, W. I. Furman, R. Gallino, I. F. Goncalves, E. Gonzalez-Romero, A. Goverdovski, F. Gramegna, E. Griesmayer, F. Gunsing, B. Haas, R. Haight, M. Heil, A. Herrera-Martinez, S. Isaev, E. Jericha, F. Käppeler, Y. Kadi, D. Karadimos, M. Kerveno, V. Ketlerov, P. E. Koehler, V. Kononov, M. Krlicka, C. Lamboudis, H. Leeb, A. Lindote, M. I. Lopes, M. Lozano, S. Lukic, J. Marganiec, J. Martinez-Val, P. F. Mastinu, A. Mengoni, P. M. Milazzo, A. Molina-Coballes, C. Moreau, M. Mosconi, F. Neves, H. Oberhummer, S. O'Brien, J. Pancin, T. Papae-vangelou, C. Paradela, A. Pavlik, P. Pavlopoulos, J. M. Perlado, L. Perrot, M. Pignatari, M. T. Pigni, R. Plag, A. Plompen, A. Plukis, A. Poch, A. Policarpo, C. Pretel, J. M. Quesada, S. Raman, W. Rapp, T. Rauscher, R. Reifarth, M. Rosetti, C. Rubbia, G. Rudolf, P. Rullhusen, J. Salgado, J. C. Soares, C. Stephan, G. Tagliente, J. L. Tain, L. Tassan-Got, L. M. N. Tavora, R. Terlizzi, G. Vannini, P. Vaz, A. Ventura, D. Villamarin-Fernandez, M. Vincente-Vincente, V. Vlachoudis, F. Voss, H. Wendler, M. Wiescher, K. Wisshak, *Phys. Rev. C* **73** (2006) 034604.
- [18] F. Käppeler, A. Mengoni, *Nucl. Phys.* **A777** (2006) 291.
- [19] K. Sonnabend, P. Mohr, K. Vogt, A. Zilges, A. Mengoni, T. Rauscher, H. Beer, F. Käppeler, R. Gallino, *Astrophys. J.* **583** (2003) 506.
- [20] F. Käppeler, *Prog. Part. Nucl. Phys.* **43** (1999) 419.
- [21] J. J. Cowan, F.-K. Thielemann, J. W. Truran, *Phys. Rep.* **208** (1991) 267.
- [22] D. L. Lambert, *Astron. Astroph. Rev.* **3** (1992) 201.
- [23] M. Arnould, S. Goriely, *Phys. Rep.* **384** (2003) 1.
- [24] W. A. Fowler, G. E. Caughlan, B. A. Zimmermann, *Annu. Rev. Astron. Astrophys.* **5** (1967) 525.
- [25] T. Rauscher, F.-K. Thielemann, *At. Data Nucl. Data Tables* **75** (2000) 1.
- [26] K. Sonnabend, *Untersuchung von "branching points" im astrophysikalischen s-process mit reellen Photonen*, PhD Thesis, Institut für Kernphysik, TU Darmstadt, 2004.
- [27] NON-SMOKER^{WEB}, Version 4.6.0, <http://nucastro.org/nonsmoker.html>.
- [28] P. E. Hodgson, *Nuclear reactions and nuclear structure*, Clarendon Press, Oxford, 1971.

- [29] J. Holmes, S. Woosley, W. Fowler, B. Zimmermann, *At. Data Nucl. Data Tables* **18** (1976) 305.
- [30] A. J. Koning, S. Hilaire, M. C. Duijvestijn, in R. C. Haight *et al.*, Ed., *Proceedings of the International Conference on Nuclear Data for Science and Technology - ND2004, Sep. 26 - Oct. 1, 2004, Santa Fe, USA*, 2005, Volume 769 of *AIP*, (p. 1154).
- [31] J.-P. Jeukenne, A. Lejeune, C. Mahaux, *Phys. Rev. C* **16** (1977) 80.
- [32] A. Lejeune, *Phys. Rev. C* **21** (1980) 1107.
- [33] F.-K. Thielemann, M. Arnould, in K. Böckhoff, Ed., *Proceedings of the International Conference on Nuclear Data for Science and Technology*, D. Reidel Publ. Co., Brüssel, 1983, (p. 762).
- [34] C. M. McCullagh, M. L. Stelts, R. E. Chrien, *Phys. Rev. C* **23** (1981) 1394.
- [35] T. Rauscher, F.-K. Thielemann, K.-L. Kratz, *Phys. Rev. C* **56** (1997) 1613.
- [36] A. J. Koning, J. P. Delaroche, *Nucl. Phys.* **A713** (2003) 231.
- [37] J. Kopecky, M. Uhl, *Phys. Rev. C* **41** (1990) 1941.
- [38] T. Ericson, *Adv. Phys.* **9** (1960) 425.
- [39] A. Gilbert, A. G. W. Cameron, *Can. J. Phys.* **43** (1965) 1446.
- [40] A. Richter, in S. Meyers *et al.*, Ed., *Proceedings of Fifth European Particle Accelerator Conference*, IOP, Bristol, 1996, (p. 110).
- [41] K. Vogt, *Bestimmung von (γ,n) -Reaktionsraten für den astrophysikalischen γ -Prozess und Parametrisierung von Neutronenseparationsenergien*, PhD Thesis, Institut für Kernphysik, TU Darmstadt, 2003.
- [42] Application Software Group, **GEANT 3.21**, CERN programm Library Long Writeup **W5013**, 1994.
- [43] S. Agostinelli, J. Allison, K. Amako, J. Apostolakis, H. Araujo, P. Arce, M. Asai, D. Axen, S. Banerjee, G. Barrant, F. Behner, L. Bellagamba, J. Boudreau, L. Broglia, A. Brunengo, H. Burkhardt, S. Chauvie, J. Chuma, R. Chytrcek, G. Cooperman, G. Cosmo, P. Degt'yarenko, A. Dell'Acqua, G. Depaola, D. Dietrich, R. Enami, A. Feliciello, C. Ferguson, H. Fesefeldt, G. Folger, F. Foppiano, A. Forti, S. Garelli, S. Giani, R. Giannitrapani, D. Gibin, J. J. G. Cadenas, I. Gonzalez, G. G. Abril, G. Greeniaus, W. Greiner, V. Grichine, A. Grossheim, S. Guatelli, P. Gumplinger, R. Hamatsu, K. Hashimoto, H. Hasei, A. Heikkinen, A. Howard, V. Ivanchenko, A. Johnson, F. W. Jones, J. Kallenbach, N. Kanaya, M. Kawabata, Y. Kawabata, M. Kawaguti, S. Kelner, P. Kent, A. Kimura,

- T. Kodama, R. Kokoulin, M. Kossov, H. Kurashige, E. Lamanna, T. Lampen, V. Lara, V. Lefebure, F. Lei, M. Liendl, W. Lockman, F. Longo, S. Magni, M. Maire, E. Medernach, K. Minamimoto, P. M. de Freitas, Y. Morita, K. Murakami, M. Nagamatu, R. Nartallo, P. Nieminen, T. Nishimura, K. Ohtsubo, M. Okamura, S. O'Neale, Y. Oohata, K. Paech, J. Perl, A. Pfeiffer, M. G. Pia, F. Ranjard, A. Rybin, S. Sadilov, E. D. Salvo, G. Santin, T. Sasaki, N. Savvas, Y. Sawada, S. Scherer, S. Sei, V. Sirotenko, D. Smith, N. Starkov, H. Stoecker, J. Sulkimo, M. Takahata, S. Tanaka, E. Tcherniaev, E. S. Tehrani, M. Tropeano, P. Truscott, H. Uno, L. Urban, P. Urban, M. Verderi, A. Walkden, W. Wander, H. Weber, J. P. Wellisch, T. Wenaus, D. C. Williams, D. Wright, T. Yamada, H. Yoshida, D. Zschesche, Nucl. Instr. and Meth. A **506** (2003) 250.
- [44] P. Mohr, J. Enders, T. Hartmann, H. Kaiser, D. Schiesser, S. Schmitt, S. Volz, F. Wissel, A. Zilges, Nucl. Instr. and Meth. A **423** (1999) 480.
- [45] S. Volz, N. Tsoneva, M. Babilon, M. Elvers, J. Hasper, R.-D. Herzberg, H. Lenske, K. Lindenberg, D. Savran, A. Zilges, Nucl. Phys. A **779** (2006) 1.
- [46] K. Vogt, P. Mohr, M. Babilon, W. Bayer, D. Galaviz, T. Hartmann, C. Hutter, T. Rauscher, K. Sonnabend, S. Volz, A. Zilges, Nucl. Phys. A **707** (2002) 241.
- [47] K. Vogt, P. Mohr, M. Babilon, J. Enders, T. Hartmann, C. Hutter, T. Rauscher, S. Volz, A. Zilges, Phys. Rev. C **63** (2001) 055802.
- [48] S. Müller, D. Galaviz, A. Kretschmer, K. Sonnabend, A. Zilges, Phys. Rev. C **73** (2006) 025804.
- [49] P. Mohr, K. Vogt, M. Babilon, J. Enders, T. Hartmann, C. Hutter, T. Rauscher, S. Volz, A. Zilges, Phys. Lett. B **488** (2000) 127.
- [50] R. Longland, C. Iliadis, A. E. Champagne, C. Fox, J. R. Newton, Nucl. Instr. and Meth. A **566** (2006) 452.
- [51] C. Siegel, *Experimentelle Bestimmung der Effizienz eines Niederenergie-Gamma-Detektors*, Bachelor Thesis, Institut für Kernphysik, TU Darmstadt, 2006, unpublished.
- [52] J. Glorius, *Untersuchung von γ -Zerfallskaskaden mit Niederenergie-Photonenspektrometern*, Bachelor Thesis, Institut für Kernphysik, TU Darmstadt, 2007, unpublished.
- [53] A. Constantinescu, *Untersuchung der Ablenkeigenschaften eines Dipolmagneten und Entwicklung eines Teilchen-Raytracers*, Bachelor Thesis, Institut für Kernphysik, TU Darmstadt, 2007, unpublished.
- [54] M. Fritzsche, *Entwicklung einer Online-Energiekontrolle für den S-DALINAC*, Diploma Thesis, Institut für Kernphysik, TU Darmstadt, 2007, unpublished.

- [55] B. Wiik, *Messung der Tritiumausbeute aus Kernphotoreaktionen am Silber mit Bremsstrahlung bis zu 56 MeV*, PhD Thesis, Institut für Kernphysik, TH Darmstadt, 1965.
- [56] K. Vogt, P. Mohr, T. Rauscher, K. Sonnabend, A. Zilges, Nucl. Phys. **A718** (2003) 575c.
- [57] K. Sonnabend, K. Vogt, D. Galaviz, S. Müller, A. Zilges, Phys. Rev. C **70** (2004) 035802.
- [58] NNDC Online Data Service, ENSDF database,
<http://www.nndc.bnl.gov/nndc/ensdf/>.
- [59] P. Carlos, H. Beil, R. Bergere, A. Lepretre, A. Veyssi re, Nucl. Phys. **A172** (1971) 437.
- [60] P. Carlos, H. Beil, R. Bergere, A. Lepretre, A. de Miniac, Nucl. Phys. **A225** (1974) 171.
- [61] O. V. Vasil'ev, V. A. Semenov, S. F. Semenko, Yad. Fiz. **13** (1971) 463.
- [62] G. M. Gurevich, L. E. Lazareva, V. M. Mazur, S. Y. Merkulov, G. V. Solodukhov, V. A. Tyutin, Nucl. Phys. **A351** (1981) 257.
- [63] F. Dreyer, H. Dahmen, J. Staude, H. H. Thies, Nucl. Phys. **A192** (1972) 433.
- [64] B. L. Berman, M. A. Kelly, R. L. Bramblett, J. T. Caldwell, H. S. Davis, S. C. Fultz, Phys. Rev. **185** (1969) 1576.
- [65] A. Lepretre, H. Beil, R. Bergere, P. Carlos, J. Fagot, A. de Miniac, A. Veyssi re, H. Miyase, Nucl. Phys. **A258** (1976) 350.
- [66] A. Sauerwein, *Auswertung eines Photoaktivierungsexperimentes zur Photodisintegration von ^{192}Os* , Bachelor Thesis, Institut f r Kernphysik, TU Darmstadt, 2007, unpublished.
- [67] B. L. Berman, D. D. Faul, R. A. Alvarez, P. Meyer, D. L. Olson, Phys. Rev. C **19** (1979) 1205.
- [68] A. M. Goryachev, G. N. Zalesnyy, Yad. Fiz. **27** (1978) 1479.
- [69] P. A. Moldauer, Phys. Rev. C **177** (1969) 1841.
- [70] D. Wilmore, P. E. Hodgson, Nucl. Phys. **55** (1964) 673.
- [71] F. D. Becchetti, G. W. Greenlees, Phys. Rev. **182** (1969) 1190.
- [72] E. Bauge, J. P. Delaroche, M. Girod, Phys. Rev. C **58** (1998) 1118.
- [73] E. Bauge, J. P. Delaroche, M. Girod, Phys. Rev. C **63** (2001) 024607.
- [74] K. Knie, T. Faestermann, G. Korschinek, G. Rugel, W. R hm, C. Wallner, Nucl. Instr. and Meth. B **172** (2000) 717.

- [75] K. Lindenberg, *Development and Construction of the Low-Energy Photon Tagger NEP-TUN*, PhD Thesis, Institut für Kernphysik, TU Darmstadt, 2007.
- [76] E. Gehrman, *Vorbereitung und Durchführung eines Experiments zur (γ, α) -Reaktion an ^{143}Nd* , Bachelor Thesis, Institut für Kernphysik, TU Darmstadt, 2007, unpublished.
- [77] Isotrak catalogue, *Calibration standards and instruments for measuring radioactivity*, Second Edition, 2001.

Appendix A

Parametrization of bremsstrahlung spectra

In this section, a simple parametrization for bremsstrahlung spectra will be provided to reliably estimate the photon flux at the photoactivation setup of the S-DALINAC (see Sec. 3.1). This parametrization has been derived from extensive simulations using the Monte Carlo code GEANT4 as described in Sec. 3.3.1.

It has been found that the spectral shape of bremsstrahlung of maximum photon energy $E_{\max} > 7500$ keV can be accurately described by a linear function for photon energies $E_\gamma > 6500$ keV:

$$n_\gamma(E_\gamma, E_{\max}) = a(E_{\max}) \times E_\gamma + b(E_{\max}) \quad , \quad (\text{A.1})$$

where n_γ denotes the photon flux in units of $(\text{s cm}^2 \text{ keV } \mu\text{A})^{-1}$, and E_γ and E_{\max} are in units of keV, respectively. The two parameters a and b each are a function of E_{\max} and have been derived from a large number of simulations for various incident beam energies. It has been found that they can be parameterized in front of the collimator by

$$a(E_{\max}) = -(0.097 - 0.04 \times e^{-0.00047(E_{\max}-7000)}) \times E_{\max} \quad (\text{A.2})$$

$$b(E_{\max}) = 657.284 \times E_{\max} + 159.454 \quad (\text{A.3})$$

and behind the collimator by

$$a(E_{\max}) = -(0.00032 - 0.00012 \times e^{-0.001(E_{\max}-7000)}) \times E_{\max} \quad (\text{A.4})$$

$$b(E_{\max}) = 2.4247 \times E_{\max} - 3847.31 \quad . \quad (\text{A.5})$$

Using these parameters, a mean deviation of less than 15% has been determined between the simulations and the parametrization of Eq. (A.1). However, very close to the cut-off the deviation increases and larger discrepancies have been found for energies as close as 100 keV to E_{\max} in front of the collimator and 300 keV behind the collimator, respectively. In this energy region, the parametrization should only be applied under reserve. Although the accuracy of this parametrization is usually not sufficient to be involved in the detailed analysis of experiments, it allows for a reliable estimation of the photon flux for a wide energy range.

As a final remark, it has to be mentioned that the numeric values of the parameters of Eq. (A.2) to Eq. (A.5) have only been derived for a distance of 6.5 cm between radiator and collimator. For the modified experimental setup of slightly larger distance (see Sec. 3.1), the parameters a and b have not been determined. However, it was found that the spectral shape of the photon flux remains almost unchanged, whereas the photon-flux intensity is reduced by about a factor of 6 in front of the collimator and by about 5% behind the collimator.

Appendix B

Input for detection-efficiency calibrations

B.1 Calibration sources

Isotope	Activity [kBq]	E_γ [keV]	I_γ [%]	Transmission [%]
^{133}Ba	44.90 ± 1.35^a	53.2	2.199 ± 0.022	94.9
		79.6	2.620 ± 0.060	97.7
		81.0	34.06 ± 0.270	97.7
		160.6	0.645 ± 0.008	98.4
		223.2	0.450 ± 0.004	98.5
		276.4	7.164 ± 0.220	98.6
		302.9	18.33 ± 0.060	98.7
		356.0	62.05 ± 0.190	98.7
		383.8	8.940 ± 0.030	98.7
^{109}Cd	39.10 ± 1.56^c	88.0	3.700 ± 0.100	97.8
^{57}Co	392.0 ± 11.8^b	122.1	85.60 ± 0.170	98.2
		136.5	10.68 ± 0.080	98.2
^{60}Co	46.10 ± 1.38^a	1173.2	99.85 ± 0.030	99.3
		1332.5	99.98 ± 0.001	99.3
^{137}Cs	45.70 ± 1.37^a	661.7	85.10 ± 0.200	100.0
^{54}Mn	400.0 ± 12.0^a	834.9	99.98 ± 0.001	100.0
^{22}Na	38.50 ± 1.16^a	1274.6	99.94 ± 0.014	100.0
^{210}Pb	40.70 ± 1.63^c	46.5	4.250 ± 0.040	96.8

Tab. B.1: Specifications of calibration sources. The γ intensities per decay I_γ were taken from Ref. [58]. The transmission accounts for the absorption of photons in the surrounding plastic housing and has to be taken into account for detection-efficiency calibrations. The transmission factors have been adopted from Ref. [77].
Reference date: *a*: 01.12.1999, *b*: 01.02.2005, *c*: 01.03.2006.

B.2 Detector dimensions

Detector	S/N	\varnothing [mm]	l [mm]	Δ [mm]	d [mm]
HPGe	GI-423	57.0	62.0	1.0 (Al)	3.0
LEPS1	43-TE 389	36.0	13.0	0.25 (Be)	7.0
LEPS2	43-TE 391	36.0	13.0	0.25 (Be)	7.0
NRF1	72902	77.0	80.0	1.0 (Al)	3.0
NRF2	73760	78.9	79.0	1.0 (Al)	3.5
NRF3	72930	78.0	78.0	1.0 (Al)	5.0
NRF4	b 90006	73.0	77.0	1.0 (Al)	5.0

Tab. B.2: Dimensions of the detectors used for the experiments of this thesis as implemented in the simulations with GEANT4. The diameter and length of the sensitive crystal are denoted by \varnothing and l , respectively. The thickness of the entrance window and the distance between detector crystal and entrance window are quoted by Δ and d , respectively. In addition, a cooling finger of 9.0 mm diameter and 49.0 mm length for the *HPGe* detector and an additional absorbing mylar layer of 0.025 mm for both *LEPS* have been taken into account. The *LEPS* and *HPGe* detector have been used for activity measurements in this thesis (see Sec. 3.2.1), whereas detectors denoted by *NRF* (Nuclear Resonance Fluorescence) have been mounted behind the collimator of the photoactivation setup to measure the photon-scattering reaction of ^{11}B (see Sec. 3.3.2). In addition, detector *NRF4* has been used for a direct measurement of the spectral distribution of bremsstrahlung (see Sec. 3.4.2).

Appendix C

Correction factors for the determination of target activity

C.1 Corrections for self-absorption and target dimensions

As described in Sec. 3.2.3, the detection efficiencies determined for point-like sources have to be corrected before being adopted for the determination of target activity according to Eq. (3.8). The corrections account for the finite dimensions of a target (a disk of 20 mm diameter) and for self-absorption of photons within the target material. For all targets studied in this thesis simulations using GEANT4 have been performed to derive the corresponding correction factors denoted by k_{ε} . A selection of correction factors for both detector setups used in the experiments of this thesis is shown in Tab. C.1.

C.2 Correction factors for summing effects

The coincident detection of photons gives rise to summing effects in the observed spectra, which need to be corrected in the data analysis as discussed in detail in Sec. 3.2.4. The correction factors calculated for the γ transitions used for the data analysis in the experiments of this thesis are summarized in Tab. C.2 and Tab. C.3. With regard to the various terms contributing in the correction procedure, the total correction factor k_{total} has been divided into:

- k_{cascades} : Refers to contributions according to Eq. (3.15) and Eq. (3.16)
- k_{summing} : Refers to contributions according to Eq. (3.17)
- $k_{\text{X-rays}}$: This correction stems from coincident events between γ transitions and X-rays subsequent to the decay of the parent nucleus. Therefore, this contribution usually only becomes significant if the parent nucleus decays by electron capture. This correction has not been discussed explicitly in Sec. 3.2.4 but can be treated in analogy to Eq. (3.15) and Eq. (3.16).

Target	m [mg]	E_γ [keV]	k_ε (LEPS)	k_ε (HPGe)
Au	50	333.0	0.927	0.981 ^a
		426.1	0.931	0.990 ^a
	200	333.0	0.916	0.978 ^a
		426.1	0.923	0.998 ^a
Re	350	122.6	0.774	0.864 ^a
		137.2	0.808	0.883 ^a
Gd	50	69.7	0.830	0.931 ^a
		103.0	0.894	0.957 ^a
Nd	45	91.1	0.894	0.973 ^a
		270.2	0.932	0.988 ^a
Sm ₂ O ₃	500	69.7	0.508	0.857 ^a
		103.0	0.738	0.991 ^a
	1750	69.7	0.206	0.552 ^a
		103.0	0.470	0.970 ^a
CeO ₂	800	145.4	–	0.927 ^b
		165.9	–	0.958 ^b
OsO ₂	400	129.4	0.765	0.857 ^a
		646.0	0.918	0.991 ^a
	1725	129.4	0.461	0.552 ^a
		646.0	0.911	0.970 ^a
Ir	330	186.9	–	0.872 ^c
		296.0	–	0.918 ^c
		612.5	–	0.924 ^c

Tab. C.1: Correction factors k_ε for the detection efficiency due to self-absorption and target dimensions as described in Sec. 3.2.3. The distance between target and detector at the LEPS setup was 5 mm. At the HPGe setup different distances were used, which is indicated by the superscripts (*a*: 81 mm, *b*: 42 mm, *c*: 0.5 mm).

The total correction factor k_{total} can be calculated from:

$$k_{\text{total}} = \left(1 - \sum_i 1 - \frac{1}{k_i} \right)^{-1}, \quad (\text{C.1})$$

where k_i refers to the various contributions stated above.

Isotope	Detector	E_γ [keV]	k_{cascades}	k_{summing}	$k_{\text{X-rays}}$	k_{total}
^{148}Nd	(2)	91.105	1.0032	1	1.026	1.029
		531.016	1	1	1.026	1.026
^{150}Nd	(2)	114.314	1.0529	1	1.026	1.082
		155.873	1.0610	1	1.026	1.090
		211.309	1.0122	0.992	1.026	1.030
		267.693	1.0721	0.998	1.026	1.100
		270.166	1.0104	0.914	1.026	0.945
^{154}Gd	(2)	97.431	1	1	1.148	1.148
		103.18	1.0204	1	1.148	1.175
^{160}Gd	(2)	57.996	1	1	1	1
		226.04	1.0365	1	1	1.037
		348.28	1	0.998	1	0.998
		363.55	1.0204	1	1	1.020
^{154}Sm	(2)	69.673	1.0418	1	1.026	1.070
		97.431	1.0289	1	1.026	1.056
		103.18	1.0079	1	1.026	1.034
^{187}Re	(1)	122.64	1	1	1	1
		137.157	1	1	1	1
^{197}Au	(2)	333.03	1.0403	1	1.134	1.185
		355.73	1.0107	1	1.134	1.148
		426.10	1	1	1	1

Tab. C.2: Correction of summing effects involved in the photoactivation experiment of isotopes in the rare-earth region. Correction factors have been determined for each γ transition analyzed in the experiment. The calculations have been performed for both the HPGe setup (1) and the LEPS setup (2) for a distance of 81 mm and 5 mm between detector and target, respectively. See Sec. 3.2.4 for a detailed discussion and Sec. C.2 for the notations used in the table.

Isotope	Detector	E_γ [keV]	k_{cascades}	k_{summing}	$k_{\text{X-rays}}$	k_{total}
^{191}Ir	(1)	186.86	1.5786	1	1.050	1.651
		518.55	1.5327	1	1.050	1.614
		569.30	1.5249	0.9887	1.050	1.595
		557.95	1.3059	0.9146	1.050	1.248
^{193}Ir	(1)	295.96	1.3714	1	1	1.379
		308.46	1.3415	1	1	1.341
		316.51	1.2277	1	1	1.228
		468.07	1.1632	1	1	1.163
		612.46	1.1592	0.576	1	0.668
^{187}Re	(1)	122.64	1	1	1	1
		137.157	1	1	1.037	1
^{197}Au	(1)	333.03	1.1692	1	1.087	1.290
		355.73	1.0413	1	1.087	1.136
		426.10	1	1	1	1

Tab. C.3: Correction of summing effects involved in the photoactivation experiment of $^{191,193}\text{Ir}$. Correction factors have been determined for each γ transition analyzed in the experiment. The calculations have been performed for the HPGe setup (1) for a distance of 0.5 mm between detector and target. See Sec. 3.2.4 for a detailed discussion and Sec. C.2 for the notations used in the table.

List of Figures

2.1	Solar abundance distribution	6
2.2	Uncertainties of elemental abundances	6
2.3	Nucleosynthesis in the rare-earth region	8
2.4	Gamow-like window of photoneutron reactions	16
2.5	Normalized partition functions as a function of temperature	17
2.6	Compound-state reaction	21
3.1	Schematic layout of the superconducting Darmstadt electron linear accelerator S-DALINAC	26
3.2	Schematic layout of the photoactivation setup	27
3.3	Photon flux at the photoactivation setup	28
3.4	Reaction yield of photoactivation experiments as a function of maximum photon energy	30
3.5	Approximation of a Planck spectrum using bremsstrahlung	31
3.6	Typical decay spectrum of an irradiated gold target	33
3.7	Beam-current record	33
3.8	Spectrum of natural background at the HPGe and LEPS setup	34
3.9	Detection efficiency of the HPGe and LEPS setup	36
3.10	Variation of detection efficiency as a function of distance between source and detector	37
3.11	Angular distribution of bremsstrahlung at the photoactivation setup	39
3.12	Typical β -decay scheme	40
3.13	Photopeak-to-total ratio of a HPGe detector as a function of photon energy	42
3.14	Spectral shape of bremsstrahlung	44
3.15	Detection efficiency for photon-scattering reactions	47
3.16	Comparison of bremsstrahlung simulations using the Monte Carlo codes GEANT3 and GEANT4	48
3.17	Absolute normalization of the photon flux using various standard reactions	49

3.18	Sensitivity of the photoneutron reaction yield to the absolute beam energy . . .	50
3.19	Direct measurement of bremsstrahlung	53
3.20	Comparison of directly measured bremsstrahlung spectra with simulations . . .	54
3.21	Reaction yields for photoneutron reactions very close to the neutron threshold .	55
3.22	Distribution of deposited charge in a segmented radiator	57
3.23	Experimental uncertainties	59
4.1	Determination of the half-life of ^{147}Nd	63
4.2	Normalization factors for the photoneutron cross sections of $^{148,150}\text{Nd}$	64
4.3	Normalization factors for the photoneutron cross sections of ^{154}Sm	65
4.4	Normalization factors for the photoneutron cross sections of $^{154,160}\text{Gd}$	65
4.5	Energy dependence of the photoneutron cross sections for isotopes in the rare-earth region	67
4.6	Normalization factors for the photoneutron cross sections of $^{140,142}\text{Ce}$	71
4.7	Energy dependence of the photoneutron cross sections of $^{140,142}\text{Ce}$	72
4.8	Level scheme of ^{191}Os	74
4.9	Ratio of population of the ground state and isomeric state of ^{191}Os after the photoneutron reaction $^{192}\text{Os}(\gamma, n)$	77
4.10	Normalization factors for the photoneutron cross section of ^{192}Os	78
4.11	Energy dependence of the photoneutron cross section of ^{192}Os	78
4.12	Decay spectrum of an irradiated naturally composed iridium target	81
4.13	Normalization factors for the photoneutron cross sections of $^{191,193}\text{Ir}$	83
4.14	Energy dependence of the photoneutron cross sections of $^{191,193}\text{Ir}$	84
5.1	Sensitivity of statistical model calculations to nuclear physics input	91
5.2	Sensitivity of statistical model calculations to the GDR parameters	93
5.3	Sensitivity of statistical model calculations to the neutron optical-model potential	94
5.4	Predictive power of statistical model calculations for astrophysically relevant ground-state reaction rates	97

List of Tables

2.1	Stellar photoneutron reaction rates	18
3.1	Specifications of targets irradiated very close to the neutron separation energy .	55
3.2	Specifications of various techniques for the determination of beam energy . . .	58
4.1	Specifications of targets used for photoactivation experiments of isotopes in the rare-earth region	62
4.2	Astrophysical ground-state reaction rates of $^{148,150}\text{Nd}$ and ^{154}Sm	68
4.3	Astrophysical ground-state reaction rates of ^{154}Gd	69
4.4	Specifications of cerium targets used for photoactivation experiments	70
4.5	Accessible states of ^{191}Os in the photoneutron reaction $^{192}\text{Os}(\gamma, n)$	73
4.6	Specifications of osmium targets used for photoactivation experiments	76
4.7	Astrophysical ground-state reaction rates of ^{192}Os	79
4.8	Specifications of iridium targets used for photoactivation experiments	80
4.9	Accessible states of $^{190,192}\text{Ir}$ in the photoneutron reaction $^{191,193}\text{Ir}(\gamma, n)$	82
4.10	Astrophysical ground-state reaction rates of ^{191}Ir	84
4.11	Astrophysical ground-state reaction rates of ^{193}Ir	85
4.12	Overview of experimentally determined normalization factors for photoneutron cross sections	86
5.1	Overview of astrophysically relevant ground-state reaction rates measured at the S-DALINAC	96
B.1	Specifications of calibration sources	111
B.2	Dimensions of HPGe detectors	112
C.1	Correction factors for the detection efficiency due to self-absorption and target dimensions	114
C.2	Correction of summing effects involved in the photoactivation experiment of isotopes in the rare-earth region	115

C.3	Correction of summing effects involved in the photoactivation experiment of $^{191,193}\text{Ir}$	116
-----	---	-----

Publications

During my employment at the *Institut für Kernphysik, Technische Universität Darmstadt*, the following articles have been published:

- J. Hasper, S. Müller, D. Savran, L. Schnorrenberger, K. Sonnabend, and A. Zilges,
Investigation of photoneutron reactions close to and above the neutron emission threshold in the rare earth region,
Phys. Rev. C **77** (2008) 015803.
- M. Elvers, J. Hasper, S. Müller, D. Savran, L. Schnorrenberger, K. Sonnabend, and A. Zilges,
Nuclear Astrophysics with real photons – the data acquisition system of the NEPTUN tagger setup,
J. Phys. G: Nucl. Part. Phys. **35** (2008) 014027 (Proceedings of Nuclear Physics in Astrophysics III, 26.03. - 31.03.2007, Dresden, Germany).
- D. Savran, M. Babilon, A. M. van den Berg, M. N. Harakeh, J. Hasper, H. J. Wörtche, and A. Zilges,
Investigation of the Pygmy Dipole Resonance in $(\alpha, \alpha'\gamma)$ coincidence experiments,
Nucl. Phys. **A788** (2007) 165C (Proceedings).
- W. Bayer, R. Eichhorn, M. Gopych, H.-D. Gräf, J. Hasper, A. Richter, and A. Zilges,
X-ray spectroscopy - a new method to investigate field emission in superconducting accelerating cavities,
Nucl. Inst. Meth. Phys. Res. A **575** (2007) 321.
- D. Savran, M. Babilon, A. M. van den Berg, M. K. Harakeh, J. Hasper, A. Matic, H. J. Wörtche, and A. Zilges,
Nature of Pygmy Dipole Resonance in ^{140}Ce studied in $(\alpha, \alpha'\gamma)$ experiments,
Phys. Rev. Lett. **97** (2006) 172502.
- S. Volz, N. Tsoneva, M. Babilon, M. Elvers, J. Hasper, R.-D. Herzberg, H. Lenske, K. Lindenberg, D. Savran, and A. Zilges,
The photoresponse of stable $N = 82$ nuclei below 10 MeV,
Nucl. Phys. **A779** (2006) 1.

- K. Sonnabend, S. Müller, M. Elvers, J. Hasper, L. Kern, K. Lindenberg, and A. Zilges,
Photodissociation as a tool for nuclear astrophysics,
Proceedings of Science, NIC IX, 057 (Proceedings of the International Symposium on Nuclear Astrophysics – Nuclei in the Cosmos – IX, 25.06. 20.06.2006, CERN, Geneva, Switzerland).
- K. Sonnabend, M. Babilon, J. Hasper, S. Müller, M. Zarza, and A. Zilges,
Photodissociation of neutron deficient nuclei,
European Physical Journal **A27** (2006) s1.149 (Proceedings of the Nuclear Physics in Astrophysics II Conference, 16.05. - 20.05.2005, Debrecen, Hungary).
- J. Hasper, K. Lindenberg, and A. Zilges,
Design of a low-energy photon tagger at the S-DALINAC,
BgNS Transactions **10** (2005) 2 (Proceedings of XVI International School on Nuclear Physics, Neutron Physics and Nuclear Energy, 19.09. - 26.09.2005, Varna, Bulgaria).

Acknowledgment

This work had never been possible without the support of numerous people. At this point, once again, I sincerely would like to thank all of them.

I'm very indebted to Prof. Dr. Andreas Zilges who gave me the opportunity to play an active part in current research work in nuclear physics. In all the time preparing for my doctorate, he repeatedly gave me the chance to participate in international conferences and experiments. I am deeply grateful for all the personal and scientific experiences gained during that time. Furthermore, I very much appreciate the confidence he placed in my work as well as being open-minded, honest, and motivating. I look forward to an exciting, successful, and eventful collaboration in Cologne.

Thanks go also to Prof. Dr. Norbert Pietralla for his willingness to officially continue the supervision of my work. Even though we only worked together for a fairly short time, I very much enjoyed sharing his fascination for physics.

I owe special thanks to Prof. Dr. Thomas Rauscher from Basel for numerous interesting discussions about astrophysical network calculations which opened my eyes in many areas. Assisting me immensely with the application of the statistical model calculations contributed significantly to the success of this work.

I am also thankful for the advice and assistance of Dr. Franz Käppeler from Karlsruhe in pursuing our research work. Due to his friendly and cooperative manner, working together always meant a great pleasure for me.

Furthermore, I am, of course, deeply grateful to my present and former colleagues Dr. Mario Babilon, Dr. Wolfgang Bayer, Marc Büssing, Dipl.-Phys. Janis Endres, Dipl.-Phys. Michael Elvers, Dipl.-Phys. Matthias Fritzsche, Dr. Daniel Galaviz Redondo, Dr. Kai Lindenberg, Dipl.-Phys. Sebastian Müller, Dr. Deniz Savran, Dipl.-Phys. Linda Schnorrenberger, Dr. Kerstin Sonnabend and Dr. Stephan Volz. Seen from the personal as well as scientific point of view, every single one of them contributed to a great extent to an extremely enjoyable collaboration in the past years.

I am not only obliged to my colleagues I closely worked with but also to all other staff members of the institute for their support and the pleasant work environment. I, especially, would like to mention the technical staff and the accelerator group of Dr. Ralf Eichhorn for providing excellent beam conditions during my experiments. Moreover, I would like to convey special thanks to the workshop of the mechanics and electronics technician. Many ideas had not been possible to realize without their help.

Scientific research work always entails a great deal of administrative work. Therefore, I do not want to miss to thank, in particular, Andrea Sobota and Giovanna Umberti for the excellent job they have done. The unelaborated handling of numerous bureaucratic matters helped me immensely to fully concentrate on my scientific work.

Scientific research is altogether not possible without the respective funds for research. Therefore, I would also like to take the opportunity to thank the *Deutsche Forschungsgemeinschaft* (DFG) for supporting this work as part of the *Sonderforschungsbereich 634*.

I am grateful for the moral support of all friends and relatives who repeatedly enabled me to take my mind off the problems faced in physics, to brace new energies and get new ideas pursuing other activities.

There is no way to express my gratitude to my parents for supporting and assisting me. The certainty that I always can count on them in all regards has always brought an enormous relief I am extremely thankful for.

Finally, my special thanks goes to my partner Karolina Glodowska. It is beyond words to express my appreciation for being exceptionally understanding during all that time for the many extra hours I had to work. She always had a sure feeling when I needed support, and without her help this work had hardly been possible. I very much look forward to our shared future.

Lebenslauf

Persönliche Daten

Name	Jens Hasper
Geburtsdatum	07.07.1981
Geburtsort	Bad Hersfeld
Staatsangehörigkeit	deutsch
Eltern	Gabriele und Helmut Hasper
Bekenntnis	evangelisch
Familienstand	ledig

Schul Ausbildung

1987 - 1991	Grundschule an der Sommerseite, Bad Hersfeld
1991 - 1997	Gesamtschule Obersberg, Bad Hersfeld
1997 - 2000	Oberstufe an der Modellschule Obersberg, Bad Hersfeld
Juni 2000	Abitur an der Modellschule Obersberg, Bad Hersfeld

Wehrdienst

1997 - 1998	Panzer grenadier bataillon 52, Rotenburg/Fulda
-------------	--

Universitätsausbildung

2001 - 2005	Diplomstudiengang im Fachbereich Physik, TU Darmstadt
2005	Diplom (mit Auszeichnung)
seit 2005	Promotionsstudent am Institut für Kernphysik, TU Darmstadt

Beruflicher Werdegang / Beschäftigungsverhältnisse

2003	zweimonatige Tätigkeit als Werkstudent (Siemens Medical Solutions, Erlangen, Abteilung MREA)
2003 - 2005	Studentische Hilfskraft (Fachbereich Physik, TU Darmstadt)
seit 2005	Wissenschaftlicher Mitarbeiter (Institut für Kernphysik, TU Darmstadt)

Wissenschaftliche Auszeichnungen

2000	DPG-Buchpreis für hervorragende Leistungen im Fach Physik
2005	Gerhard-Herzberg-Studienpreis

Erklärung

Die vorliegende Arbeit stellt meinen ersten Promotionsversuch dar; sie ist von mir selbstständig verfasst. Überall dort, wo ich die Gedanken und Ideen anderer verwendet oder entlehnt, mich auf fremde Kenntnisse in Wort oder Schrift gestützt habe, habe ich dies kenntlich gemacht und die verwendeten Quellen angegeben.

Teile dieser Arbeit wurden bereits publiziert:

J. Hasper, S. Müller, D. Savran, L. Schnorrenberger, K. Sonnabend, and A. Zilges,
Investigation of photoneutron reactions close to and above the neutron emission threshold in the rare earth region,
Phys. Rev. C **77** (2008) 015803.

Darmstadt, im Januar 2008

(Jens Hasper)

